Multiparticle Azimuthal Correlation Measurements in Lead-Lead and Proton-Lead Collisions at LHC with the CMS Detector

By

Shengquan Tuo

Dissertation

Submitted to the Faculty of the

Graduate School of Vanderbilt University

in partial fulfillment of the requirements

for the degree of

DOCTOR OF PHILOSOPHY

in

Physics

May, 2015

Nashville, Tennessee

Approved:

Professor Julia Velkovska

Professor Senta Greene

Professor Will Johns

Professor Robert Scherrer

Professor Akram Aldroubi

To my parents,

Fenglian Hao and Aixiu Tuo,

For making me be who I am today

Acknowledgments

This dissertation would not have been possible without the guidance and the help from many people.

First and foremost, I would like to express my deepest gratitude to my advisor, Dr. Julia Velkovska, who guided and mentored me through the entire journey of my graduate studies. I learned from Julia not only the knowledge of heavy ion physics but the way of thinking, analyzing and solving problems. Julia also provided me with the enthusiasm and inspiration to physics which was very important for me. She is very good at finding what is more important to do. As an example, the first figure of our most important paper in the dissertation, Phys. Lett. B 724 (2013) 213, was initially just a cross check plot, but she suggested to publish this figure. It turned out the figure was one of the best results in the paper and after that other collaborations started to publish papers based solely on similar studies in the figure.

I would also like to thank Dr. Charles Maguire and Dr. Senta Victoria Greene for the help and support. I learned the importance of being responsible at work from both Charlie and Vicki. Charle impressed me by submitting thousands of crab jobs even at late nights to test the Vanderbilt T2 performance. Vicki, as one of the Ph.D. committee members, read the dissertation very carefully and gave a lot of comments.

My thanks go out to my friends and colleagues at Vanderbilt University, Eric Appelt, Ron Belmont, Shengli Huang, Michael Issah, Ravi Janjam, Pelin Kurt, Yaxian Mao, Hong Ni, Weizhuang Peng, Dillon Roach, Brennan Schaefer, Monika Sharma, Ben Snook, Momchil Velkovsky and Qiao Xu. I remember the excitement we shared and the discovery we made together.

It is my pleasure to work in the CMS Collaboration. I would like to thank many people I worked and traveled with in the pase few years: Yuting Bai, Colin Baus, Jeremy Callner, Raphael Granier de Cassagnac, Rylan Conway, Torsten Dahms, Sunil Dogra, Doga Gulhan, David Hofman, Xavier Janssen, Kurt Jung, Vladimir Korotkikh, Krisztian Krajczar, Yen-Jie Lee, Wei Li, Frank Ma, Camelia Mironov, Matthew Nguyen, Sandra Padula, Christof Roland, Gunther Roland, Steve Sanders, Ferenc Sikler, Kevin Stenson, George Stephans, Dragos Velicanu, Gabor Veres, Fuqiang Wang, Quan Wang, Bolek Wyslouch, Victoria Wyslouch, Lingshan Xu, Yetkin Yilmaz, Anna Zsigmond. A special thanks to Wei Li for the fruitful discussions and help in the last few years.

Thinking back to my undergraduate time and before, I should thank these people who had a big effect to me and guided me to physics: Zizong Xu, Xiaolian Wang and Hongfang Chen for introducing heavy ion physics to me in the University of Science and Technology of China. Honglan Du and Hongye Xie for providing various opportunities in the middle school. Jian Zhang and Fengsheng Wu for encouraging me to study math and science.

Finally, I would like to appreciate all my family members. I would like to thank my wife, Xia Guo, for her patience, support and encouragement. Thanks a lot to my new baby girl, Kailin Tuo, for the fun and happiness you bring to us. I am gratefull for the love, support and encouragement from my mother Fenglian Hao and my father Aixiu Tuo. I would like to thank my brothers Wenquan Tuo, Wanquan Tuo and Meiquan Tuo, my sisters Ruirui Tuo and Xiaorui Tuo, and new family members Kaizhan Tuo, Yanling Huang, Hai Wu, Na Huo and Likeng Huang for the love and support.

TABLE OF CONTENTS

流水不腐, 户枢不蠹, 动也。 - 吕氏春秋·尽数 (239 BC, China)

Flowing waters do not stagnate and door hinges do not get mole crickets, because they move.
- The Annals of LüBuwei (Translated by J. Knoblock and J. Riegel)

List of Tables

Table **Page**

List of Figures

Figure **Page**

Abbreviations and Symbols

η	The pseudorapidity defined as $\eta = -\ln(\tan(\theta/2))$ where θ is the polar angle with respect to the z-axis
η/s	The ratio of shear viscosity to entropy density
ϵ_n	nth order asymmetry of the initial state
ϵ_{part}	Participant eccentricity
μ_B	Baryon chemical potential
ϕ	The azimuthal angle, $\phi = \arctan(y/x)$, generally of a particle produced in a collision
Ψ_R	Reaction plane angle
Ψ_{EP}	Event Plane angle
Ψ_n	Participant plane angle
$\sqrt{s_{NN}}$	Center-of-mass energy per nucleon pair
$\sqrt{s}$	The center-of-mass energy of a collision system
b	Impact parameter between two colliding nuclei. May also be used as an abbreviation for barn or bottom quark, or an abbreviation for a barn, where 1 b = 10^{-24} cm^2
$c_2\{4\}$	Four-particle cumulant
CGC	Color Glass Condensate
E_{T}	The transverse energy, defined $E_{\mathrm{T}} = \sqrt{m^2 + p_{\mathrm{T}}^2}$, where m is the mass of the object
N_{coll}	Number of binary collisions between nucleons in a nucleus-nucleus or proton-nucleus collision
N_{part}	Number of participating nucleons in a nucleus-nucleus collision
$N_{trk}^{offline}$	The number of offline reconstructed tracks with $\lvert\eta\rvert < 2.4$ and $p_T > 0.4$ GeV/c without efficiency correction
R_{AA}	The nuclear modification factor for some collision between two nuclei of species A, for example Pb or Au.
v_n	nth Fourier coefficient of the azimuthal distribution of particles produced in a collision
$v_n\{2\}$	nth Fourier coefficient of the azimuthal distribution from two-particle correlations
$v_n\{4\}$	nth Fourier coefficient of the azimuthal distribution from four-particle correlations
$v_n\{6\}$	nth Fourier coefficient of the azimuthal distribution from six-particle correlations
$v_n\{8\}$	nth Fourier coefficient of the azimuthal distribution from eight-particle correlations
$v_n\{LYZ\}$	nth Fourier coefficient of the azimuthal distribution from all-particle correlations

$v_n\{EP\}$ nth Fourier coefficient of the azimuthal distribution from event plane method

y The rapidity of a particle or reference frame, defined $y = \tanh^{-1}\beta_z$, where $\beta_z = v_z/c$ and v_z is the velocity along the z-axis

p_T The transverse momentum, $\sqrt{p_x^2 + p_y^2}$, of a particle produced in a collision where the z-axis is generally taken as the direction of motion of the incoming particles

GEANT4 GEometry ANd Tracking, version 4, a CERN software package to simulate the passage of particles through matter

AA Generally refers to a collision between two nuclei of species A

AGS Alternating Gradient Synchrotron

ALICE A Large Ion Collider Experiment, one of the four large experiments at the LHC, and the one experiment dedicated to heavy ion physics

ATLAS Originally stood for A Toroidal LHC ApparatuS, one of the four large LHC experiments

BHC Beam Halo Counter

BNL Brookhaven National Laboratory

BRAHMS Broad RAnge Hadron Magnetic Spectrometers, one of the large experiments at RHIC

BSC Beam Scintillator Counter

CDF The Collider Detector at Fermilab, a large experiment at the Tevatron collider

CEP Critical End Point

CERN European Organization for Nuclear Research

CGC Color Glass Condensate, an effective field theory describing QCD in the saturation regime

CMS Compact Muon Solenoid, one of the four main LHC experiments

ECAL The Electromagnetic Calorimeter of the CMS detector

eV Electron Volt

HCAL The Hadronic Calorimeter of the CMS detector

HF Forward Hadron Calorimeter

HLT High Level Trigger, the second stage of the CMS trigger system consisting of commercial processors

L1 Level-1 (Trigger System), the initial stage of the CMS trigger system consisting of custom programmable electronics

LHC Large Hadron Collider

LHCb Large Hadron Collider beauty, one of the four large LHC experiments

MC Monte Carlo, a type of computer algorithm relying on repeated random sampling to obtain numerical results

PbPb Lead-Lead

PHENIX Pioneering High Energy Nuclear Interaction eXperiment, one of the large experiments at RHIC

PS Proton Synchrotron

PSB Proton Synchrotron Booster

pp Proton-Proton

pPb Proton-Lead

QCD Quantum Chromodynamics

QGP Quark-gluon plasma

RHIC Relativistic Heavy Ion Collider

SPS Super Proton Synchrotron

STAR Solenoidal Tracker at RHIC, one of the large experiments at RHIC

TEC Tracker Endcap, one of the CMS silicon strip detector components

TIB Tracker Inner Barrel, one of the CMS silicon strip detector components

TID Tracker Inner Disc, one of the CMS silicon strip detector components

TOB Tracker Outer Barrel, one of the CMS silicon strip detector components

UPC Ultra-Peripheral Collision, an electromagnetic interaction between nuclei colliding with a very large impact parameter

Chapter 1

Introduction

It is expected that a novel phase of hot and dense matter, Quark Gluon Plasma (QGP), existed at the extremely high temperature of the early universe shortly after the Big Bang. In order to study the properties of this hot and dense matter, physicists build accelerators and collide heavy ions at ultra-relativistic energies to create the QGP in controlled laboratory conditions. The experiments at the Relativistic Heavy Ion Collider (RHIC) announced the discovery of the QGP in 2005. One of the most important features of the produced medium is the strong azimuthal correlation between the produced particles, which indicates that the QGP behaves like an almost perfect liquid. The evolution in the properties of this fluid as a function of the initial temperature and the system size is studied in this thesis by measurements performed in lead-lead (PbPb) and proton-lead (pPb) collisions at the higher center-of-mass energies available at the Large Hadron Collider (LHC) at the European Organization for Nuclear Research (CERN), Switzerland. The question of whether there is a collision system size limit for the produced medium to behave like a liquid is addressed by exploring multiparticle correlations arising in the PbPb and pPb collisions. The data were collected using the Compact Muon Solenoid (CMS) experiment at LHC.

1.1 QCD Phase Diagram

Quantum Chromo Dynamics (QCD) is the fundamental theory describing the strong interaction between quarks and gluons. The non-Abelian nature of the QCD gauge symmetry leads to the asymptotic freedom of the QCD interaction and the confinement of quarks and gluons within hadrons. Shortly after the discovery of these properties of QCD, people realized that a new phase of QCD matter should exist at extremely high temperature or energy density, in the very early universe or in the inner core of a neutron star [1, 2]. The term Quark Gluon Plasma was first coined by Shuryak, describing the potentially plasma-like phase in such extreme conditions [3].

The asymptotic freedom feature of QCD means that the quarks and gluons interact asymptotically weakly at high energy or small distance scales [4]. In this case, the theory can be simplified and solved using a perturbative expansion. It has been successful in describing a large set of processes involving large-momentum-transfer scatterings. The perturbative QCD calculations fail at low energy or large-distance scales because in these circumstances the coupling constant is much larger. An alternative approximation method called lattice QCD, where the field equations are solved numerically on discrete space-time grids, can provide quantitative information about the QCD phase transition and Equation of State (EoS) of the deconfined medium. For an ideal massless gas limit (Stefan-Boltzmann limit), the EoS is given by:

$$P = \frac{1}{3}\epsilon, \quad \epsilon = g\frac{\pi^2}{30}T^4 \tag{1.1}$$

where P is the pressure, ϵ is the energy density, T is the temperature and g is the effective number of degrees of freedom. The value of g is 47.5 for a three quark flavor QGP, much larger than that of a pion gas where g is 3 .

Figure 1.1 shows the energy density ϵ divided by T^4 as a function of temperature from a lattice QCD calculation [5]. One can see that the energy density increases rapidly around the critical temperature T_c, which is due to the increase of the effective degrees of freedom. The critical temperature T_c is around 170 MeV. Different curves shown in different colors in the plot are using different number of quark flavors as shown in the legends. The ϵ_{SB}/T^4 is the calculation from the Stefan-Boltzmann limit.

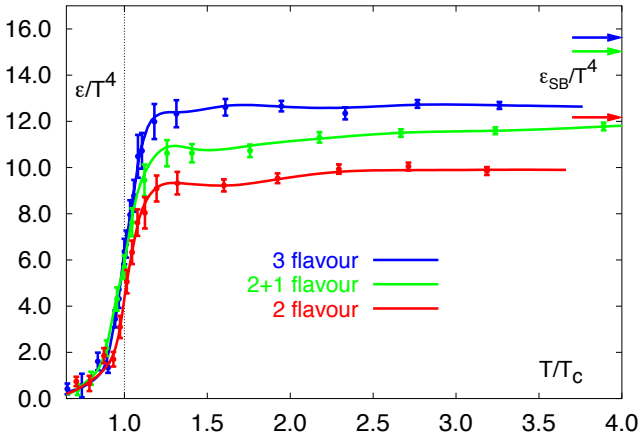

Figure 1.1: Energy density ϵ divided by T^4, the number of degree of freedom, as a function of temperature T from lattice QCD [5]. The critical temperature T_c is around 170 MeV.

The rich phase structure of QCD is illustrated in Figure 1.2. The left hand side of Figure 1.2 is a qualitative illustration of the QCD phase diagram as a function of temperature and baryon chemical potential. The baryon chemical potential, μ_B, can be thought of as a measure of the net baryon density. It is the amount of energy added to a system held at constant volume and entropy with the addition of one baryon.

At high baryon density, a first order transition to quark-gluon matter is expected to occur as more and more cold nuclear matter is compressed to a small volume. This leads to a color superconductor phase due to the Cooper pairing of quarks similar to the pairing of electrons into "quasi-bosons", which is responsible for the superconductivity in solid-state physics [6]. Neutron stars are the densest and tiniest stars in the universe with radii of only about 12-13 km and masses of the order a few times the mass of the Sun. The inner cores of neutron stars are so dense that they might be good candidates for observing cold quark matter [7].

The universe evolved from very high temperature and zero baryon density after the Big Bang. The evolution of the produced matter after a heavy ion collision is also quite similar with a very small μ_B. The current universe is only one event of a Big Bang. With the heavy ion experiments, we can produce a lot of collisions (or "Little Bangs") and study the evolution of the expansion. From lattice QCD, the phase transition is found to change from a first order transition at a high value of μ_B to a crossover (with no discontinuities in the thermodynamic observables, as opposed to the

first or second order phase transitions) at low value of μ_B [8, 9], though the position of the critical end point (CEP) is still uncertain.

The right hand side of Figure 1.2 is the phase diagram plotted as a function of pressure and temperature, as we usually do for ordinary matter. The calculated pressure and temperature state for the medium produced in each heavy ion experiment is indicated in the plot. The boundary to the unphysical region is $\mu_B = 0$ and is quantitatively described by lattice QCD and a free pion gas at low temperature and pressure [10].

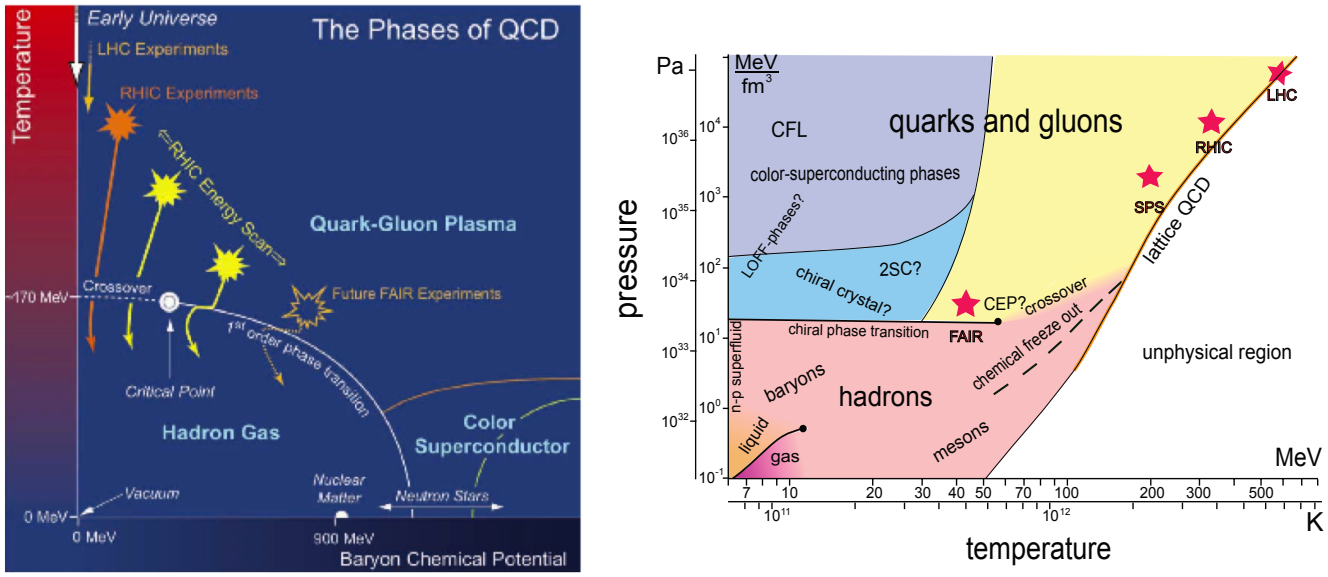

Figure 1.2: Left: The QCD phase diagram as a function of temperature and baryon chemical potential [11]. Right: The phase diagram in the pressure-temperature plane [10]

It is possible to obtain some information about the QCD phase diagram from data by looking at the relative yields of different particle species [12] and interpret them within a statistical thermal model. If a thermally equilibrated QGP is formed, it will transition to a hadron gas and form hadrons with abundances that are determined by their masses and the baryon chemical potentials in the system. The hadron abundances that are observed in the experiment reflect a stage in the system evolution called "chemical freeze-out" (see Section 1.2.1). The chemical freeze-out temperature T and the baryon chemical potential μ_B can be extracted from fit parameters. Figure 1.3 shows the QCD phase diagram from data and thermal model calculations. At the LHC, the preliminary best fit temperature is 156 MeV [13], slightly lower than the value at RHIC energies (160 - 170 MeV) [14].

1.2 Heavy Ion Collisions

The first facility to accelerate ion beams was the BEVALAC at Lawrence Berkeley National Laboratory, which could accelerate uranium ion beams up to an energy of 2.1 GeV/nucleon in the early 1980s [15]. The Alternating Gradient Synchrotron (AGS) at Brookhaven National Laboratory (BNL) allowed Au+Au collisions at center of mass energies per nucleon pair from $\sqrt{s_{NN}} =$

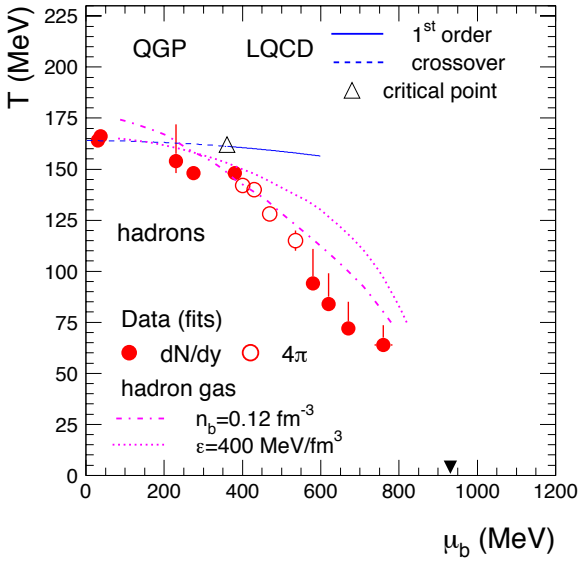

Figure 1.3: QCD phase diagram from data and thermal model calculations [12].

2.68 GeV to $\sqrt{s_{NN}} = 4.75$ GeV. The Super Proton Synchrotron (SPS) at CERN can accelerate Pb ion beams and provide Pb+Pb collisions up to $\sqrt{s_{NN}} = 17.3$ GeV [16]. The Relativistic Heavy-Ion Collider is a heavy ion collider at BNL. It started its first run in 2000. Unlike the previous fixed target experiments, RHIC is the first facility designed to collide two heavy ion beams. The top heavy ion collision energy at RHIC is $\sqrt{s_{NN}} = 200$ GeV. Four experiments were set up to collect data: BRAHMS [17], PHENIX [18], PHOBOS [19] and STAR [14]. The PHENIX and STAR experiments are still running with upgraded detector systems. Different collision systems were tried at RHIC, with Au+Au, Cu+Cu, Cu+Au, U+U, d+Au, ^{3}He+Au, and p+p. The highest energy collider to date is the LHC at CERN with nucleon-nucleon center-of-mass energy of $\sqrt{s_{NN}} = 2.76$ TeV for Pb+Pb collisions and $\sqrt{s_{NN}} = 5.02$ TeV for p+Pb collisions. The designed top energy for Pb+Pb collisions at the LHC is $\sqrt{s_{NN}} = 5.5$ TeV.

Before the operation of RHIC, no unambiguous evidence for the QGP formation was found, although several signals found at SPS suggested the formation of a "new state of matter" [20]. After the first three runs of RHIC from the year 2000 to 2003, the four experiments announced the discovery of the QGP in 2005 [14, 17–19, 21–25]. Before discussing the signatures of the QGP, we will first introduce different stages of a heavy ion collision.

1.2.1 Stages of a Relativistic Heavy Ion Collision

The most important theoretical achievement in this area in the past decade might be the emergence of an integrated dynamical modeling approach of a relativistic heavy ion collision. The matter produced in a collision goes through several stages ending with particles observed in the detectors located around the collision point. Figures 1.4 and 1.5 illustrate different stages for a relativistic heavy ion collision.

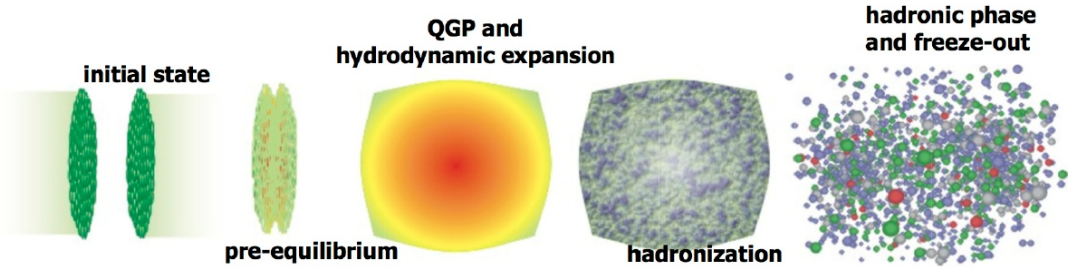

Figure 1.4: Different stages for a relativistic heavy ion collision [26].

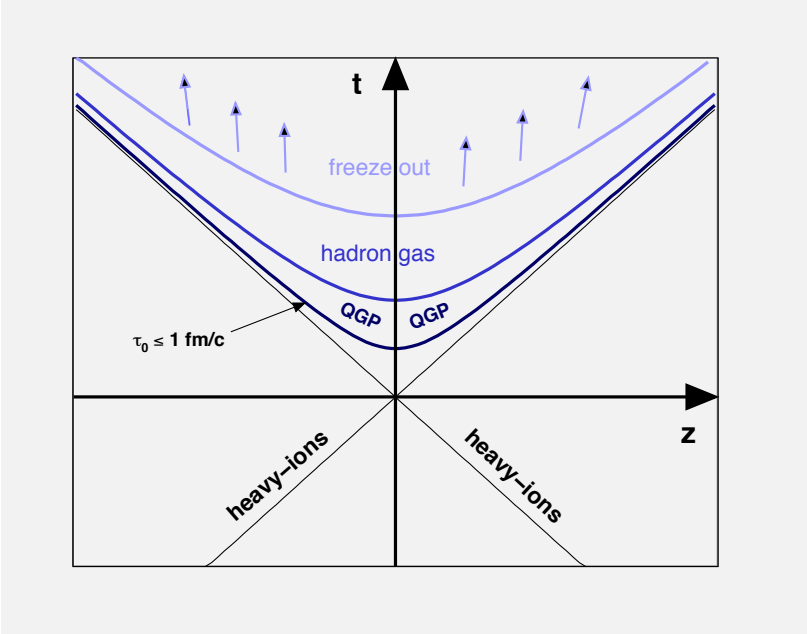

Figure 1.5: The space-time evolution of a relativistic heavy ion collision [27].

1. The initial stage: The two Lorentz contracted heavy nuclei approach each other with more than 99.99% of the speed of light. At such ultra-relativistic energies, the gluon desity in the initial stage is so high that it might be saturated and the matter could be described by Color Glass Condensate (CGC) [28–31], which is still to be established experimentally.

2. The pre-equilibrium stage and thermalization: When the two nuclei collide at high energy, the created energy density is an order of magnitude above the energy density required for the crossover from hadronic to partonic degree of freedom. It takes roughly around 0.1fm/c$\approx 3 \times 10^{-25}$s for the pre-equilibrium bulk matter to achieve local thermalization and form the QGP. The pre-equilibrium state of matter is important in defining the initial condition for the QGP. In particular, the azimuthal correlation of produced particles and the energy loss of jets propagating through the QGP can be significantly influenced by the properties of the initial conditions. If there is gluon saturation before collisions happen, the matter of the pre-equilibrium state is formed by melting the CGC state. Since this is the non-equilibrium matter preceding the QGP, it is called the Glasma [32–35].

3. The QGP expansion and hadronization: Driven by the thermal pressure gradients, the QGP expands and cools very quickly after thermalization. As the system reaches the critical temperature $T_c \approx 170$ MeV, it hadronizes and turns into hadronic matter. It can take more than 10 fm/c for the QGP fireball to expand. If thermalization is achieved and locally maintained during the expansion, the evolution of the QGP and the hadronic matter can be described by hydrodynamics [36]. Hydrodynamics is a macroscopic theory which describes the system using macroscopic variables, such as local energy density, pressure, temperature, and flow velocity. The theory does not require the knowledge of the microscopic dynamics, but needs the equation of state, which gives a relation between the pressure and the energy density. The simplest version is the ideal hydrodynamics [37, 38], which neglects the viscous effects and assumes that the local equilibrium is perfectly maintained during the expansion. Microscopically, this requires that the microscopic scattering time is much shorter than the macroscopic expansion time and that the mean free path is much smaller than the system size. If these requirements are not satisfied, viscous effects play a role. In that case, viscous hydrodynamics may be applicable, as long as the deviation from local equilibrium is small [39, 40]

4. The hadronic expansion and freeze-out: The hadronic matter continues to expand until the system becomes very dilute. These hadrons initially go through inelastic collisions as the system keeps cooling down. When the temperature drops to a certain point, the inelastic collisions between hadrons cease and the yields of different particle species are completely defined. This stage is referred to as "chemical freeze-out" and the temperature at this point is called the chemical freeze-out temperature. As the system cools further, hadrons continue to undergo elastic collisions until individual hadrons stop interacting and decouple from the system. This stage is called "kinetic freeze-out" and the temperature at this moment is the kinetic freeze-out temperature. The hadronic matter can be described by the hadron cascade model, which solves the Boltzmann equation for different hadron species with flavor-dependent cross-sections [41–43]. The hadron cascade model can be combined with hydrodynamics or a parton cascade model (describing QGP) to form a hybrid approach description of the evolution of the QGP expansion together with the hadronic matter cooling.

Although the understanding of different stages becomes clearer, there is currently no model of heavy ion collisions that can predict all aspects of the collision in a self-consistent manner. The theoretical understanding of the heavy ion collision relies on models with their own assumptions, adjusted parameters and uncertainties. All the models need to be tested with more precise and differential measurements as they develop and become more and more realistic.

1.2.2 Signatures of QGP

The signatures of QGP have been investigated for about 30 years. Such signatures include: strangeness enhancement [44, 45], quarkonium suppression [46, 47], jet quenching [48–51], collective flow [37,52,53], critical fluctuations [54], and others. Some of the signatures were already found at the AGS and SPS [16]. But none of these observables can prove unambiguously the formation of QGP since they are influenced by dynamic evolution of the system from the pre-equilibrium stage, QGP stage until the hadronic stage. There were three observables at RHIC that convinced the heavy ion community that the QGP had been created. They were the measurements of the strong anisotropic collective flow, the observation of number of constituent quark scaling of elliptic flow v_2, and the quenching of jets.

1. The strong anisotropic collective flow:

   The detailed information about anisotropic flow will be discussed in Chapter 2. In brief, the elliptic flow v_2 is defined as the 2nd Fourier coefficient of the particle azimuthal distribution.

$$v_2(p_T) = \langle \cos(2\phi_p) \rangle \equiv \frac{\int d\phi_p \, \cos(2\phi_p) \, \frac{d^3N}{dy \, p_T dp_T \, d\phi_p}}{\int d\phi_p \, \frac{d^3N}{dy \, p_T dp_T \, d\phi_p}} \,, \tag{1.2}$$

   where $\frac{d^3N}{dy \, p_T dp_T \, d\phi_p}$ is the particle yield, p_T is the transverse momentum, $y = \frac{1}{2} \ln[(E + p_L)/(E - p_L)]$ is the rapidity of the particle with E and p_L being the energy and the longitudinal momentum, ϕ_p is the particle azimuthal angle with respect to a theoretical plane called the reaction plane. The reaction plane is the plane formed by the beam direction and the impact parameter direction (line connecting the center of the two nuclei).

   In hydrodynamics, the collective flow is driven by the pressure gradients of the fireball, so it can provide access to the equation of state of the produced medium. The elliptic flow is generated mostly during the hot and dense early stage, thus giving information about the QGP phase [37, 55].

   One of the main discoveries at RHIC is that the produced medium displays strong collective behavior [56–59], which, for the first time in the history of nuclear physics, could be well described by ideal hydrodynamics with a QGP equation of state.

   Figure 1.6 shows the comparison of elliptic flow from the experiments and ideal hydrodynamic predictions. The plot is taken from [21]. For $p_T < 1.5$ GeV/c, where more than 98% of the particles are produced, ideal hydrodynamics agrees with the data very well and correctly

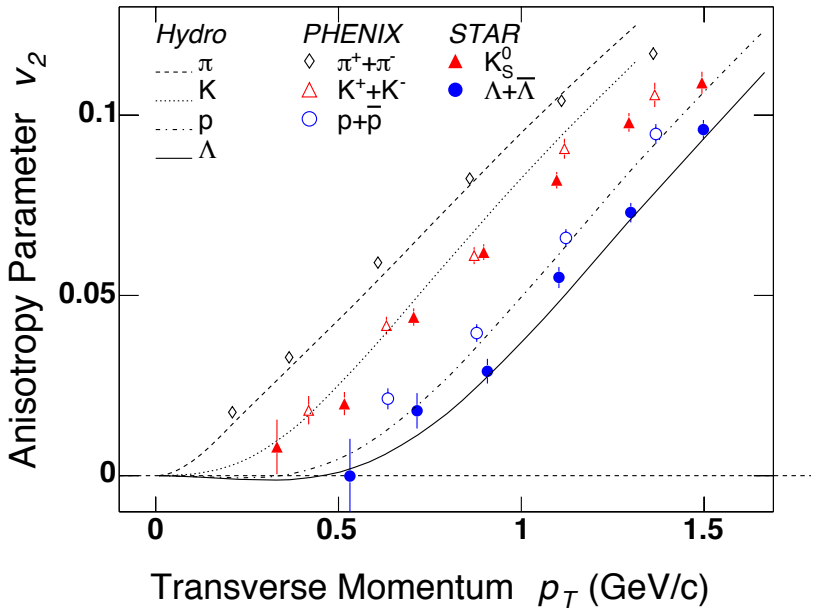

Figure 1.6: The elliptic flow for identified hadrons from STAR and PHENIX compared to hydrodynamic calculations in 200 GeV minimum bias Au+Au [21].

predicts the splitting of different hadron species (mass ordering). This indicates that the matter created at RHIC behaves like a nearly perfect liquid with very small viscosity.

The overall success of the hydrodynamic description suggests that the interactions among constituents in the initial stages are characterized by very short mean free paths and the thermalization of the system is very fast. It must be on a time scale of about 0.6 fm/c [60, 61]. At this time scale, the matter has a temperature of $\sim$ 350 MeV [62], about twice the QGP phase transition temperature predicted by lattice QCD. Although this gives an indirect evidence for the QGP formation, the success of ideal hydrodynamics gives strong evidence for the formation of a thermalized new form of matter at $T \sim 2T_c$.

2. The quark degrees of freedom and number of constituent quark scaling:

   The success of the statistical model for analyzing the relative hadron abundances [64,65] gives some evidence for the QGP phase transition. The ratios between different hadron species are well described by the thermal model, including two parameters, T and μ_B, resulting in a chemical freeze-out temperature T_{ch} = 160 - 170 MeV at RHIC [14]. The number is close to the QCD phase transition temperature ($T_c \approx 170$ MeV) as determined by the lattice QCD calculations. This analysis strongly indicates that most hadrons are produced during the QGP to hadron phase transition stage.

   The direct evidence for quark degrees of freedom can be extracted from the p_T-differential $v_2(p_T)$ measurements for different mesons and baryons. In Figure 1.7, the left hand side shows the v_2 for different mesons and baryons as a function of their transverse kinetic energy $KE_T = \sqrt{p_T^2 + m^2} - m$. We can see two universal v_2 curves for baryons and mesons, respectively [63]. The baryons, which contain three constituent quarks, show stronger v_2 at intermediate p_T ($2.0 < p_T < 4.0$ GeV/c) than mesons, which contain two constituent quarks. This can be

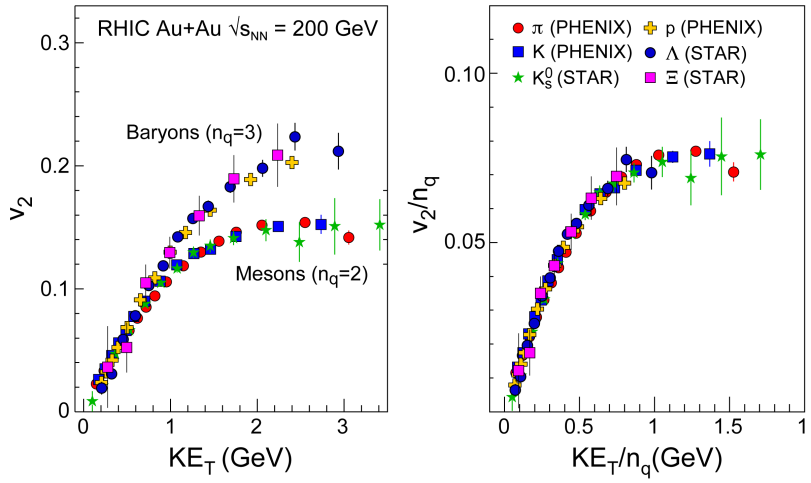

Figure 1.7: Left: The value of v_2 as a function of transverse kinetic energy KE_T for various hadron species. Right: The value of v_2 and KE_T scaled by the number of constituent quark. All the hadron species have the same curve: the differential v_2 per quark. [63].

well explained by the quark recombination model [66–70], in which the collectively flowing baryons and mesons at intermediate p_T are generated by the coalescence of quarks that are collectively flowing in the QGP medium. According to this model, the baryon and meson elliptic flow is expressed in terms of the elliptic flow of quarks:

$$v_2^{(M)}(p_T) = 2v_2^{(q)}(p_T/2); \qquad v_2^{(B)}(p_T) = 3v_2^{(q)}(p_T/3). \tag{1.3}$$

The right hand side plot of Figure 1.7 shows a rescaling of both v_2 and KE_T by the number of constituent quarks (2 for mesons and 3 for hadrons), which leads to a universal v_2 scaling curve for all hadron species. The constituent quark scaling of v_2 suggests that the collectively flowing matter involves quarks directly. The collectivity of quarks is transferred to the collectivity of hadrons by quark recombination. Thus, the flowing medium has quark degrees of freedom.

3. The Jet quenching:

   At the beginning of a heavy ion collision, a pair of energetic fast partons with large p_T can be created from hard scatterings of incoming quarks and gluons. Each parton will finally fragment into a spray of hadrons, which is called a jet. The jet is a useful probe for QGP since the fast parton, which fragments into a jet, has to travel through the hot medium formed in the collision.

   Another exciting result from RHIC, after the discovery of strong elliptic flow, was the observation of a strong suppression of high p_T hadrons in central Au+Au collisions[1], compared with the scaled results from pp collisions [72–74]. Figure 1.8 shows the nuclear modification factor

[1]The heavy ion collisions are classified by their centrality, defined as the percentage of the total nuclear inelastic cross-section, where 0% indicates a head-on (central) collision, and 100% means a grazing (peripheral) collision. The central events have smaller impact parameters b, larger numbers of participant (wounded) nucleons N_{part} and larger number of binary nucleon-nucleon collisions N_{coll} compared to peripheral collisions.

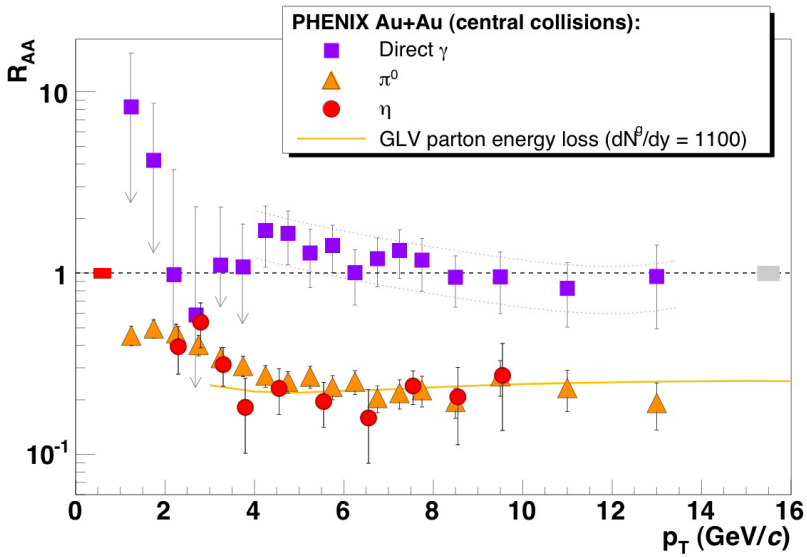

Figure 1.8: The nuclear modification factor R_{AA} as a function of p_T for direct photons, π^0 and η mesons in central Au+Au collisions [71]. The R_{AA} is defined as the cross section per nucleon-nucleon collision measured in heavy ion collisions divided by the cross section measured in pp collisions. If the heavy ion collisions can be viewed as a simple superposition of pp collisions, R_{AA} will be 1.

R_{AA} as a function of p_T for direct photons, π^0 and η mesons in central Au+Au collisions [71]. The R_{AA} is defined as the cross section per nucleon-nucleon collision measured in heavy ion collisions divided by the cross section measured in pp collisions. $R_{AA} = 1$ if the heavy ion collisions can be viewed as a simple superposition of pp collisions. The π^0 and η mesons were observed to have a suppression by a factor of 4-5, which agrees with the theoretical predictions [48, 50, 51, 75]. The theory argued that the QGP formation could lead to large energy loss of fast partons by induced gluon radiation and suppress the production of high p_T hadrons fragmented from these partons. In the measurement, the direct photons are not suppressed, which is expected since they only interact electromagnetically and thus escape from the medium without much interaction.

The angular correlations between a high p_T leading hadron (trigger) with other energetic hadrons also provides strong support for the picture of significant parton energy loss in the QGP [77]. From energy-momentum conservation, the fast partons are always produced in pairs, moving in opposite directions. This leads to back-to-back correlations between jets or high p_T hadrons as shown in Figure 1.9 for pp and dAu collisions (shown with the black line and the red circles). The trigger particles have $4 < p_T < 6$ GeV/c and the associated particles have 2 GeV/c $< p_T < p_T(trigger)$. In central AuAu collisions, we see only one peak around $\Delta\phi = 0$ (near-side), which is in the direction of the fast trigger hadron. This observation can be understood if we assume that the energetic parton pair is created near the surface of the fireball: The near-side outgoing parton escapes from the medium without losing energy and fragments to leading hadrons, however, its inward-traveling partner in the opposite direction needs to go through the QGP medium and loses energy, which makes it not able to contribute

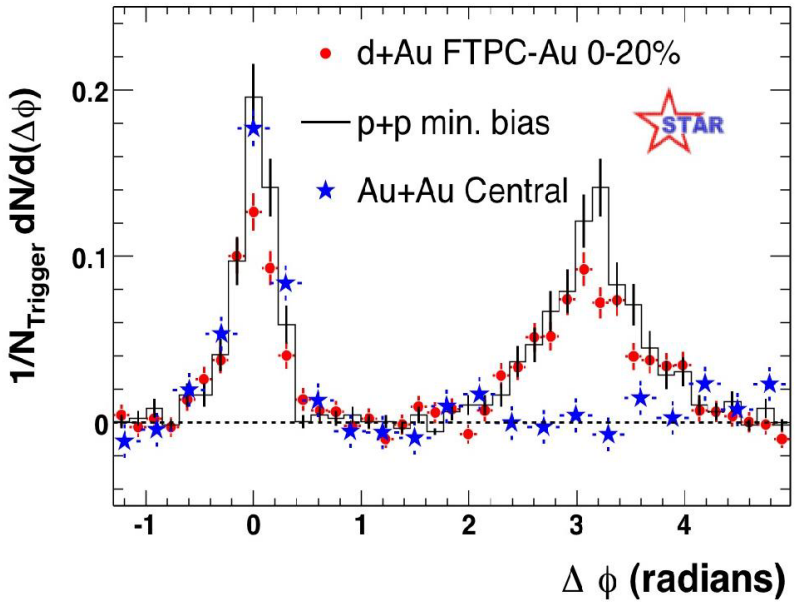

Figure 1.9: The azimuthal angular correlations between high momentum hadrons in pp, dAu and central AuAu collisions [76].

to the energetic hadrons in the away-side ($\Delta\phi = \pi$), and we will see the missing peak in the away-side.

All these signatures are being studied again in detail at the LHC energy for PbPb collisions. The next step in the study of the QGP after the initial discovery is to explore the properties of the medium. Another very interesting question this thesis tries to address is whether QGP is produced also in smaller collision systems, such as in pPb collisions and the peripheral PbPb collisions at LHC.

1.3 Viscous Hydrodynamics

As mentioned in Section 1.2.1, relativistic hydrodynamics is a macroscopic tool to calculate the QGP fireball evolution and predict the soft low p_T particle physics in relativistic heavy ion collisions [37, 38]. The theory is based on the conservation laws of energy, momentum and net charge current. The equations are written as:

$$\partial_\mu T^{\mu\nu}(x) = 0\,, \qquad \partial_\mu N^{\mu}(x) = 0\,.$$

Ideal hydrodynamics assumes local equilibrium, which expresses the energy momentum tensor and the net baryon charge current as: $T^{\mu\nu} = (e+p)u^\mu u^\nu - pg^{\mu\nu}$ and $N^\mu = nu^\mu$. Here, the 14 independent variables (10 from $T^{\mu\nu}$ and 4 from N^μ) in $T^{\mu\nu}$ and N^μ reduce to 6 unknowns (The energy density e, pressure p and, baryon density n, and 3 independent components in the fluid four velocity u^μ). Together with the input of the equation of state (EoS) $p = p(n, e)$, the system is closed. The set of

equations can be solved numerically with proper initial conditions [37, 38].

Viscous hydrodynamics works in a near equilibrium system. In the Landau frame (flow of energy, instead of conserved charge), $T^{\mu\nu}$ and N^{μ} are expressed as: $T^{\mu\nu} = (e+p+\Pi)u^{\mu}u^{\nu} - (p+\Pi)g^{\mu\nu} + \pi^{\mu\nu}$, $N^{\mu} = nu^{\mu} + V^{\mu}$. Here, $\pi^{\mu\nu}$ is the shear stress tensor, Π is the bulk pressure and V^{μ} is the baryon flow. At top RHIC and the LHC energies, the net baryon density n is negligible and V^{μ} is assumed to be zero. Other evolution equations for the viscous terms can be obtained from the 2nd law of thermodynamics or from kinetic theory, which have the following forms [78–82]:

$$\Delta^{\mu\alpha}\Delta^{\nu\beta}D\pi_{\alpha\beta} = -\frac{1}{\tau_{\pi}}(\pi^{\mu\nu} - 2\eta\sigma^{\mu\nu}) - \frac{1}{2}\pi^{\mu\nu}\frac{\eta T}{\tau_{\pi}}\partial_{\gamma}\left(\frac{\tau_{\pi}}{\eta T}u^{\gamma}\right),$$
$$D\Pi = -\frac{1}{\tau_{\Pi}}(\Pi + \zeta\theta) - \frac{1}{2}\Pi\frac{\zeta T}{\tau_{\Pi}}\partial_{\gamma}\left(\frac{\tau_{\Pi}}{\zeta T}u^{\gamma}\right).$$

where $D = u^{\mu}\partial_{\mu}$, $\Delta^{\mu\nu} = g^{\mu\nu} - u^{\mu}u^{\nu}$, $\sigma^{\mu\nu} = \nabla^{\langle\mu}u^{\nu\rangle}$, and $\langle ...\rangle$ denote the symmetric and traceless projection orthogonal to the fluid four velocity u^{μ}, η is the shear viscosity, ζ is the bulk viscosity, and τ_{π} and τ_{Π} are the corresponding relaxation times. These four parameters are the free inputs in viscous hydrodynamic calculation. The magnitude of the anisotropic flow is sensitive to the shear viscosity, therefore, a great effort was made by both theorists and experimentalists to extract the shear viscosity of QGP, including the research done in this thesis.

One of the key inputs for hydrodynamic simulations is the EoS. The state-of-the-art EoS used by many groups is s95p-PCE [83, 84]. Initial entropy/energy density and initial flow velocity are required to start the hydrodynamic evolution at the starting time τ_0. These initial profiles can be provided from different initial condition models or from pre-equilibrium dynamics.

To simplify the numerical simulation, many viscous hydrodynamic calculations assume a specific velocity profile $v_z = z/t$ along the beam direction (Bjorken approximation). This leads to a longitudinal boost invariance and reduces the (3+1)D hydrodynamics to (2+1)D hydrodynamics. The (2+1)D viscous hydrodynamics codes have been developed by several groups since 2007 [85–94]. Recently, several groups [95–101] have further developed (3+1)D viscous hydrodynamics without longitudinal boost invariance. From a comparison between the (2+1)D and (3+1)D codes, it was found that the differences are small for the flow profiles at mid-rapidity [102].

1.4 Motivations and Outline of the Thesis

The first motivation of the thesis is to study the properties of QGP by looking at the charged-particle azimuthal correlations in PbPb collisions at LHC with a much higher collision energy compared to RHIC.

The most important motivation is to find what is the smallest system size in which equilibration and subsequent collective flow can be achieved. The study is done by looking at particle correlations in pPb collisions compared to peripheral PbPb collisions using the number of produced particles as a measure of the size of the system.

There are different methods for studying the correlations and extracting the v_2 signal. The measurement in this thesis is concentrated on multiparticle correlations. One definition of the word "flow" from Oxford dictionary is: "Go from one place to another in a steady stream, typically in large numbers", so it is natural to study flow with multiparticle correlations. We will study how the value of the flow coefficient changes as more and more particle correlations are used.

Chapter 2 introduces the flow-related concepts. The formal definition of flow and non-flow are discussed, together with the latest understanding of the initial state fluctuations and higher order flow harmonics. Different flow analysis methods are introduced and compared. Finally the status of extracting the QGP transport coefficient, shear viscosity over entropy density $\frac{\eta}{s}$, is briefly discussed.

Chapter 3 discusses how the experiment is set up. We will briefly present the LHC specification along with the design and layout of the CMS detector. The trigger system and the data taking are also briefly discussed.

In Chapter 4, the event clean up selections and centrality determination are discussed. The selection criteria for both PbPb and pPb are presented. The event centrality is determined using the Forward Hadron Calorimeter. We will show the estimation of the average value of geometry variables like N_{part} and N_{coll}.

Chapter 5 shows the flow results in PbPb collisions in the 5-50% centrality range. The v_2 is studied as a function of p_T, pseudorapidity and centrality. The fourth and sixth Fourier coefficients in the particle azimuthal distributions, v_4 and v_6, are studied as a function of p_T and centrality.

In Chapter 6, we present the results of v_2 for pPb and PbPb collision events that produce the same number of particles, an event characteristic referred to as "multiplicity". We have results of v_2 from four-particle correlations as a function of p_T and multiplicity. The v_2 from all particle correlations is also shown as a function of multiplicity.

Chapter 7 summarizes the studies in the thesis.

Chapter 2

Anisotropic Flow

2.1 Anisotropic Flow, Initial State Fluctuations and Non-flow

2.1.1 Anisotropic Flow

The idea of anisotropic flow [52] comes from the fact that in a non-central heavy ion collision, the overlap zone of the collision is an almond shape as shown in left hand side plot of Figure 2.1. If no collective behavior takes place in the hot medium, i.e. thermal equilibrium is not reached and the mean free path is large as shown in the left hand side plot of Figure 2.2, then the outgoing particles would be isotropic in azimuth. However, if the mean free path of the particles comprising the QGP is small and thermal equilibrium is reached, the pressure gradient is largest along the impact parameter direction (the line connecting the center of the two nuclei when they collide), or the pressure gradient is larger in-plane than out-of-plane (the plane here means the reaction plane formed by the impact parameter direction and the beam direction), then more particles are collectively pushed (flow) in-plane than out-of-plane. Since the directions of the particles are reflected by $p_T = \sqrt{p_x^2 + p_y^2}$, of course this anisotropy is a momentum space anisotropy. The definition of anisotropic flow is the momentum space anisotropy of outgoing particles. By comparing the anisotropic flow with the initial state coordinate space anisotropy, we can get information about the properties of the produced medium. This is the purpose of studying anisotropic flow.

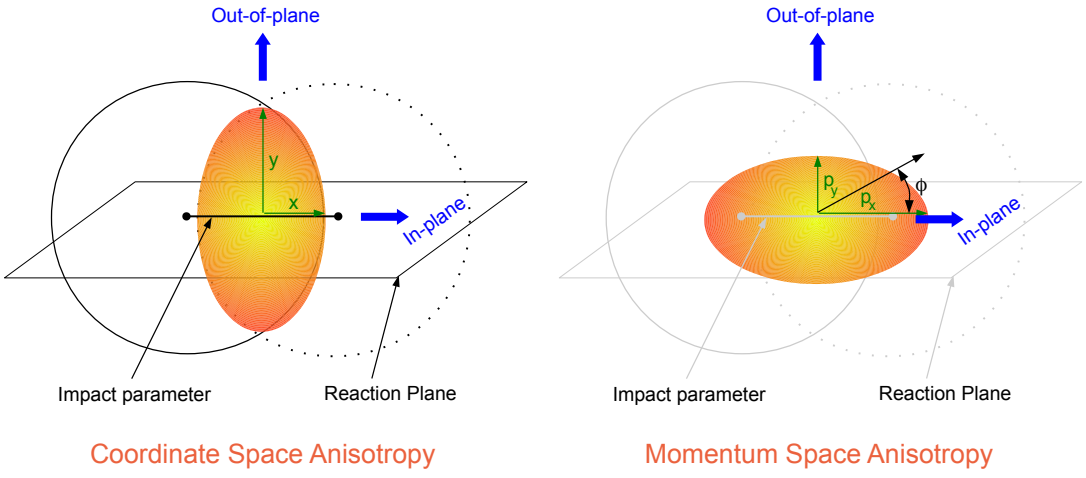

Figure 2.1: Left: The almond overlap zone generated just after a heavy ion collision. Right: The momentum space anisotropy of particles after freeze-out.

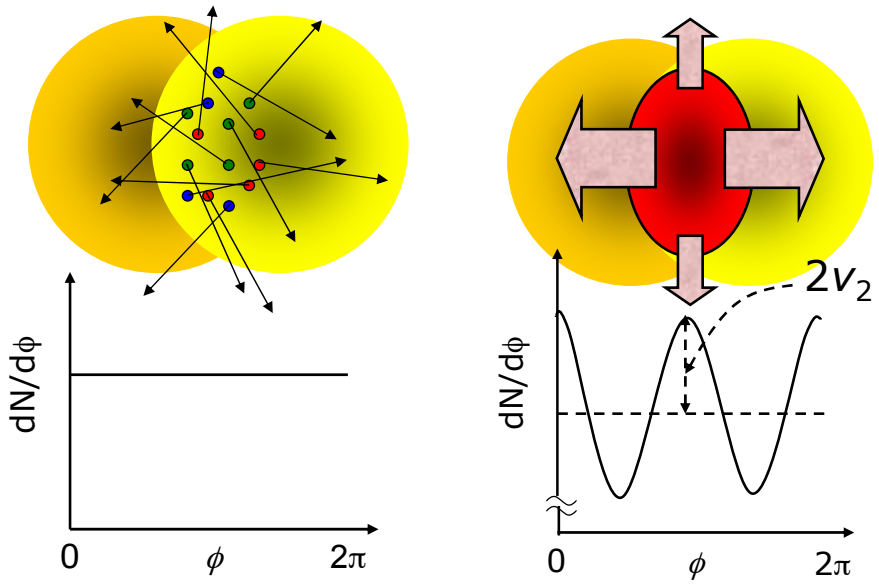

(a) Large mean free path (b) Small mean free path

Figure 2.2: Normalized azimuthal distribution $dN/d\phi$ in a non-central heavy ion collision [27].

Mathematically, the definition of anisotropic flow has to describe the momentum space anisotropy very well. To do that, let us first look at the coordinate space anisotropy as shown in the left hand side of Figure 2.1. We know that the anisotropy of an ellipse-like shape can be described by the eccentricity of the ellipse. One definition (we will see the benefit of this definition later) of the eccentricity could be the dimensionless variable:

$$\epsilon = \frac{y^2 - x^2}{y^2 + x^2} \tag{2.1}$$

with x and y as shown in the left hand side of Figure 2.1.

Similarly, we can define the momentum space anisotropy by:

$$v = \frac{p_x^2 - p_y^2}{p_x^2 + p_y^2} \tag{2.2}$$

with p_x and p_y as shown in the right hand side of Figure 2.1. We can rewrite Equation 2.2:

$$v = \frac{p_x^2 - p_y^2}{p_x^2 + p_y^2} = \frac{(p_T\cos(\phi))^2 - (p_T\sin(\phi))^2}{(p_T\cos(\phi))^2 + (p_T\sin(\phi))^2} = \frac{p_T^2\cos(2\phi)}{p_T^2} = \cos(2\phi) \tag{2.3}$$

Now let us go back to the development of anisotropic flow in history. Two years after the first idea

of flow [52], people found that the flow can be generalized to the Fourier analysis of the particle azimuthal distribution [103]. The azimuthal distribution $\frac{dN}{d\phi}$ of the produced particle is a periodic function, so it is natural to expand it in a Fourier series

$$\frac{dN}{d\phi} = \frac{Nx_0}{2\pi} + \frac{N}{\pi}\sum_{n=1}^{\infty}[x_n \cos(n\phi) + y_n \sin(n\phi)]. \tag{2.4}$$

in which

$$x_n = \int_0^{2\pi} r(\phi)\cos(n\phi)d\phi = \langle\cos(n\phi)\rangle, \tag{2.5}$$

$$y_n = \int_0^{2\pi} r(\phi)\sin(n\phi)d\phi = \langle\sin(n\phi)\rangle. \tag{2.6}$$

Now, for each pair of the Fourier coefficients, x_n and y_n, the corresponding flow harmonics v_n can be defined as:

$$v_n \equiv \sqrt{x_n^2 + y_n^2} \tag{2.7}$$

All the y_n are zero if the colliding nuclei are the same. This is because of the symmetry as shown in Figure 2.1. The probability of producing a particle at the azimuthal angle ϕ is the same for $-\phi$, so that y_n in Equation 2.6, $\langle\sin(n\phi)\rangle$ will be zero since $\sin(n\phi) + \sin[n(-\phi)] = 0$. Also in the symmetric collision case, all the odd coefficients for x_n will be zero since from Figure 2.1, the probability of producing a particle at ϕ is the same for $\phi + \pi$, and x_n in Equation 2.5, $\langle\cos(n\phi)\rangle$ will be zero for odd n since $\cos(n\phi) + \cos[n(\phi + \pi)] = \cos(n\phi) + \cos(n\phi)\cos(n\pi) - \sin(n\phi)\sin(n\pi)$ $= \cos(n\phi) + \cos(n\phi)(-1)^n - \sin(n\phi)\cdot 0 = \cos(n\phi)\cdot(1 + (-1)^n) = 0$ for odd n.

The v_n harmonics can be related to the azimuthal distribution $\frac{dN}{d\phi}$ by:

$$\begin{aligned}\langle\cos(n\phi)\rangle &\equiv \frac{\int_0^{2\pi}\cos(n\phi)\frac{dN}{d\phi}d\phi}{\int_0^{2\pi}\frac{dN}{d\phi}d\phi} \\ &= \frac{\frac{N}{\pi}v_n\int_0^{2\pi}\cos^2(n\phi)d\phi}{v_0} = \frac{Nv_n}{v_0}.\end{aligned} \tag{2.8}$$

where we have used the orthogonality relationship:

$$\int_{-\pi}^{\pi} \sin(mx)\cos(nx)dx = 0$$
$$\int_{-\pi}^{\pi} \cos(mx)\cos(nx)dx = \pi\delta_{mn} \tag{2.9}$$

in which δ_{mn} is the Kronecker delta symbol. If we use the normalized azimuthal distribution $\frac{dN}{d\phi}$, $v_0 = \int_0^{2\pi} \frac{dN}{d\phi} d\phi = \mathrm{N}$, so that:

$$v_n = \langle \cos(n\phi) \rangle \tag{2.10}$$

For n = 1, the harmonic v_1 is called directed flow. The second harmonic $v_2 = \langle \cos(n\phi) \rangle$ is the same as Equation 2.2 for a single particle and called elliptic flow. We can have other higher order harmonics from this generalized definition of anisotropic flow.

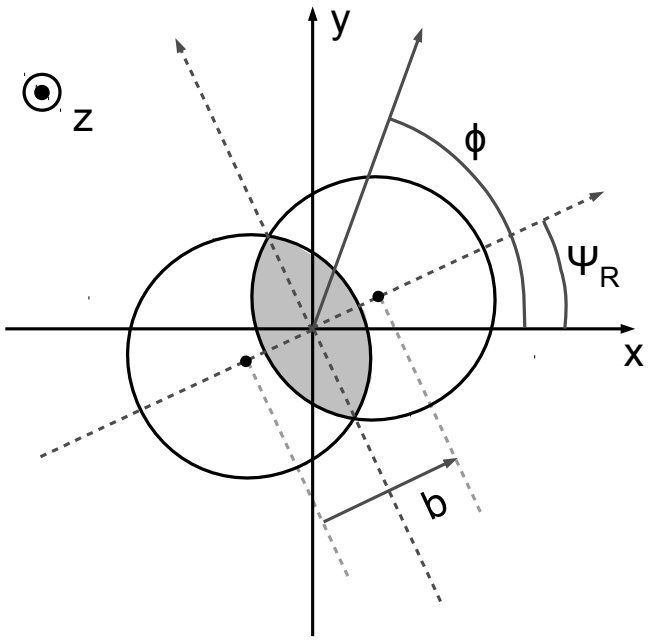

Figure 2.3: A schematic plot of a non-central nucleus-nucleus collision viewed in the plane orthogonal to the beam. The azimuthal angle ϕ, the impact parameter vector b, and the reaction plane angle Ψ_R are shown. The plot is taken from [104].

In practice, the reaction plane should change for different events, as shown in Figure 2.3. All the ϕ angles in the previous discussions are with respect to the reaction plane as shown in Figure 2.1

(the reaction plane angle=0 in that case). Therefore, the Fourier decomposition of the azimuthal distribution should be [103, 105, 106] (also from Equation 2.4 in the previous discussion):

$$\frac{dN}{d\phi} = \frac{N}{2\pi}\left\{1 + \sum_{n=1}^{\infty} 2v_n \cos\left(n\left(\phi - \Psi_R\right)\right)\right\}. \tag{2.11}$$

and from Equation 2.10, the flow coefficients are:

$$v_n = \langle \cos(n(\phi - \Psi_R)) \rangle \tag{2.12}$$

Because the nuclei are so small and traveling so fast, it is not possible to know their positions at the level of a fm, so the impact parameter and the reaction plane angle for each event are not known. From data, we can estimate, based on the distribution of the particles produced in the collision, a symmetry plane angle called the Event Plane (EP) angle. This is done using the flow vector $\mathbf{Q_n}$ [106]:

$$Q_{n,x} = \sum_i w_i \cos(n\phi_i) = |\mathbf{Q_n}| \cos(n\Psi_{EP}) \tag{2.13}$$

$$Q_{n,y} = \sum_i w_i \sin(n\phi_i) = |\mathbf{Q_n}| \sin(2\Psi_{EP}) \tag{2.14}$$

where the sum is over all particles used the event plane calculation. The ϕ_i and w_i are the lab frame azimuthal angle and weight for particle i. The weight is optimized to minimize the uncertainty of event plane angle determination. The event plane angle is the azimuthal angle of the flow vector $\mathbf{Q_n}$ given by:

$$\Psi_{EP} = \left(tan^{-1}\frac{Q_{n,y}}{Q_{n,x}}\right)/n \tag{2.15}$$

Then, flow is estimated using the event plane angle.

The eccentricity of the collision zone also can not be measured directly. It has been a common practice to use smooth, event-averaged initial conditions, for the calculation of the initial spatial asymmetry in the transverse plane. The "standard" eccentricity is given by:

$$\epsilon_{std} = \frac{\langle y^2 \rangle - \langle x^2 \rangle}{\langle y^2 \rangle + \langle x^2 \rangle} \tag{2.16}$$

where $\langle x^2 \rangle$ and $\langle y^2 \rangle$ are second moments of the nucleon distribution in the $x-$ and $y-$direction. The averages are over all the events that are analyzed.

The transverse overlap area of the collision can be estimated by:

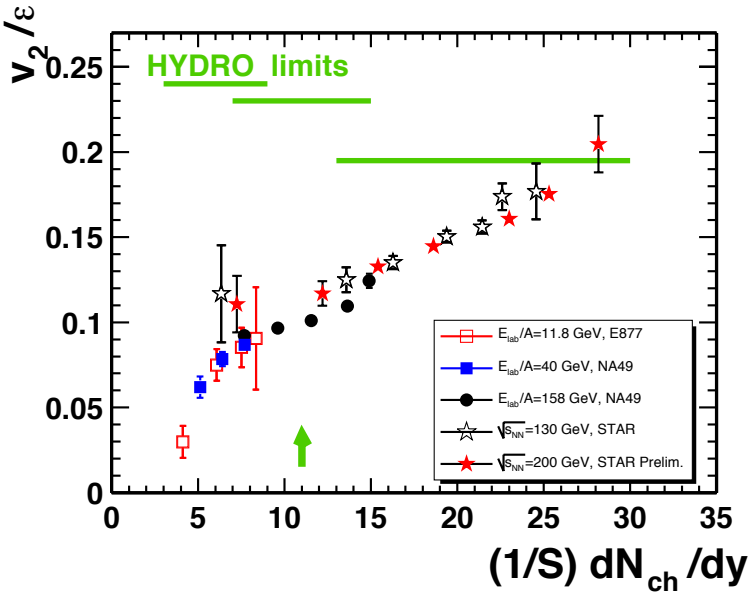

Figure 2.4: The elliptic flow scaled by eccentricity, v_2/ϵ_2, as a function of the particle density, $1/S(dN/dy)$, from different collision systems and different energies [107].

$$S = \pi\sqrt{\langle x^2\rangle}\sqrt{\langle y^2\rangle} \tag{2.17}$$

With these estimates, the behavior of the produced medium in the context of hydrodynamic flow can be studied quantitatively by looking at the ratio of flow and eccentricity compared with the particle density. Figure 2.4 shows the value of v_2/ϵ_2, as a function of the transverse particle density, $1/S(dN/dy)$, from different collision systems and different energies [107]. At the large density region at the top RHIC energies, the elliptic flow value reaches the predicted hydrodynamic limit (ideal hydrodynamics in the limit of zero mean free path). The value of v_2/ϵ_2 is constant, independent of the system size, due to the scale invariance of the theory. The fact that v2/eps2 reaches the ideal hydrodynamics limit is also an indirect signature that the medium produced at RHIC is thermalized very early as assumed in the calculations.

2.1.2 Initial State Fluctuations

The Cu+Cu collision system was also studied at RHIC. Figure 2.5 (left) shows v_2/ϵ_{std}, as a function of the particle density for Cu+Cu and Au+Au collisions. One can see that the results from the two systems are far away from each other. However, if the ϵ_{std} is replaced by ϵ_{part}, the results in the two systems agree well as shown in the right hand side plot of Figure 2.5. The participant eccentricity [108, 109] is calculated from the Monte Carlo (MC) Glauber model, which will be discussed in Chapter 4.

The nucleons that participate in inelastic interactions are called "participants". A schematic view of a PbPb collision with an impact parameter b = 6 fm, as obtained from the Glauber model, is

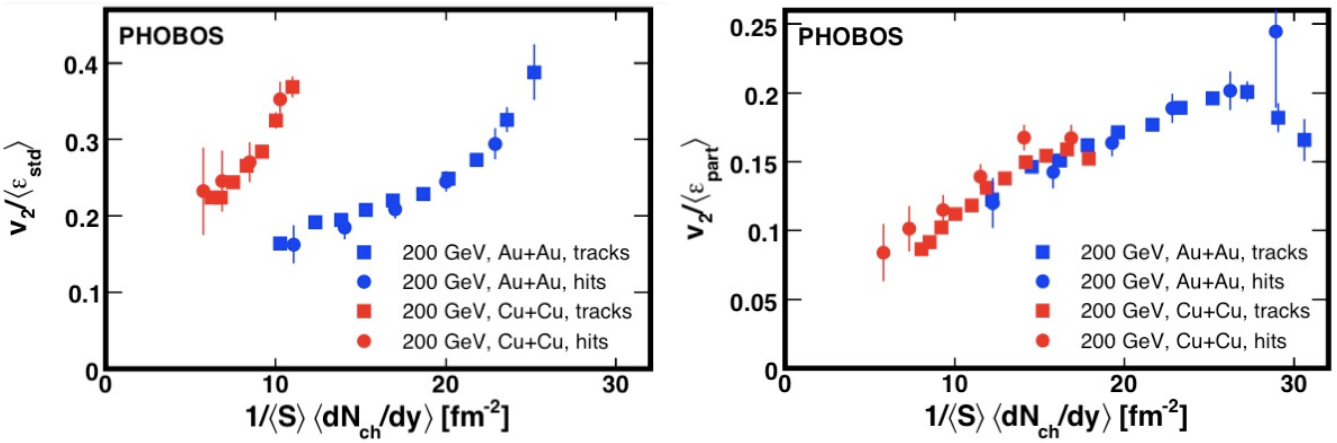

Figure 2.5: Left: The value of v_2/ϵ_{std}, as a function of the particle density for Cu+Cu and Au+Au collisions. Right: The value of v_2/ϵ_{part}, as a function of the particle density for Cu+Cu and Au+Au collisions [108].

shown in Figure 2.6. Each circle represents a nucleon from the incoming nuclei. They are drawn with different colors to distinguish the two nuclei. The filled circles are the ones that are determined to undergo at least an inelastic collision in the MC implementation of the Glauber model. These are the participants in one particular simulated event. One can see that the initial interaction zone as determined by the spatial distribution of the participants (filled circles) is no longer regular in shape and is not necessarily symmetric with respect to the reaction plane angle Ψ_R. In each event, one can evaluate the variances $\sigma_x^2 = \langle x^2\rangle - \langle x\rangle^2$, $\sigma_y^2 = \langle y^2\rangle - \langle y\rangle^2$, and the covariance $\sigma_{xy} = \langle xy\rangle - \langle y\rangle\langle x\rangle$ of the participant distributions projected on the x and y axes. One can then find a frame x'-y' that minimizes $\sigma_{x'}$, and define a "participant plane" using the beam direction and the x' axis. To characterize the geometry of the initial state of the collision, the eccentricity of the participant zone, ϵ_{part}, is defined as:

$$\epsilon_{part} = \frac{\sigma_{y'}^2 - \sigma_{x'}^2}{\sigma_{y'}^2 + \sigma_{x'}^2} = \frac{\sqrt{\left(\sigma_y^2 - \sigma_x^2\right)^2 + 4\sigma_{xy}^2}}{\sigma_y^2 + \sigma_x^2}, \tag{2.18}$$

The transverse overlap area of the collision is then:

$$S = \pi\sigma_{x'}\sigma_{y'} = \pi\sqrt{\sigma_x^2\sigma_y^2 - \sigma_{xy}^2} \tag{2.19}$$

These studies show that the produced initial symmetry plane of the system after collision is the participant plane, not the reaction plane. The participant plane fluctuates about the reaction plane on an event-by-event basis. Neither of the two plane angles can be measured experimentally, with participant plane angle calculated using the position of participants and reaction plane angle from the impact parameter and beam direction. Experimentally, the plane determined from the produced particles is an estimate of the participant plane. However, the plane determined from the spectator nucleons is an estimate of the reaction plane.

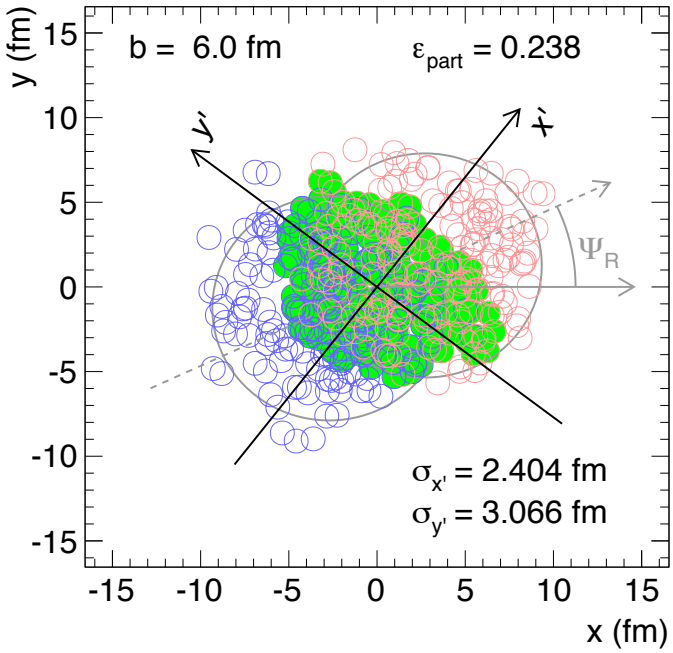

Figure 2.6: A schematic view of a PbPb collision with an impact parameter $b = 6$ fm as obtained from the Glauber model. The nucleons that participate in inelastic interactions are marked with filled circles. The x and y coordinates represent the laboratory frame, while x' and y' represent the frame that is aligned with the axes of the ellipse in the participant zone. The participant eccentricity ϵ_{part} and the standard deviations of the participant spatial distribution $\sigma_{y'}$ and $\sigma_{x'}$ from which the transverse overlap area of the two nuclei is calculated are also shown. The angle Ψ_R denotes the orientation of the reaction plane. The Figure is from [104].

Understanding these initial state fluctuation effects is very important for the interpretation of the anisotropic flow results. Recognizing the importance of the fluctuation effects is relatively recent (2006 - 2010), and in the last few years a lot of new measurements have emerged. If we look at the Figure 2.6 again and think about the fluctuations of the position of these participant nucleons, it is possible that the participant zone might be a triangular shape in some cases, or some other shapes. Therefore, there should be v_3, v_4 and other higher order harmonics because of fluctuations. Again, if the shape is triangular, it will not look like an elliptical shape, so when ϵ_3 is large, ϵ_2 will be small. There should be an anti-correlation between ϵ_2 and ϵ_3. If these anti-correlations also could be observed in the final momentum space by looking at the correlations of the v_2 and v_3 flow coefficients, it would be a good test of the hydrodynamic description. Also, the ϵ_{part} can vary a lot for different events even with the same impact parameter. Thus, the measured v_2 coefficient should also have large event-by-event fluctuations. The central PbPb collision could have v_n because of fluctuations, though the collision shape would be isotropic if we consider nuclei to be uniform spheres colliding head-on in this case. Similarly, because of fluctuations, flow is possible to exist in pPb collisions, which will be an important part of the thesis.

Higher Order Flow Harmonics

As discussed above, there could be triangularity for $n = 3$ and other higher order coordinate space asymmetry from initial state fluctuations. Let us denote ϵ_{part} to be ϵ_2 because it is for $n = 2$, then we could have ϵ_3, ϵ_4, and other ϵ_n.

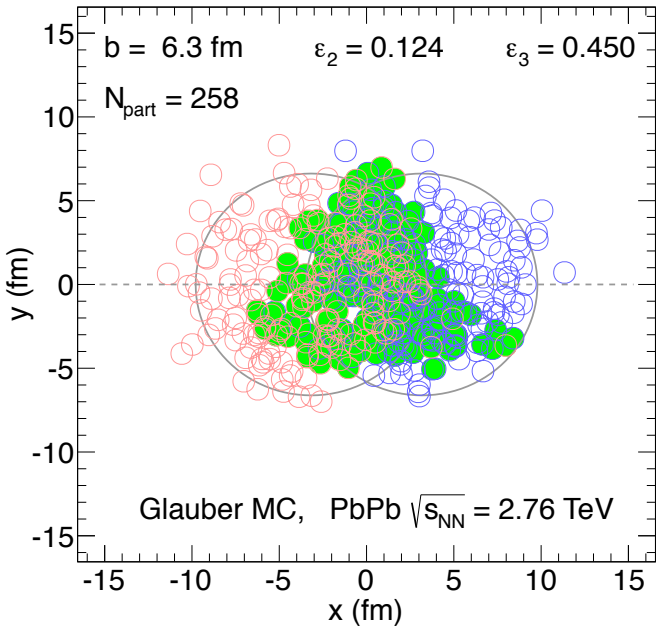

Figure 2.7: A schematic view of a PbPb collision with large triangularity ϵ_3.

The definition of ϵ_{part} of ϵ_2 in Equation 2.18 can be rewritten as:

$$\epsilon_2 = -\frac{\langle r^2 \cos(n(\phi - \Psi_2))\rangle}{\langle r^2 \rangle} \tag{2.20}$$

where, r and ϕ are the polar coordinate positions of participating nucleons, and Ψ_n is the participant plane angle in a model. Then the definition of ϵ_n for higher order harmonics can be generalized to:

$$\epsilon_n = -\frac{\langle r^n \cos(n(\phi - \Psi_n))\rangle}{\langle r^n \rangle} \tag{2.21}$$

Figure 2.7 shows an example of a PbPb event with large ϵ_3 and small ϵ_2 from the Glauber model. One can see clearly that the triangular shape, shown by filled green circles which represent the participant nucleons, is from the fluctuations of the nucleon positions. The pressure gradients are different in different directions. There are three short axes from which more particles will be produced if the medium is thermalized and hydrodynamics applicable. Thus, a large v_3 can be produced from this event. Similarly, some events will have large quadrangular flow, v_4, or pentagonal flow, v_5, or hexagonal flow, v_6. The results of these higher order harmonics give more constraints to theories and may provide detailed information about the structure of the initial state configuration.

Initial State Asymmetry in pPb Collisions

It is also possible that a large ϵ_2 or ϵ_n is produced in a pPb collision because of fluctuations. Figure 2.8 (left) shows a pPb event with large ϵ_2. The N_{part} is 21, which means the proton collides with 20 nucleons in the Pb nucleus. There are 20 nucleon-nucleon collisions ($N_{coll} = 20$) and the number of participant nucleons is 21. Similarly, the right hand side of Figure 2.8 shows a pPb event with large ϵ_3.

If the produced medium after a pPb collision is thermally equilibrated (at least a local thermal equilibrium), it could be described by hydrodynamics and we may find v_n signals in pPb collisions. However, before the measurements were available, it was assumed that the volume of the produced medium in pPb collisions was not large enough to be an equilibrated system. Whether this is the case is still being investigated. This thesis provides an experimental study of flow observables in different collision systems and demostrates that there are remarkable similarities between PbPb and pPb collisions that produce the same number of final-state particles.

2.1.3 Non-Flow

In the flow analysis, we want to estimate the particle correlations with respect to a symmetry plane, like the participant plane, Ψ_n. However, there are always some correlations independent of Ψ_n. These correlations are called non-flow correlations.

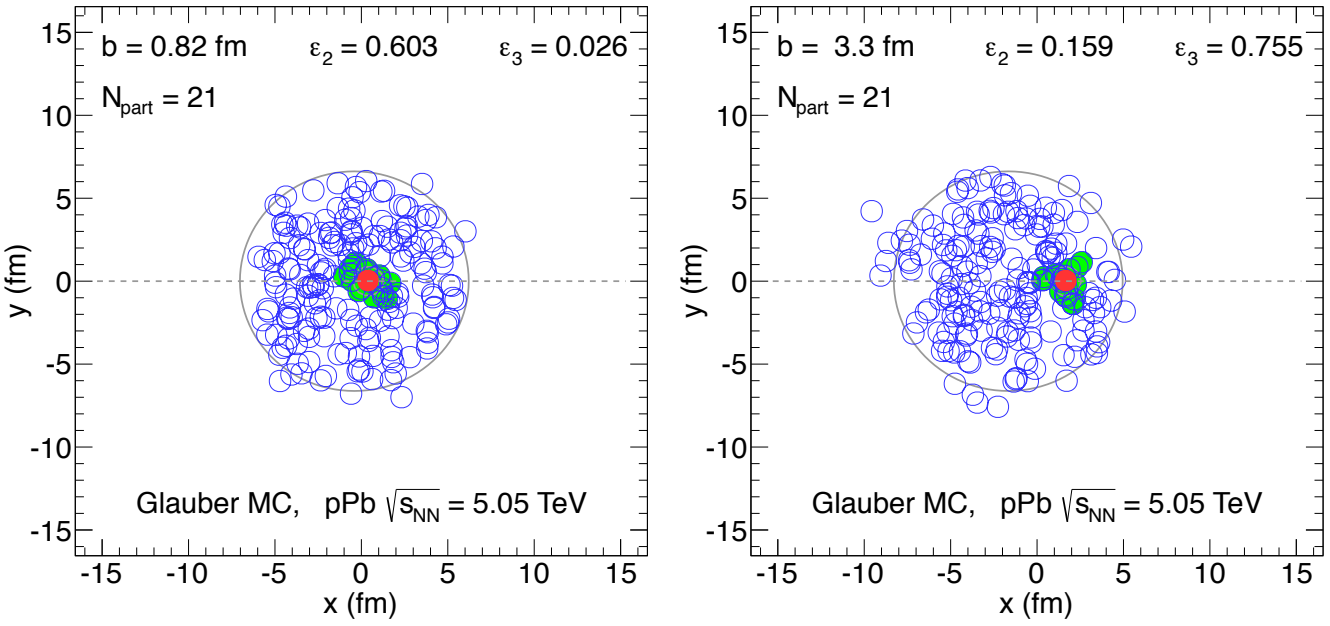

Figure 2.8: Left: A pPb collision with large ϵ_2. Right: A pPb collision with large ϵ_3.

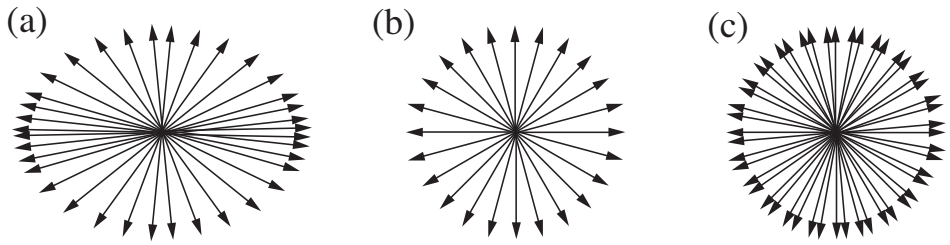

Figure 2.9: The particle distributions in the transverse plane, where for a) $v_2 > 0, v_2\{2\} > 0$, b) $v_2 = 0, v_2\{2\} = 0$, c) $v_2 = 0, v_2\{2\} > 0$. The plot is from [110].

As an example illustrating the non-flow, let us use the two-particle correlation method for v_2 analysis:

$$\begin{aligned}\langle\langle\cos 2(\phi_1 - \phi_2)\rangle\rangle &= \langle\langle\cos 2((\phi_1 - \Psi_2) - (\phi_2 - \Psi_2))\rangle\rangle \\ &= \langle\langle\cos 2(\phi_1 - \Psi_2)\rangle\langle\cos 2(\phi_2 - \Psi_2)\rangle + \delta_2\rangle, \\ &= \langle v_2^2 + \delta_2\rangle\end{aligned} \tag{2.22}$$

where the double brackets denote an average over all particles in an event, and then an average over all events. We have factorized the azimuthal correlation with respect to the Ψ_2, v_2, and a correlation independent of Ψ_2, the non-flow term δ_2. If δ_2 is small, Equation 2.22 can be used to measure $\langle v_2^2\rangle$. However, the δ_2 term is not negligible in general [111–114].

Figure 2.9 shows an example of different particle distributions in the transverse plane. Figure 2.9a is an anisotropic distribution and both $v_2 = \langle\cos 2\phi\rangle$ and the two-particle correlation $v_2\{2\} =$

$\sqrt{\langle \cos 2(\phi_1 - \phi_2) \rangle}$ are positive. Figure 2.9b shows an isotropic distribution for which $v_2 = 0$ and $v_2\{2\} = 0$. Figure 2.9c shows two symmetric distributions rotated with respect to each other which give $v_2 = 0$ and $v_2\{2\} > 0$. This example shows how the non-flow contributions from sources like resonance decays or jets can affect the v_2 measured from two-particle correlations. It was shown in [113] that for n-particle correlations, the non-flow $\delta_n \propto 1/M^{n-1}$ and the $v_2\{n\}$ is a good estimate of v_2 only if $v_2 \gg 1/M^{(n-1)/n}$. For all-particle correlations, which we denote as $v_2\{\infty\}$, it requires $v_2 \gg 1/M$. The meaning of M is the number particles in an event.

Another technique used to reduce non-flow is applying a pseudorapidity[1] gap between the two correlated particles. The correlation with a large gap will remove most of the non-flow in the short range correlations. This technique is further discussed in Section 2.2.

2.2 Flow Analysis Methods

As was discussed in Section 2.1, anisotropic flow are observables that measure the asymmetry of the azimuthal distribution of particles with respect to symmetry planes of an event. So, it is natural to construct these symmetry planes from data and estimate different flow coefficients from them by correlating particles with these planes. This method is called the event plane method. Since particles are correlated with a common plane in an event if there is anisotropic flow, of course these particles are correlated with each other. So we can study the anisotropic flow, without constructing any symmetry plane, by looking at the correlations between these particles. We will discuss flow from two-particle and four-particle correlations in the cumulant method, and flow from all-particle correlations in the Lee-Yang Zeros method.

2.2.1 Event Plane Method

In this method [106], the event plane angle for each order n, Ψ_{EP}, is calculated as an estimation of the participant plane angle by:

$$\Psi_{EP} = \left(tan^{-1} \frac{Q_{n,y}}{Q_{n,x}} \right) / n \tag{2.23}$$

with $Q_{n,x}$ and $Q_{n,y}$ from:

$$Q_{n,x} = \sum_i w_i \cos(n\phi_i) = |\mathbf{Q_n}| \cos(n\Psi_{EP}) \tag{2.24}$$

$$Q_{n,y} = \sum_i w_i \sin(n\phi_i) = |\mathbf{Q_n}| \sin(2\Psi_{EP}) \tag{2.25}$$

[1]The pseudorapidity of a particle is defined as $\eta = -\ln[\tan(\theta/2)]$, with the polar angle θ defined relative to the beam axis

as already shown in Equation 2.13 and 2.14.

The flow coefficient v_n from this method is then estimated as:

$$v_n\{EP\} = \frac{v_n^{\text{obs}}\{EP\}}{R_n} = \frac{\langle \cos n(\phi - \Psi_{EP})\rangle}{\langle \cos n(\Psi_{EP} - \Psi_n)\rangle} \tag{2.26}$$

With R_n being event plane resolution:

$$R_n = \langle \cos n\,(\Psi_{EP} - \Psi_n)\rangle \tag{2.27}$$

and observed v_n before resolution correction being:

$$v_n^{obs}\,\{EP\} = \langle \cos n\,(\phi - \Psi_{EP})\rangle \tag{2.28}$$

The ϕ is the particle azimuthal angle. The Ψ_n is the participant plane angle for order n, which is not possible to know in experiments. A method called the sub-event method is usually used to estimate the resolution:

$$R_n = \sqrt{\langle \cos[n(\Psi_{EP}^A - \Psi_{EP}^B)]\rangle}. \tag{2.29}$$

with Ψ_{EP}^A and Ψ_{EP}^B being the event plane angle from sub-event A and B. In a real data analysis, we usually use particles with $\eta > 0$ in an event as one sub-event, and $\eta < 0$ as another sub-event of the event. When the observed v_n, $v_n^{obs}\,\{EP\}$, is calculated, the ϕ angle and Ψ_{EP} will also be from different sub-events. If the ϕ is from particles with $\eta > 0$, the Ψ_{EP} should be calculated from particles with $\eta < 0$. Similarly, if the ϕ is from particles with $\eta < 0$, the Ψ_{EP} should be from particles with $\eta > 0$. With this method we could avoid auto-correlations, which could occur if we use a particle to estimate the event plane angle and then correlate this particle with the estimated event plane angle. The non-flow in the short range correlations could also be removed with this technique since there is an η gap between the particles used estimate the event plane angle and the particles used to calculate the correlations.

2.2.2 Long-Range Two-Particle Correlation Method

The flow coefficients from two-particle correlations can be estimated directly by $\langle \cos(n(\phi_1 - \phi_2))\rangle$. But since there is no pseudorapidity gap applied between the two particles ϕ_1 and ϕ_2, there is a large contribution from the short-range non-flow correlations from this method.

In practice, we first construct a two-particle correlation function following the procedure established in Refs. [115–117]. The "trigger" particles are defined as particles within a given transverse momentum p_T^{trig} range. N_{trig} is the number of trigger particles in the event. Particle pairs are formed by associating each trigger particle with the remaining particles from a specified p_T^{assoc} range. The

per-trigger-particle associated yield is defined as

$$\frac{1}{N_{trig}}\frac{d^2N^{pair}}{d\Delta\eta\, d\Delta\phi} = B(0,0) \times \frac{S(\Delta\eta,\Delta\phi)}{B(\Delta\eta,\Delta\phi)}, \tag{2.30}$$

where $\Delta\eta$ and $\Delta\phi$ are the differences in η and ϕ of the particle pair. The signal pair distribution, $S(\Delta\eta,\Delta\phi)$, is the yield of particle pairs normalized by N_{trig} from the same event,

$$S(\Delta\eta,\Delta\phi) = \frac{1}{N_{trig}}\frac{d^2N^{same}}{d\Delta\eta\, d\Delta\phi}\ . \tag{2.31}$$

The mixed-event pair distribution,

$$B(\Delta\eta,\Delta\phi) = \frac{1}{N_{trig}}\frac{d^2N^{mix}}{d\Delta\eta\, d\Delta\phi}\ , \tag{2.32}$$

is constructed by pairing the trigger particles in each event with the associated particles from different events. Here, N^{mix} is the number of pairs taken from the mixed events.

The flow coefficients are determined from a Fourier decomposition of the long-range (large η gap) two-particle $\Delta\phi$ correlation function,

$$\frac{1}{N_{trig}}\frac{dN^{pair}}{d\Delta\phi} = \frac{N_{assoc}}{2\pi}\left[1 + \sum_n 2V_{n\Delta}\cos(n\Delta\phi)\right], \tag{2.33}$$

as described in Refs. [115,116], where $V_{n\Delta}$ are the Fourier coefficients and N_{assoc} represents the total number of pairs per trigger particle for a given $(p_T^{trig}, p_T^{assoc})$ bin. A minimum $\Delta\eta$ of 2 units is applied to remove short-range correlations. The flow coefficients $v_n\{2, |\Delta\eta| > 2\}$ from the two-particle correlation method can be extracted as a function of p_T from the fitted Fourier coefficients,

$$v_n\{2, |\Delta\eta| > 2\}(p_T) = \frac{V_{n\Delta}(p_T, p_T^{ref})}{\sqrt{V_{n\Delta}(p_T^{ref}, p_T^{ref})}}, \tag{2.34}$$

Here, a fixed p_T^{ref} range for the "reference particles" is chosen to include most of the low- and mid-p_T particles. The v_n coefficients in a broad rapidity and p_T window are often referred to as "integrated flow". They are extracted by averaging the values of v_n in small rapidity and p_T bins weighted by the number of particles in these bins.

This method is still affected by the event-by-event flow fluctuations.

2.2.3 Cumulant Method

Flow measurement is contaminated by direct correlations between particles which do not originate from their correlation with the participant plane. Such correlations are generically called non-flow correlations as discussed in Section 2.1. It is therefore important in flow measurements either to

estimate or to minimize those contributions in order to measure the "true" flow. The cumulant methods have been developed based on the fact that anisotropic flow is a correlation among all particles in an event while non-flow effects originate from a few particle correlations. The principle of the cumulant method is that when cumulants of higher order are considered, the contribution of non-flow effects from lower order correlations are reduced [113, 118].

There are two different cumulant methods. The first one is based on the generating function [113, 118] . The second one was developed recently and called the Q-Cumulant method [119]. The advantage of this new method is that it provides fast and exact (no approximations) non-biased (no interference between different harmonics) estimates for cumulants, as compared to the version of the cumulant method that employs generating functions. We will discuss the detail of the second one in the following.

The cumulants are expressed in terms of the moments of the magnitude of the corresponding flow vector Q_n

$$Q_n \equiv \sum_{i=1}^{M} e^{in\phi_i} \tag{2.35}$$

where M is the number of particles in each event.

Reference Flow

In order to calculate the reference flow, i.e., the value integrated over p_T, four steps are needed. First, the single-event average 2- and 4-particle azimuthal correlations are defined, respectively as

$$\langle 2 \rangle = \frac{|Q_n|^2 - M}{M(M-1)} \tag{2.36}$$

$$\begin{aligned} \langle 4 \rangle =& \frac{|Q_n|^4 + |Q_{2n}|^2 - 2 \cdot \Re e \left[Q_{2n} Q_n^* Q_n^* \right]}{M(M-1)(M-2)(M-3)} \\ & - 2 \frac{2(M-2) \cdot |Q_n|^2 - M(M-3)}{M(M-1)(M-2)(M-3)} \end{aligned} \tag{2.37}$$

Second, the average over all events can be estimated by the following procedure

$$\begin{aligned} \langle\langle 2 \rangle\rangle &\equiv \langle\langle e^{in(\phi_1 - \phi_2)} \rangle\rangle \\ &\equiv \frac{\sum_{\text{event}} \left(W_{\langle 2 \rangle} \right)_i \langle 2 \rangle_i}{\sum_{\text{event}} \left(W_{\langle 2 \rangle} \right)_i} \end{aligned} \tag{2.38}$$

$$\begin{aligned} \langle\langle 4 \rangle\rangle &\equiv \langle\langle e^{in(\phi_1 + \phi_2 - \phi_3 - \phi_4)} \rangle\rangle \\ &\equiv \frac{\sum_{\text{event}} \left(W_{\langle 4 \rangle} \right)_i \langle 4 \rangle_i}{\sum_{\text{event}} \left(W_{\langle 4 \rangle} \right)_i} \end{aligned} \tag{2.39}$$

where double brackets denote an average, first over all particles and then over all events. The

weights, $W_{\langle 2\rangle}$ and $W_{\langle 4\rangle}$

$$W_{\langle 2\rangle} \equiv M(M-1) \tag{2.40}$$

$$W_{\langle 4\rangle} \equiv M(M-1)(M-2)(M-3) \tag{2.41}$$

are used to minimize the effect of multiplicity fluctuations in the event sample on the estimates of 2- and 4-particle correlations.

Third, the 2- and 4-particle cumulants without detector bias can be formulated as:

$$c_n\{2\} = \langle\langle 2\rangle\rangle \tag{2.42}$$

$$c_n\{4\} = \langle\langle 4\rangle\rangle - 2 \cdot \langle\langle 2\rangle\rangle^2 \tag{2.43}$$

Finally, the reference flow v_n can be calculated from the two-particle and four-particle cumulants, as

$$v_n\{2\} = \sqrt{c_n\{2\}} \tag{2.44}$$

$$v_n\{4\} = \sqrt[4]{-c_n\{4\}} \tag{2.45}$$

Differential Flow

Similar to the procedure for estimating the reference flow, four steps are needed to calculate the differential flow as a function of p_T. Two additional vectors, p_n and q_n, need to be defined, with a similar role as Q_n in the reference flow,

$$p_n \equiv \sum_{i=1}^{m_p} e^{in\psi_i} \tag{2.46}$$

$$q_n \equiv \sum_{i=1}^{m_q} e^{in\psi_i} \tag{2.47}$$

where m_p is the number of particles of interest and m_q is the number of particles labeled as both particles of interest and reference flow particles. The q vector is introduced in order to subtract effects of autocorrelations.

The first step to extract the differential flow is to calculate the reduced (i.e., restricted to a sub-phase space window of interest) single-event average 2- and 4-particle correlations, respectively given by

$$\langle 2'\rangle = \frac{p_n Q_n^* - m_q}{m_p M - m_q} \tag{2.48}$$

$$\begin{aligned}\langle 4'\rangle =& [p_n Q_n Q_n^* Q_n^* - q_{2n} Q_n^* Q_n^* - p_n Q_n Q_{2n}^* \\ & - 2 \cdot M p_n Q_n^* - 2 \cdot m_q |Q_n|^2 + 7 \cdot q_n Q_n^* \\ & - Q_n q_n^* + q_{2n} Q_{2n}^* + 2 \cdot p_n Q_n^* + 2 \cdot m_q M \\ & - 6 \cdot m_q]/[(m_p M - 3m_q)(M-1)(M-2)].\end{aligned} \tag{2.49}$$

The next step is to estimate the event average, i.e.,

$$\langle\langle 2' \rangle\rangle = \frac{\sum_{\text{event}} (w_{\langle 2' \rangle})_i \langle 2' \rangle_i}{\sum_{i=1}^{N} (w_{\langle 2' \rangle})_i} \tag{2.50}$$

$$\langle\langle 4' \rangle\rangle = \frac{\sum_{\text{event}} (w_{\langle 4' \rangle})_i \langle 4' \rangle_i}{\sum_{i=1}^{N} (w_{\langle 4' \rangle})_i} \tag{2.51}$$

where the multiplicity weights are given by

$$w_{\langle 2' \rangle} \equiv m_p M - m_q \tag{2.52}$$

$$w_{\langle 4' \rangle} \equiv (m_p M - 3m_q)(M-1)(M-2) \tag{2.53}$$

The third step is the calculation of the 2- and 4-particle differential cumulants which, in the case without detector bias (uniform azimuthal acceptance) are given by

$$d_n\{2\} = \langle\langle 2' \rangle\rangle \tag{2.54}$$

$$d_n\{4\} = \langle\langle 4' \rangle\rangle - 2 \cdot \langle\langle 2' \rangle\rangle \langle\langle 2 \rangle\rangle \tag{2.55}$$

.

Finally, the differential flow harmonics obtained from second- and fourth-order cumulants, $v_n'\{2\}$ and $v_n'\{4\}$, respectively, can be expressed as

$$v_n'\{2\} = \frac{d_n\{2\}}{\sqrt{c_n\{2\}}} \tag{2.56}$$

$$v_n'\{4\} = -\frac{d_n\{4\}}{(-c_n\{4\})^{3/4}} \tag{2.57}$$

Each one gives an independent estimate of the same differential flow harmonic v_n'.

2.2.4 Lee-Yang Zeros Method

The Lee-Yang zeros method studies directly the large-order behavior of the cumulant expansion. This method is driven by the idea that correlating a large number of particles is the most natural way of studying genuine collective motion in the expanding medium. This flow behavior is determined by finding the location of the zeros of a complex generating function, in very close analogy to the theory of phase transitions formulated by Lee and Yang [120, 121]. For a phase transition near the critical point, long range correlations appear in the system, and zeros of the grand partition function come close to the real axis as the size of the system increases. In a medium with anisotropic flow, like QGP, a similar mathematical phenomenon occurs.

Consider a generating function of azimuthal correlations [114, 122],

$$G^{\theta}(ir) = \langle \prod_{j=1}^{M} [1 + irw_j \cos(n(\phi_j - \theta))] \rangle \tag{2.58}$$

where r is a real positive variable, $0 \leq \theta < \pi/n$ is an input angle and the w_j is the weight attributed to the j^{th} particle to maximize the signal. The product runs over all particles in an event and the average denoted by the angular brackets is over all events. If there is no collective flow the system consists of independent subsystems, and the product can be factorized to a product over the subsystems. Then the zeroes of G^{θ} are the same as those of the subsystem function and their positions are independent of the system size (multiplicity). On the contrary, when there is collective flow, the generating function can no longer be factorized and the positions of its zeroes approach the origin as the multiplicity increases. Therefore, the behavior of the zeroes reflects the presence or absence of collective flow in the system.

Flow Vector

The flow vector is a two dimensional vector $\mathbf{Q} = (Q_x, Q_y)$

$$Q_x = \sum_{j=1}^{M} w_j \cos(n\phi_j), \qquad Q_y = \sum_{j=1}^{M} w_j \sin(n\phi_j),$$

where n is the Fourier harmonic of interest. The sum runs over all detected particles, here tracks, and M is the total detected particle multiplicity of the event. The ϕ_j are the azimuthal angles of the particles with respect to a fixed laboratory frame.

The coefficients w_j are weights that can depend on transverse momentum, particle mass, and pseudorapidity. They are chosen in such a way to maximize the flow signal and hence minimize statistical error. For events with different multiplicities, one may choose weights that depend on the particle multiplicity M.

Once determined, the flow vector is projected on a fixed arbitrary direction that makes an angle of $n\theta$ with respect to the x-axis. This projection, denoted Q^{θ}, is defined as

$$Q^{\theta} \equiv Q_x \cos(n\theta) + Q_y \sin(n\theta) = \sum_{j=1}^{M} w_j \cos\left(n(\phi_j - \theta)\right)$$

This analysis is performed in practice over equally spaced values of θ, usually $\theta = (k/p)(\pi/n)$ with $k = 0, \ldots, p-1$, and $p = 5$. This gives 5 values of $V_n^{\theta}\{\infty\}$ which are then averaged over θ. This yields final estimates for integral and differential flow with smaller error bars than the individual $V_n^{\theta}\{\infty\}$.

Reference Flow

The reference flow is the average value of the flow vector projected onto the unit vector with angle $n\Phi_R$,

$$V_n \equiv \langle Q_x \cos(n\Phi_R) + Q_y \sin(n\Phi_R)\rangle = \langle Q^{\Phi_R}\rangle.$$

To estimate V_n in the experimental data where Φ_R is unknown, a generating function is defined below, which depends on an arbitrary complex z:

$$G^\theta(z) \equiv \left\langle e^{zQ^\theta} \right\rangle,$$

where the angle brackets represent an average over many events with similar centrality. To calculate the integral flow, we need to evaluate $G^\theta(z)$ for many values on the upper half of the imaginary axis, and then plot the modulus $|G^\theta(ir)|$ as a function of r. An example of such histogram is shown in Fig. 2.10. The value of reference flow is directly related to r_0^θ, the first minimum of $|G^\theta(ir)|$. The reference flow is defined as

$$V_n^\theta\{\infty\} \equiv \frac{j_{01}}{r_0^\theta},$$

where $j_{01} \approx 2.405$ is the first root of the Bessel function $J_0(x)$. As this minimum typically has a large second derivative, it is easier to determine the minimum from the square modulus $|G^\theta(ir)|^2$. The final estimate is then computed as

$$V_n\{\infty\} \equiv \frac{1}{p}\sum_{k=0}^{p-1} V_n^{k\pi/pn}\{\infty\}$$

the value of p is 5 by default. The ∞ symbol is used to indicate that the result is the large order behavior of the cumulant method.

Differential Flow

Once the reference flow $V_n\{\infty\}$ is determined for the Fourier harmonic n, one can determine the differential flow in any harmonic that is an integer multiple of n. This differential flow is denoted as $v'_{mn}\{\infty\}$ and defined by

$$\frac{v'^\theta_{mn}\{\infty\}}{V_n^\theta\{\infty\}} = \frac{J_1(j_{01})}{J_m(j_{01})} Re\left(\frac{\langle \cos[mn(\phi-\theta)] e^{ir_0^\theta Q^\theta}\rangle}{i^{m-1}\langle Q^\theta e^{ir_0^\theta Q^\theta}\rangle}\right) \tag{2.59}$$

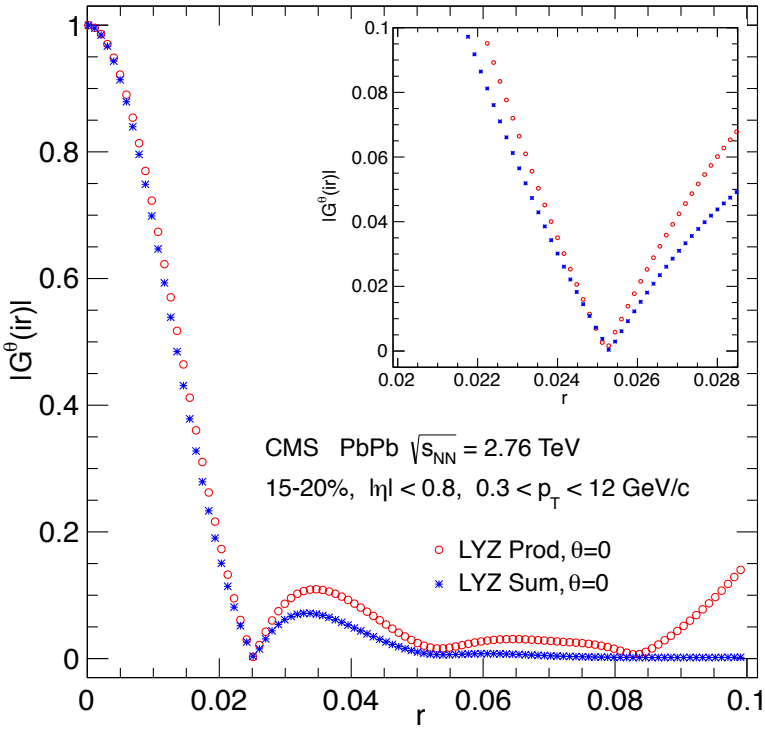

Figure 2.10: An example of modules of the second harmonic Lee-Yang Zero generating functions as a function of the imaginary axis coordinate r for θ=0. Both Sum and Product generating function are shown. It is from 500k real data in $15-20\%$ with $|\eta|<0.8$ and $0.3<p_T<12.0$ Inserted is a zoom of $|G^0(ir)|$ to show the first minimum.

Here ϕ is the azimuthal angle of a particle in the small differential bin, and the angle brackets in the numerator represent an average over all particles in all events. The angle brackets in the denominator is an average over all events.

Alternatively, the differential flow can be obtained by the product generating function Eq. (2.58) by

$$v'^{\theta}_{mn}\{\infty\} = V^{\theta}_{n}\{\infty\}\frac{J_1(j_{01})}{J_m(j_{01})}\mathbf{Re}\left(\frac{\langle G^{\theta}_{n}(ir^{\theta}_{0})\frac{\cos(mn(\phi_j-\theta))}{1+ir^{\theta}_{0}w_j\cos(n(\phi_j-\theta))}\rangle}{i^{m-1}\langle G^{\theta}_{n}(ir^{\theta}_{0})\sum_j\frac{w_j\cos(n(\phi_j-\theta))}{1+ir^{\theta}_{0}w_j\cos(n(\phi_j-\theta))}\rangle}\right) \tag{2.60}$$

where again the average in the numerator is over the particles of interest (differential particles) and the average in the denominator denote over all events.

2.3 Effect of Flow Fluctuation on Different Methods

One of the most important sources of flow fluctuation is the fluctuation of the positions of participant nucleons, which leads to the fluctuation of initial state coordinate space anisotropy, eccentricity, and the fluctuation of v_2. The magnitude of flow fluctuations is defined as [109, 123, 124]:

$$\sigma^2 \equiv \langle v_2^2\rangle - \langle v\rangle^2, \tag{2.61}$$

where v_2 is the flow in the participant plane. Different flow methods involve various functions of v_2. From Section 2.2.3, the flow from two-particle and four-particle correlations can be written as:

$$v_2\{2\}^2 = \langle v_2^2\rangle \tag{2.62}$$

and

$$v_2\{4\}^2 = \left(2\langle v_2^2\rangle^2 - \langle v_2^4\rangle\right)^{1/2} \tag{2.63}$$

For any function of v_2, $f(v_2)$, we can obtain its average value of $\langle f(v_2)\rangle$ by expanding $f(v_2)$ around $\langle v_2\rangle$ to the leading order in σ^2:

$$f(v_2) = f(\langle v_2\rangle) + f'(\langle v_2\rangle)(v_2-\langle v_2\rangle) + \frac{(v_2-\langle v_2\rangle)^2}{2}f''(\langle v_2\rangle) \tag{2.64}$$

taking the average in both sides:

$$\begin{aligned}\langle f(v_2)\rangle &= f(\langle v_2\rangle) + f'(\langle v_2\rangle)(\langle v_2\rangle - \langle v_2\rangle) + \frac{\langle v_2^2\rangle - 2\langle v_2\rangle\langle v_2\rangle + \langle v_2\rangle^2}{2} f''(\langle v_2\rangle) \\ &= f(\langle v_2\rangle) + \frac{\langle v_2^2\rangle - \langle v_2\rangle^2}{2} f''(\langle v_2\rangle) \\ &= f(\langle v_2\rangle) + \frac{\sigma^2}{2} f''(\langle v_2\rangle).\end{aligned} \tag{2.65}$$

Applying Equation 2.65 to Equation 2.62 and 2.63, we find:

$$v_2\{2\}^2 = \langle v_2\rangle^2 + \sigma^2 \tag{2.66}$$

and

$$v_2\{4\}^2 \approx \langle v_2\rangle^2 - \sigma^2. \tag{2.67}$$

The results show that fluctuations increase $v_2\{2\}$ and decrease $v_2\{4\}$. The effect of flow fluctuations to six-particle correlations is similar [110, 125]:

$$v_2\{6\}^2 \approx \langle v_2\rangle^2 - \sigma^2 \tag{2.68}$$

It was found that the Lee-Yang Zeros method is also affected by flow fluctuations in a similar way as in four-particle correlations [126] .

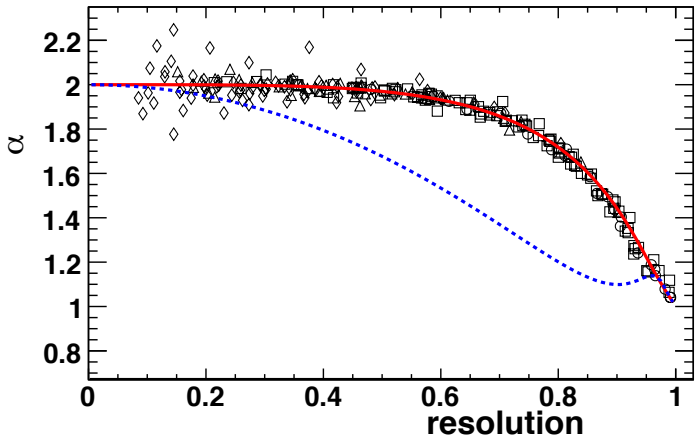

Figure 2.11: The coefficient α in Equation 2.69 as a function of the event plane resolution [109, 124]

For the event plane method, the effect depends on the event plane resolution as [109, 124] :

$$v_2\{EP\}^2 = \langle v_2 \rangle^2 + (\alpha - 1)\sigma^2 \tag{2.69}$$

where α is related to the event plane resolution as shown in Figure 2.11. When the event plane resolution is perfect and equal to 1, the event plane is the same as participant plane, and α =1, which means from Equation 2.69:

$$v_2\{EP, \alpha = 1\}^2 = \langle v_2 \rangle^2 \equiv \langle v_2\{\Psi_2\} \rangle^2 . \tag{2.70}$$

When the event plane resolution is very small, α =2, and from Equation 2.69,

$$v_2\{EP, \alpha = 2\}^2 = \langle v_2 \rangle^2 + \sigma^2 \tag{2.71}$$

which is exactly the same as $v_2\{2\}^2$.

In conclusion, the effect of flow fluctuations on the flow analysis methods can be summarized in one equation as:

$$v_2\{\}^2 = \langle v_2 \rangle^2 + (\alpha - 1)\sigma^2. \tag{2.72}$$

with $\alpha = 0$ for four-, six- and all-particle correlations (LYZ), $\alpha = 2$ for two-particle correlations, and α is in the range from 2 to 1 as the resolution becomes better for the event plane method. We can see that the effects of non-flow and flow fluctuations are different for different methods, which is why so many methods are introduced in this Chapter to study flow. With the measurements of flow from different methods, we can obtain a full picture of the flow, which will provide better constraints for estimating the QGP transport coefficients as will be discussed in the next Section.

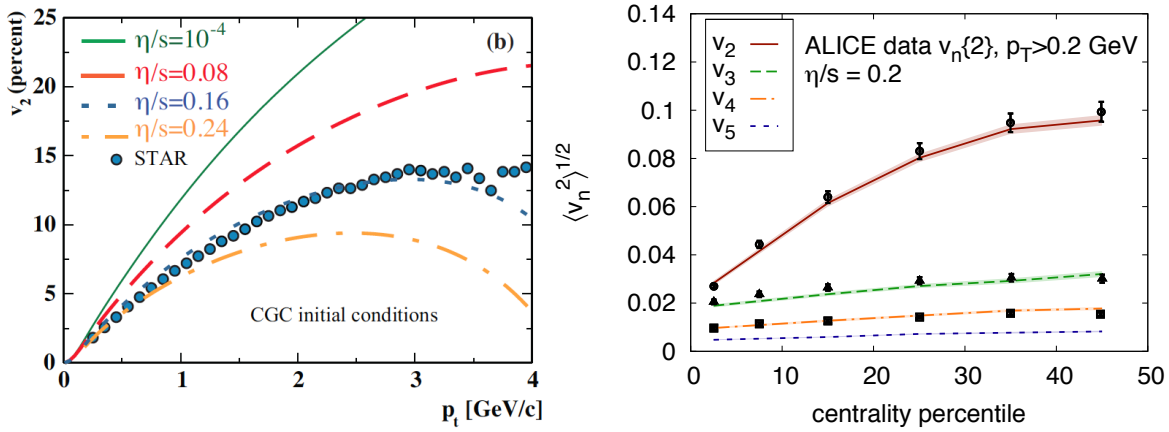

Figure 2.12: Left: The p_T dependence of measured v_2 compared to viscous hydrodynamic model calculations with different η/s [127]. Right: Root-mean-square of v_n from hydrodynamics calculations compared with $v_n\{2\}$ from experiment data as a function of centrality [128].

2.4 QGP Transport Coefficients Estimated from Flow Results

As we discussed in Chapter 1, the large elliptic flow found at RHIC suggests the created medium behaves like an almost perfect liquid. To study how perfect the medium is, the viscous corrections need to be included in hydrodynamics. The shear viscosity η and bulk viscosity ζ are two of the most important transport coefficients under investigation. These transport coefficients are input parameters for viscous hydrodynamics. The basic idea is to change these input parameters, calculate v_2 and compare with real data to see which values of η and ζ are better. The shear viscosity η has been studied a lot by studying the specific shear viscosity, η/s, the ratio of shear viscosity to entropy density.

Figure 2.12 (left) shows the p_T dependence of measured v_2 compared to viscous hydrodynamic model calculations with different η/s [127]. The initial condition model is from CGC which can provide eccentricity calculation. The calculation with $\eta/s = 0.16$ agrees best with the experimental data. The right hand side of Figure 2.12 is the root-mean-square of v_n from hydrodynamics calculations compared with $v_n\{2\}$ from experiment data as a function of centrality [128]. The model used for the calculation of ϵ_n is the IP-Glasma, which is a model within the CGC framework by combining the impact parameter dependent saturation model with the classical Yang-Mills description of initial Glasma fields [129]. The input η/s is 0.2 for these calculations.

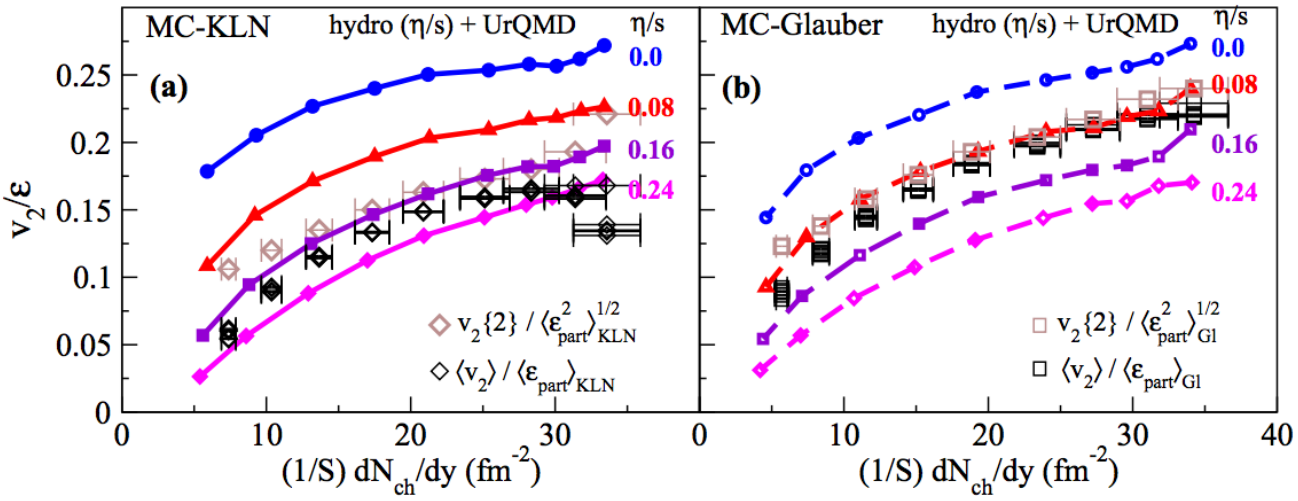

Figure 2.13: Centrality dependence of eccentricity scaled elliptic flow with different η/s and different initial condition models compared with real data (open symbols) [130].

The v_2/ϵ_2 as a function of particle density from data and hydrodynamic calculations are shown in Figure 2.13. The open markers are from real data results. The MC-KLN [131] model, which is an initial condition model based on CGC, agrees with real data better for $\eta/s = 0.16$. However, $\eta/s = 0.08$ is better with the MC-Glauber initial condition model. Figure 2.14 shows the chi-squared per degree of freedom from a fit of experimental flow data as a function of η/s with different initial condition models. The range of η/s from these fit curves gives an indication of the uncertainty in the extraction of η/s due to the uncertainty from initial conditions.

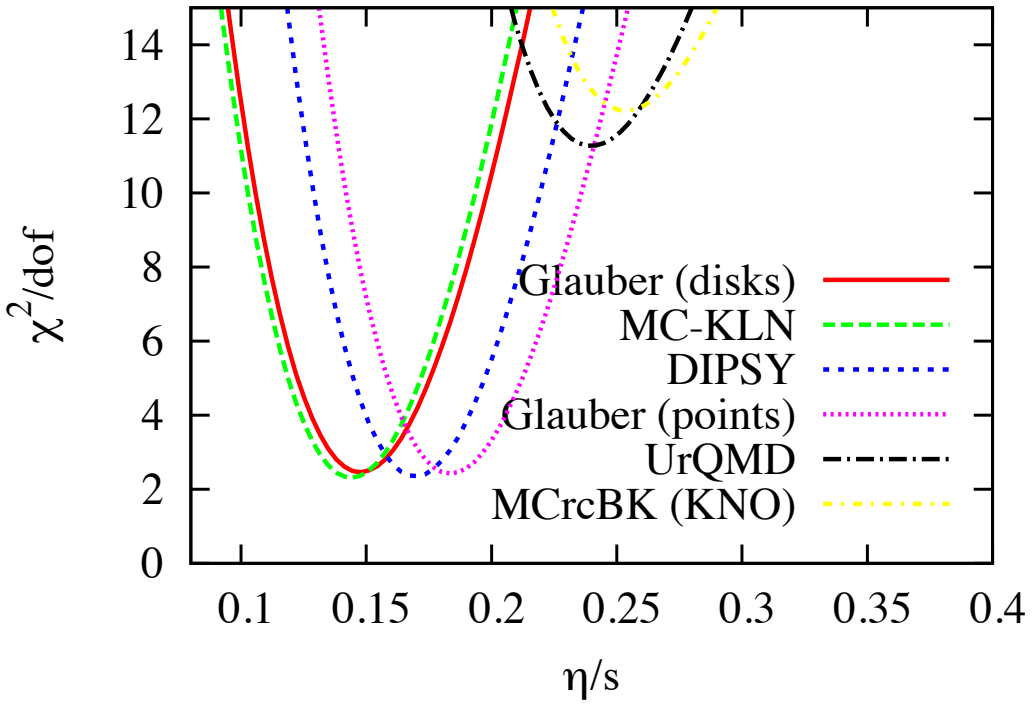

Figure 2.14: Example plot of chi-squared per degree of freedom from a fit of experimental flow data as a function of η/s with eccentricity from different initial condition models [132].

Other methods for estimating η/s have also been investigated. Some recent reviews show that the η/s should be less than 0.4, with a preferred range of $0.08 < \eta/s < 0.24$ [40, 90].

The bulk viscosity can not be ignored from some recent studies [90, 133]. Overall, although big progress has been made for estimating these QGP transport coefficients, it is important to know that there are still large uncertainties from the different initial conditions, from the relative contributions of flow from hadronic and partonic phases, and from the temperature dependence of η/s.

Chapter 3

The LHC and CMS Detector

The particle accelerating and detecting systems are briefly discussed in this chapter. The proton and heavy-ion beams can be accelerated to very high energy at the LHC and collided at designed interaction points. The CMS detector is located at one of these points. We will discuss the CMS detector system, trigger system and its data taking.

3.1 The Large Hadron Collider

The LHC [134–137] is the largest and most powerful collider so far. The purpose of the LHC is to try to answer some of the fundamental open questions in physics. Issues possibly to be studied by the LHC include:

- Is it true that the Higgs mechanism generates the masses of the elementary particles via electroweak symmetry breaking? It has been announced on July 4th, 2012 that a new boson with mass around 125 GeV, "consistent with" the theorized Higgs boson (or a candidate boson) [138, 139], has been observed. Since then, CMS has produced a comprehensive set of production and decay measurements that are published in more than 20 papers. The latest comparisons of the decay rate of the new boson in different channels to the predictions of the standard model of particle physics show no significant deviations from that expected for the standard model Higgs boson [140].
- Is it true that all known particles have supersymmetric partners?
- Are there extra dimensions in addition to the ordinary 4 (3 spatial and one time dimension) as predicted by string theory?
- What is the nature of the dark matter and dark energy?
- Why are there apparent violations of the symmetry between matter and antimatter?
- What are the properties of the Quark-Gluon Plasma? This is related to heavy ion collisions and is the purpose of the thesis.

3.1.1 Design and Layout of LHC

The Large Hadron Collider is a two-ring-superconducting-hadron accelerator and a collider. It is installed in a tunnel of 26.7 km in circumference, lying between 45 and 170 m below the ground crossing the border from Switzerland to France near Geneva, Switzerland. A series of pre-accelerators are utilized before the beam is injected into the LHC. The left hand side of Figure 3.1 shows the LHC injector. Protons are obtained by stripping electrons from hydrogen atoms and are accelerated

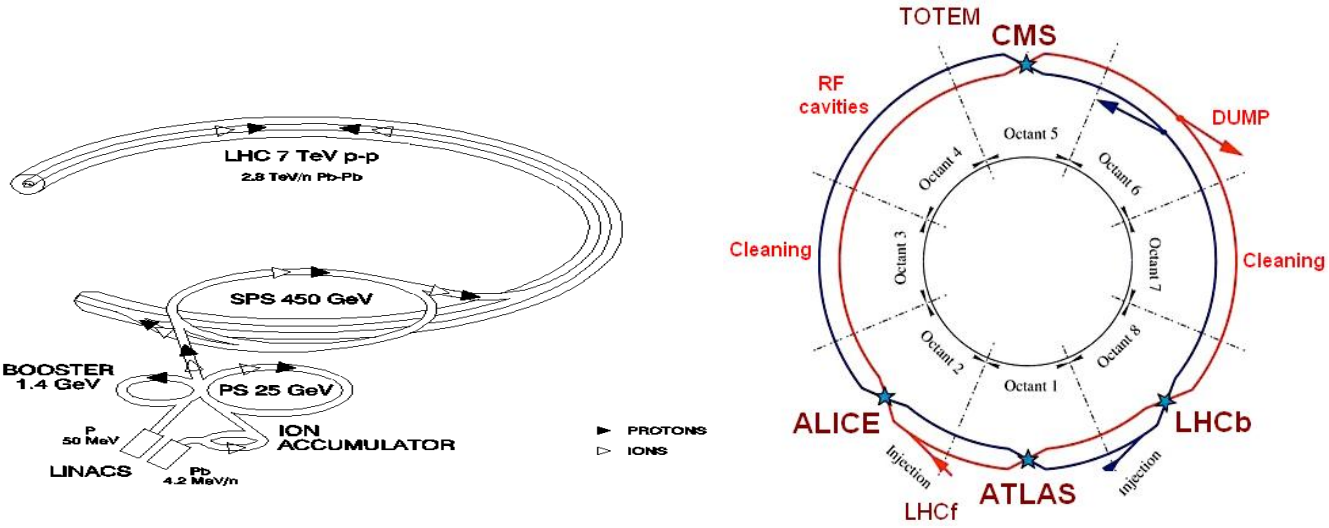

Figure 3.1: Schematic layout of the LHC injector and the LHC ring

to 50 MeV in the linear particle accelerator (LINAC 2). They then enter the Proton Synchrotron Booster (PSB) and are accelerated to 1.4 GeV. On the next stage, the protons are injected into Proton Synchrotron (PS), accelerated to 25 GeV and sent to the Super Proton Synchrotron (SPS), where their energy is increased to 450 GeV. Finally, they are injected into the LHC, both in a clockwise and an anti-clockwise direction, and accelerated to the collision energy.

Lead ions can also be accelerated in the system. A highly purified lead sample is heated to a temperature of about $500°C$ to produce the lead ions. An electron current is used to ionize the lead vapor. Many different charged states are produced in this stage, with a maximum of around Pb^{29+}. These ions are then accelerated to 4.2 MeV per nucleon in the linear accelerator 3 (LINAC 3) and passed through a carbon foil, where most of the electrons are stripped to produce Pb^{54+} ions. The beam is then accelerated to 72 MeV per nucleon in the Low Energy Ion Ring (LEIR), and sent to the PS, which increases the energy to 5.9 GeV per nucleon. After passing through a second foil that fully strips the lead ions to Pb^{82+}, the beam is send to the SPS and accelerated to 177 GeV per nucleon. Finally, it is sent to the LHC in both directions and accelerated to the collision energy. It is designed that the LHC can also collide protons and lead ions, so we can have pp, pPb, and PbPb collisions.

In order to keep the beams on their circular path and focus the beams, 1232 dipole magnets and 392 quadrupole magnets are used at the LHC. Superconducting magnets are used so that the strongest magnetic field can be created with minimum energy consumption. Of course, the system needs to be cooled down to very low temperature to maintain superconductivity. About 96 tonnes of liquid helium 4 is needed to keep the magnets at their operating temperature of 1.9 K or $-271.25°C$.

The LHC is designed to collide the proton-proton beams at a center-of-mass energy of 14 TeV with a nominal luminosity of $\mathcal{L} = 10^{34}\,\mathrm{cm}^{-2}\mathrm{s}^{-1}$ and the Pb-Pb beams at a center-of-mass energy of 5.5 TeV per nucleon pair with a peak luminosity of $\mathcal{L} = 10^{27}\,\mathrm{cm}^{-2}\mathrm{s}^{-1}$. In order to have high luminosity so that more events can be analyzed, we need to have as many bunches of protons (or lead ions) as possible in both rings, and in each bunch, as many protons (or lead ions) as possible. In the peak

luminosity, the number of effective proton (Pb) bunches is 2808 (592). In principle, there can be as many as 3564 (891) proton (lead) bunches, but not every bunch is filled in practice. This makes the minimum bunch spacing about 26.7km/3564 = 7.5m, or in the unit of time, 7.5m/(speed of beam) $\approx 7.5/(3 \times 10^8)$ s ≈ 25 ns for proton beams, and for Pb beams, about 26.7km/891 = 30m, or 30m/(speed of beam) $\approx 30/(3 \times 10^8)$ s ≈ 100 ns in the unit of time [141]. There will be about 10^{11} (7×10^7) protons (Pb ions) in each bunch. The protons (Pb ions) are grouped in cylindrical bunches with a radius of 16.6 (15.9) μm and a length of 7.55 (7.94) cm.

3.1.2 Experiments at the LHC

As shows in Figure 3.1 (right), there are eight arcs and four beam-crossing points at the LHC. Four detectors are constructed at the four collision points. They are: A Toroidal LHC Apparatus (ATLAS), A Large Ion Collider Experiment (ALICE), Compact Muon Solenoid (CMS), and The Large Hadron Collider beauty experiment (LHCb). Three other detectors share the same collision points with ATLAS, CMS and ALICE. There are altogether seven detectors that operate at the LHC

1. CMS [142] and ATLAS [143] are two general-purpose detectors that are built to study pp, pPb, and PbPb collisions. The focus of the two experiments are the verification of the standard model, search for the Higgs boson, physics beyond the standard model, and heavy ion physics. The two detectors are optimized for high-p_T physics to enhance the discovery potential of new heavy particles postulated by various models, such as the supersymmetric extensions (SUSY) of the standard model, and the use of the di-lepton and high-p_T probes in the study of the quark-gluon plasma. The large charged particle pseudorapidity coverage in the two detectors is also advantageous for particle correlation studies, as performed in this thesis.

2. ALICE [144] is a dedicated heavy-ion detector, which is optimized to study heavy ion collisions. The strengths of the detector are particle identification and low-p_T observables.

3. LHCb [145] studies the CP-violation in the b-quark systems produced in the proton-proton collisions.

4. TOTEM (TOTal Elastic and diffractive cross section Measurement) [146] is designed for the measurement of total cross section, elastic scattering and diffractive processes in the p+p collisions. It shares the same interaction point with the CMS detector.

5. LHCf (Large Hadron Collider forward) [147] is a special-purpose detector to study the particles generated in the "forward" region of collisions, those almost directly in line with the beams. It shares the same interaction point with the ATLAS experiment and consists of two detectors, situated at a distance 140 m on either side of the interaction point. The LHCf is designed to measure the energy and number of π^0 mesons produced in high-energy pp collisions, which will help explain the origin of high energy cosmic rays.

6. MoEDAL (Monopole and Exotics Detector At the LHC) [148] was approved in May 2010. The aim of this new detector is to directly search for Magnetic Monopole (MM) and other highly ionizing Stable Massive Particles at the LHC.

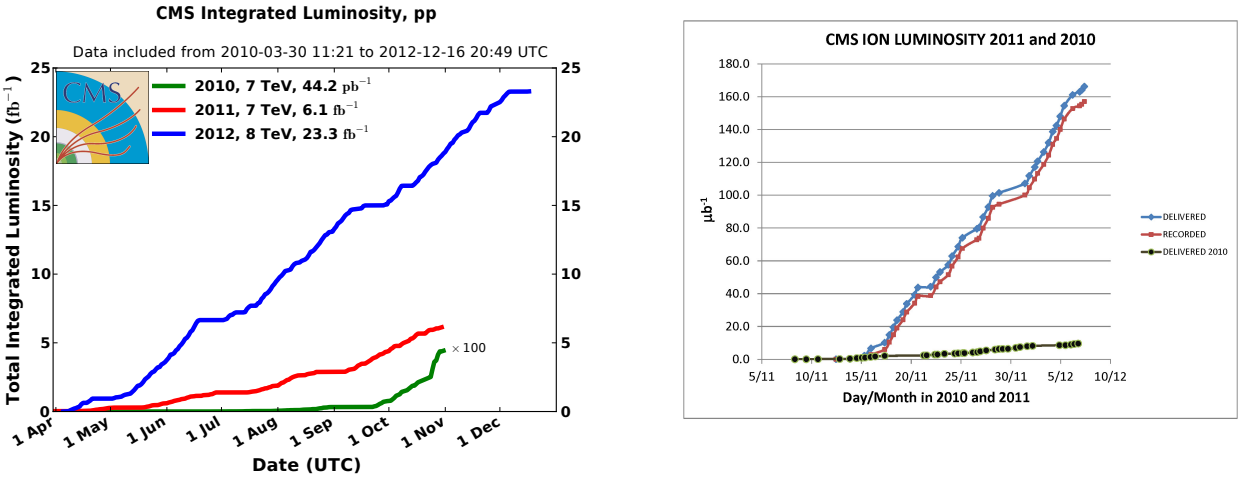

Figure 3.2: The CMS integrated luminosity for pp collisions [149] (left) and PbPb collisions [150] (right) .

Starting in November of 2009, the LHC had the first pp collisions at center-of-mass energies of 0.9 and 2.36 TeV, already becoming the world's highest-energy particle accelerator. The energy was increased to 7 TeV in 2010 and to 8 TeV in 2012. The left hand side plot of Figure 3.2 shows the integrated luminosity as a function of time for pp collisions from 2010 to the end of 2012. The right hand side plot of Figure 3.2 is the integrated luminosity for PbPb collisions in 2010 and 2011. The first full year of operation in 2010 delivered about 44 pb^{-1} of pp data to the CMS detector at $\sqrt{s} = 7$ TeV. The first PbPb run delivered over 7 μb^{-1} to the CMS detector at $\sqrt{s_{NN}} = 2.76$ TeV (the energy per nucleon is 1.38 TeV, from $E = \gamma m_0 c^2$, we have $\gamma = \frac{1}{\sqrt{1-v^2/c^2}} = \frac{E}{m_0 c^2} \approx 1380/0.938$, we get the speed of the Pb nucleus is $v \approx \sqrt{1-(0.938/1380)^2} \cdot$ c $\approx 0.99999977 \cdot$c). The pp data was also collected at 2.76 TeV to provide reference measurements for the PbPb collisions that were collected at the same center-of-mass energy. The 2011 run delivered 6.13 fb^{-1} of pp collisions at $\sqrt{s} = 7$ TeV, and for PbPb at $\sqrt{s_{NN}} = 2.76$ TeV with an integrated luminosity of about 166.7 μb^{-1} (the estimated total number of PbPb collisions: $\text{N} = \mathcal{L}_{int} \times \sigma^{inel}_{PbPb} = 166.7\ \mu\text{b}^{-1} \times 7.65\text{b} = 1.275$ billion events). The pp run in 2012 was very successful with 23.30 fb^{-1} delivered at $\sqrt{s} = 8$ TeV. A short pilot run of pPb collision at $\sqrt{s_{NN}} = 5.02$ TeV was delivered in September 2012. In January and February of 2013, 34.7 nb^{-1} of pPb collisions at $\sqrt{s_{NN}} = 5.02$ TeV was delivered to CMS. The results in the thesis use the 7 μb^{-1} PbPb data from 2010, 166.7 μb^{-1} PbPb data from 2011, and 31.69 nb^{-1} pPb data from 2013.

3.2 The Compact Muon Solenoid Detector

CMS is a general-purpose detector, which provides the opportunity to study both pp and heavy ion collisions. A detailed description of the CMS experiment can be found in [142]. The main distinguishing features of CMS are a strong field solenoid, a full silicon-based inner tracker, and a homogeneous scintillating-crystals-based electromagnetic calorimeter. The CMS coordinate system

has the origin centered at the nominal collision point, the y-axis pointing vertically upward, and the x-axis pointing inward toward the center of the LHC ring. Thus, the z-axis is pointing counter-clockwise in the beam direction. The azimuthal angle ϕ is measured from the x-axis in the x-y plane and the radial coordinate in this plane is denoted by r. The polar angle θ is measured from the z-axis. Pseudorapidity is defined as $\eta = -ln\tan(\theta/2)$. The transverse momentum and transverse energy, denoted by p_T and E_T, are computed from the x and y components.

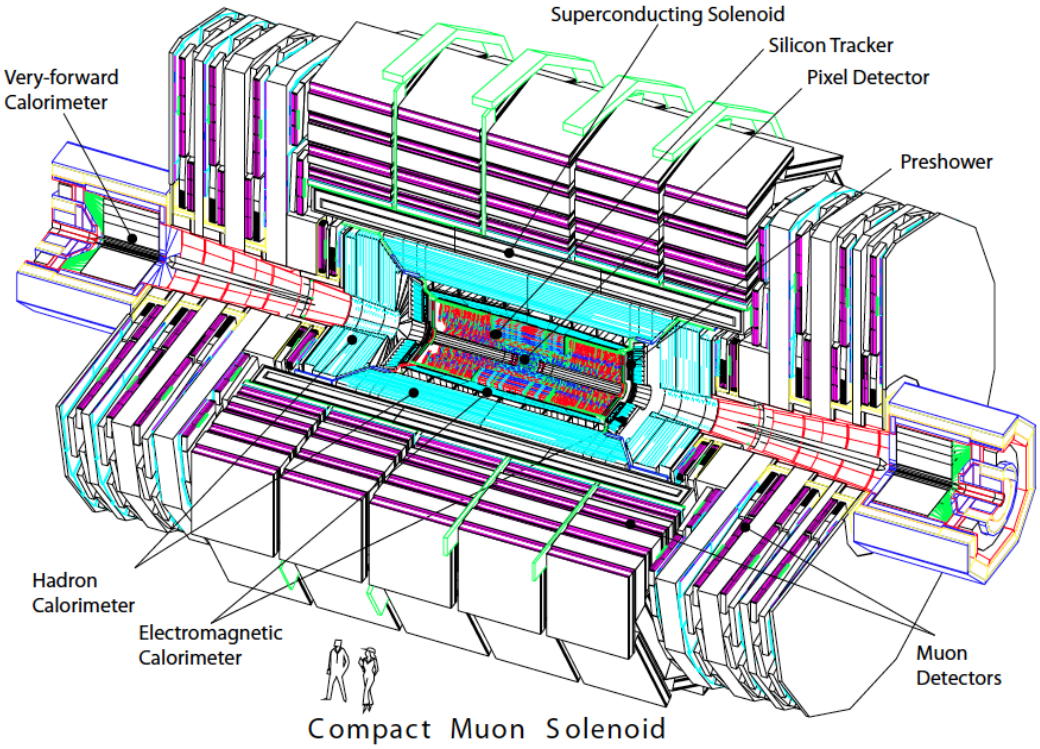

Figure 3.3: A perspective view of the CMS detector.

The overall layout of CMS is shown is Figure 3.3. The detector is 21.6 meters long, 15 meters in diameter, and weighs about 14,000 tonnes. Approximately 3,800 people, from 182 scientific institutes in 42 countries, form the CMS collaboration, built and now operate the detector.

The first layer of the detector is the tracker that can track the path of a particle through the magnetic field. The tracker is made entirely of silicon, with the silicon pixels, at the core of the detector and dealing with the highest intensity of particles, and the silicon strip detector that surrounds it. As particles travel through the tracker, the pixels and strips produce small electric signals that are amplified and detected. A detailed description of the tracker is given in Section 3.2.1.

The second layer is the Electromagnetic Calorimeter (ECAL) that is designed to measure the energies of electrons and photons with high accuracy. The ECAL uses lead tungstate ($PbWO_4$) crystals with coverage in pseudorapidity up to $|\eta| < 3.0$ and 4π in azimuth. The scintillation light is detected by silicon avalanche photodiodes (APDs) in the barrel region and vacuum phototriodes (VPTs) in the endcap region. A preshower system made of lead absorber plate is in front of the endcap to measure the energy of showers initiated in the lead plate.

The third layer is the Hadron Calorimeter (HCAL) that can measure the energy of hadrons with a coverage up to $|\eta| < 3.0$ and 4π in azimuth. The HCAL consists of layers of dense material interleaved with tiles of plastic scintillators. The pseudorapidity coverage is $|\eta| < 1.4$ for the barrel region and $1.3 < |\eta| < 3.0$ for the endcap region.

Next, positioned radially outward from the HCAL, is the CMS magnet, which is the central device around which the experiment is built. The designed magnetic field is 4 Tesla, 100,000 times stronger than the magnetic field of the earth. The operating field is scaled down to 3.8 Tesla to maximize its longevity.

The muon system is very important for CMS as the name "Compact Muon Solenoid" suggests. One of the clearest "signatures" of the Higgs Boson is its decay into four muons. To identify and measure the momentum of muons, drift tubes, cathode strip chambers and resistive plate chambers are used in CMS. These sub-detectors are embedded in the steel yoke. The drift tubes are used for the trajectory measurement in the central barrel region, while the cathode strip chambers are used in the endcaps. The resistive plate chambers, installed in both barrel and endcaps, provide a fast signal when a muon passes through the muon system.

The Forward Hadron Calorimeter (HF) consists of a steel absorber structure composed of grooved plates with quartz fibers inserted into these grooves. The HF calorimeters are placed at a distance of 11.2 m from the interaction point, covering the pseudorapidity range of $2.9 < |\eta| < 5.2$. A more detailed description of the HF calorimeters is given in Section 3.2.2.

The Beam Scintillator Counters (BSC) are a series of scintillator tiles that provide hit and coincidence rates, and can be used as a minimum-bias trigger for inelastic events. They are placed along the beam line at a distance of ± 10.9 m from the interaction point for the inner tiles, and ± 14.4 m for the outer tiles. There is a timing difference between the inner and outer tiles, thus allowing events to be tagged as incoming (towards the interaction point, triggered only by beam halo particles) and outgoing (away from the interaction point, that can be triggered from particles created in a collision or from beam halo particles). The BSC functioned during the 2010 and 2011 pp and PbPb runs and were replaced with upgraded Beam Halo Counters (BHC) that could also detect beam halo events and serve as a heavy ion minimum-bias trigger. During the 2013 pPb run, the performance of the BHC was explored, but it was still under commissioning study and not used in the minimum-bias trigger.

The Beam Pick-up Timing for the eXperiments (BPTX) are located around the beam pipe at a distance of ± 175 m from the interaction point. They are designed to provide precise information about the bunch structure and timing of the incoming beam with time resolution better than 0.2 ns.

In the following, the detectors used in this thesis are further described.

3.2.1 The Inner Tracking System

The inner tracking system is designed to provide a precise and efficient measurement of the trajectories of charged particles and a precise reconstruction of secondary vertices produced from the weak decay of short-lived particles. It surrounds the interaction point and has a length of 5.8 m

and a diameter of 2.5 m. At the designed LHC luminosity that is expected to be achieved soon after the restart of the LHC in 2015, there will be about 25 pp collisions on the average in each bunch crossing (pileup of 25) and about 1000 particles will be produced. In comparison, several times more particles can be produced in a single PbPb collision. Therefore, a detector technology featuring high granularity and fast response is required. The intense particle flux will also inevitably cause severe radiation damage to the tracking system. These requirements on granularity, speed and radiation hardness lead to a tracker design entirely based on silicon detector technology.

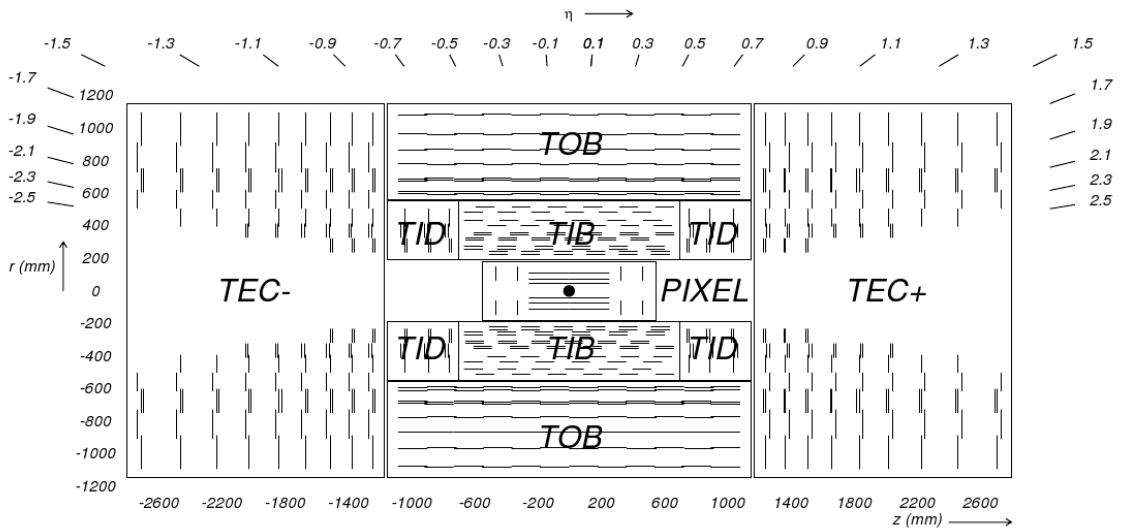

Figure 3.4: Schematic cross section through the CMS tracker [142]. Each short line represents a detector module, with double lines indicating back-to-back modules that deliver stereo hits.

A schematic cross section of the inner tracker system is shown in Figure 3.4. The CMS tracker is composed of a silicon pixel detector with three barrel layers at radii between 4.4 cm and 10.2 cm, and a silicon strip tracker with 10 barrel detection layers extending outwards to a radius of 1.1 m. Each system is completed by endcaps that consist of 2 disks in the silicon pixel detector and 3 plus 9 disks in the strip tracker on each side of the barrel, extending the acceptance of the tracker up to a pseudorapidity of $|\eta|$ <2.5. As shown in Figure 3.4, the 10 barrel layers are the Tracker Inner Barrel (TIB) and Tracker Outer Barrel (TOB). In the endcaps, there are 3 small layers of Tracker Inner Disc (TID) and 9 larger disc layers called the Tracker Endcap (TEC)

The Silicon Pixel Detector System

The pixel system is the part of the tracking system that is closest to the interaction region. It contributes precise tracking points in $r - \phi$ and z, thus it is important for good secondary vertex reconstruction and forming seed tracks for the outer track reconstruction. The layout of the silicon pixel detector system is shown in Fig. 3.5. The three 53 cm long barrel layers are at a mean radii of 4.4, 7.3, and 10.2 cm from the nominal interaction point, and the endcap layers are at $z = \pm 34.5$ cm and $z = \pm 46.5$ cm at a distance of 6–15 cm in radius from the beam axis. The barrel (endcap) layers contain 48 (18) million pixels covering a total area of 0.78 (0.28) m^2, with a pixel cell size of

$100 \times 150\,\mu\text{m}^2$. The arrangement gives complete azimuthal coverage over the pseudorapidity range of $|\eta| < 2.5$.

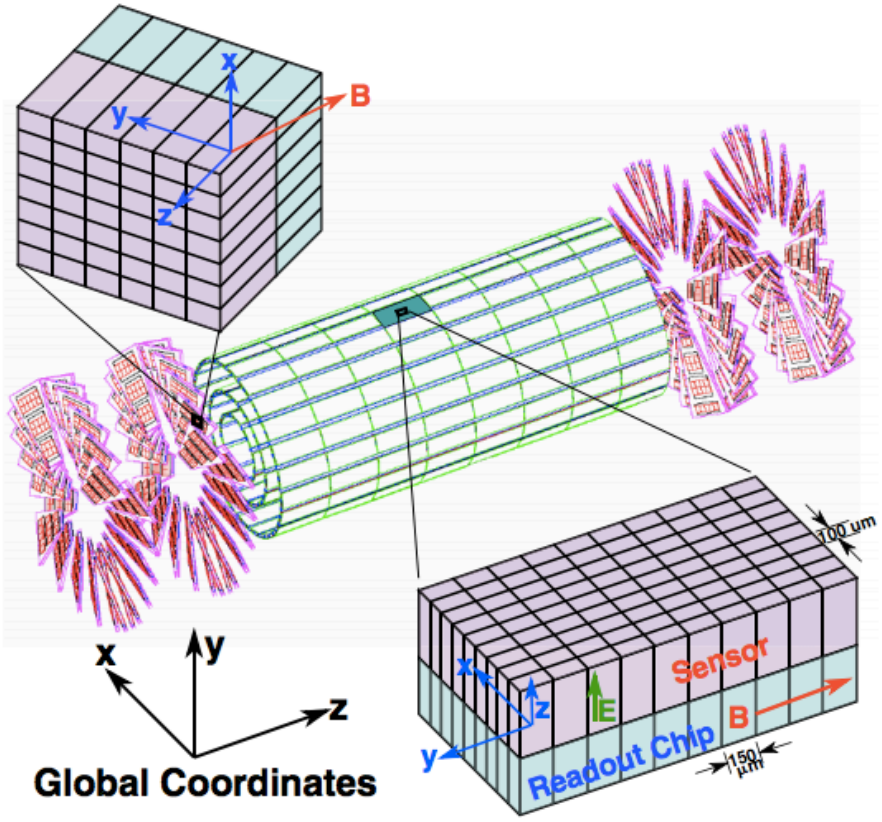

Figure 3.5: The layout of the CMS pixel detector, with example cartoons showing individual modules and their local coordinate systems [151].

The Silicon Strip Tracker

The Tracker Inner Barrel (TIB) consists of four concentric cylinders placed at radii of 255.0 mm, 339.0 mm, 418.5 mm, and 498.0 mm respectively from the beam axis that extend from -700 mm to +700 mm along the z axis. The TID are assemblies of three disks placed in z between ±800 mm and ±900 mm. The disks are identical and each one consists of three rings which span the radius from roughly 200 mm to 500 mm. The TOB consists of six layers with average radii of 608, 692, 780, 868, 965, 1080 mm. The TEC extend radially from 220 mm to 1135 mm and from ±1240 mm to ±2800 mm along the z-direction. Each endcap consists of nine disks that carry substructures on which the individual detector modules are mounted. The design of TIB and TID, as well as TOB and TEC, together guarantee a pseudorapidity coverage of $|\eta| < 2.5$.

3.2.2 The Forward Hadron Calorimeter

The Forward Hadron Calorimeter (HF) is of particular importance to heavy ion physics analysis. It is useful for event selections, and more importantly, the measured energy from HF can be used to estimate the event centrality. Signals from HF can also be used to monitor the real time luminosity during the runs.

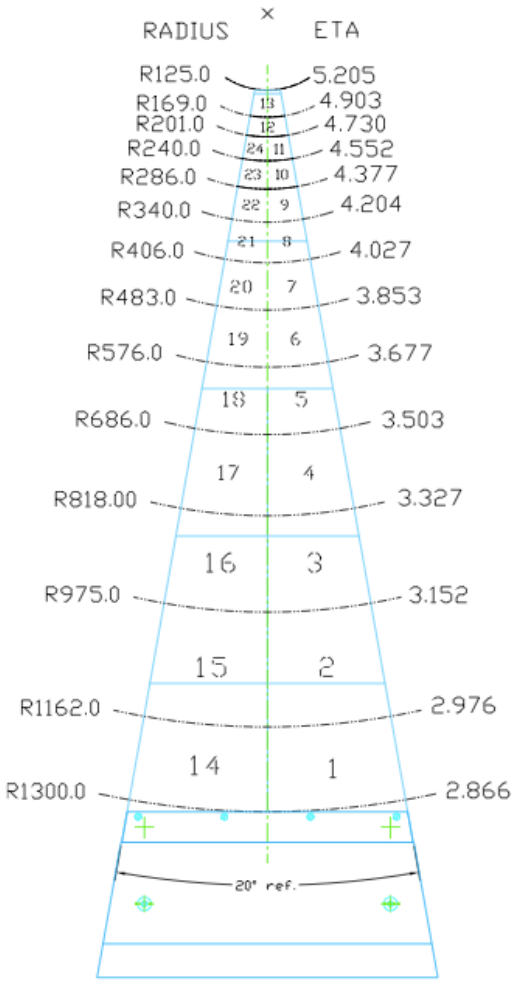

Figure 3.6: Transverse segmentation of the HF towers on a single 20° modular wedge of the HF detector. The radius and pseudorapidity coverage of each segment are displayed [142].

The HF is comprised of 5 mm thick grooved steel absorber plates, with grooves that are approximately 1 mm wide and deep. Quartz fibers (fused silica core and polymer hard-cladding) are inserted into these grooves. Along with the cladding, the diameter of the fibers is $800 \pm 30\mu$m, and over 1000 km of total fiber length was used to construct the HF. A signal is generated in the quartz fibers when charged particles with an energy above the Cherenkov threshold (≥ 190 keV for electrons) generate Cherenkov light, which is guided to photomultipliers stationed behind a shielding matrix. Half of the quartz fibers run over the full depth of the detector (165 cm), while the other half begin 22 cm from the front of the detector. The fibers are bundled into 0.175×0.15

($\Delta\eta \times \Delta\phi$) towers. The HF forms a hollow cylinder with an inner radius of 12.5 cm from the center of the beam line, and an outer radius of 130.0 cm. The front face of the HF is 11.2 m from the nominal interaction point. The HF consists of 18 modular wedges covering 20° each at both positive and negative pseudorapidity. As an example, one modular wedge of the HF segmentation in the transverse plane is shown in Figure 3.6.

Chapter 4

Experimental Method

4.1 Event Selections

4.1.1 Selections in PbPb Collisions

The PbPb minimum-bias event sample is collected using coincidences between the trigger signals from both the $+z$ and $-z$ sides of either the BSC or HF. The minimum-bias trigger used for the analysis is required to be in coincidence with the presence of both colliding ion bunches in the interaction region. This requirement suppresses noncollision-related noise, cosmic rays, and beam backgrounds (beam halo and beam-gas collisions). In the 2010 data sample, the total hadronic collision rate varied between 1 and 210 Hz, depending on the number of colliding bunches and the bunch intensity.

In order to obtain a pure sample of inelastic hadronic collisions, several offline selections are applied to the triggered event sample. These selections remove contamination from noncollision beam backgrounds and from ultra peripheral collisions (UPC) that lead to an electromagnetic breakup of one or both of the Pb nuclei [152]. First, beam-halo events are vetoed based on the BSC timing. Then, to remove UPC and beam-gas events, an offline HF coincidence of at least three towers on each side of the interaction point is required, with a total deposited energy of at least 3 GeV in each tower. A reconstructed primary vertex made of at least two tracks and consistent with the nominal interaction point position is required. To further reject beam-gas and beam-halo events, the pixel clusters are required to have a length along the beam direction compatible with being produced by particles originating from the primary vertex, as for the study in [153]. Additionally, a small number of noisy events with uncharacteristic hadron calorimeter responses are removed.

The acceptance of the silicon tracker for $|\eta| > 0.8$ is found to vary significantly with respect to the longitudinal position of the collision point relative to the geometric center of the detector. This event-by-event variance in the tracking efficiency contributes to a systematic bias of the elliptic flow measurements at forward pseudorapidity. In order to remove this bias, events in this analysis are required to have a longitudinal vertex position within 10 cm of the geometric center of the detector. After all selections, 22.6 million minimum-bias events, corresponding to an integrated luminosity of approximately $3\,\mu\text{b}^{-1}$, remain in the final 2010 data. A sample of 2.76 TeV PbPb data collected during the 2011 LHC heavy-ion run, corresponding to an integrated luminosity of $2.3\,\mu\text{b}^{-1}$, is also analyzed for comparing with pPb collisions.

4.1.2 Selections in pPb Collisions

The pPb analysis is performed using data recorded by CMS during the LHC pPb run in 2013. The data set corresponds to an integrated luminosity of about 31 nb^{-1}, assuming a pPb interaction cross section of 2.1 barns. The beam energies were 4 TeV for protons and 1.58 TeV per nucleon for lead nuclei, resulting in a center-of-mass energy per nucleon pair of 5.02 TeV. The direction of the higher energy proton beam was initially set up to be clockwise, and was then reversed. As a result of the energy difference between the colliding beams, the nucleon-nucleon center-of-mass in the pPb collisions is not at rest with respect to the laboratory frame. Massless particles emitted at $\eta_{\text{cm}} = 0$ in the nucleon-nucleon center-of-mass frame will be detected at $\eta = -0.465$ (clockwise proton beam) or 0.465 (counterclockwise proton beam) in the laboratory frame.

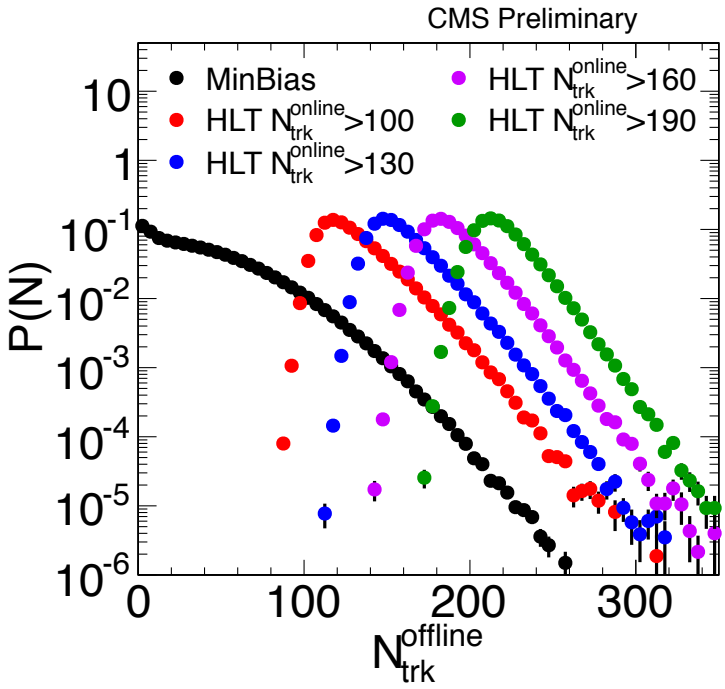

Figure 4.1: The $N_{trk}^{offline}$ distribution for minimum-bias trigger and different high-multiplicity trigger paths.

Minimum-bias pPb events were triggered by requiring at least one track with $p_T > 0.4$ GeV/c to be found in the pixel tracker for a pPb bunch crossing. Because of hardware limits on the data acquisition rate, only a small fraction ($\sim 10^{-3}$) of all minimum bias triggered events were recorded (i.e., the trigger was "prescaled"). In order to select high-multiplicity pPb collisions, a dedicated high-multiplicity trigger was implemented using the CMS level-1 (L1) and high-level trigger (HLT) systems. At L1, the total transverse energy summed over ECAL and HCAL was required to be greater than a given threshold (20 or 40 GeV). Online track reconstruction for the HLT was based on the three layers of pixel detectors, and required a track origin within a cylindrical region of length 30 cm along the beam and radius 0.2 cm perpendicular to the beam. For each event, the vertex reconstructed with the highest number of pixel tracks was selected. The number of pixel tracks ($N_{\text{trk}}^{\text{online}}$) with $|\eta| < 2.4$, $p_T > 0.4$ GeV/c, and a distance of closest approach of 0.4 cm or less to this

vertex, was determined for each event. Data were taken with thresholds of $N_{\rm trk}^{\rm online} > 100, 130$ (L1 threshold of 20 GeV), and 160, 190 (L1 threshold of 40 GeV) with prescaling factors dependent on the instantaneous luminosity. The $N_{\rm trk}^{\rm online} > 190$ trigger was never prescaled throughout the entire run. Figure 4.1 shows the $N_{trk}^{offline}$ distribution for minimum-bias trigger and different high-multiplicity trigger paths.

In the offline analysis, hadronic collisions were selected by requiring a coincidence of at least one HF calorimeter tower with more than 3 GeV of total energy in each of the HF detectors. Events were also required to contain at least one reconstructed primary vertex within 15 cm of the nominal interaction point along the beam axis and within 0.15 cm transverse to the beam trajectory. At least two reconstructed tracks were required to be associated with the primary vertex. Beam related background was suppressed by rejecting events for which less than 25% of all reconstructed tracks were of good quality (i.e., the tracks selected for physics analysis as will be discussed later).

The pPb instantaneous luminosity provided by the LHC in the 2013 run resulted in approximately 3% probability of at least one additional interaction occurring in the same bunch crossing, resulting in pileup events. A procedure for rejecting pileup events was developed to select clean, single-vertex pPb collisions. The approach was to investigate the number of tracks, $N_{\rm trk}^{\rm best}$ that is assigned to the best reconstructed vertex (e.g., the one with the greatest number of associated tracks), and $N_{\rm trk}^{\rm add}$ assigned to each of the additional vertices, as well as the distance between the two vertices in the z direction ($\Delta z_{\rm vtx}$). Based on studies using low pileup pPb data (from the 2012 pilot run), PbPb data, and MC simulations, events with $N_{\rm trk}^{\rm add}$ above a certain threshold at a given $\Delta z_{\rm vtx}$ were identified as pileup events and removed from the event sample. This threshold was set to be higher for smaller $\Delta z_{\rm vtx}$ and larger $N_{\rm trk}^{\rm best}$ to account for the fact that events with a smaller vertex separation and greater multiplicity have a higher probability of vertex splitting in the reconstruction algorithm. The residual pileup fraction was estimated to be no more than 0.2% for the highest multiplicity pPb interactions studied in this paper.

Among those pPb interactions simulated with the EPOS [154] and HIJING [155] event generators, which have at least one primary particle with total energy $E > 3\,\text{GeV}$ in both η ranges of $-5 < \eta < -3$ and $3 < \eta < 5$, the above criteria are found to select 97–98% of the events.

4.2 Centrality Determination and Glauber Model Calculation

4.2.1 Centrality Determination

The total transverse energy deposited into the HF detectors at both positive and negative pseudorapidity ($2.9 < |\eta| < 5.2$) is the variable chosen to estimate the centrality of each PbPb event. The distribution of energy per minimum-bias event is shown in Fig. 4.2. This distribution is then used to divide the events into 40 bins, each representing approximately 2.5% of the total inelastic cross section. These bins may be combined to create 5 or 10% centrality classes.

Using Monte Carlo simulations, it is estimated that the minimum-bias trigger and the event selections include $(97 \pm 3)\%$ of the total inelastic cross section. For the events included in this thesis, the trigger is fully efficient.

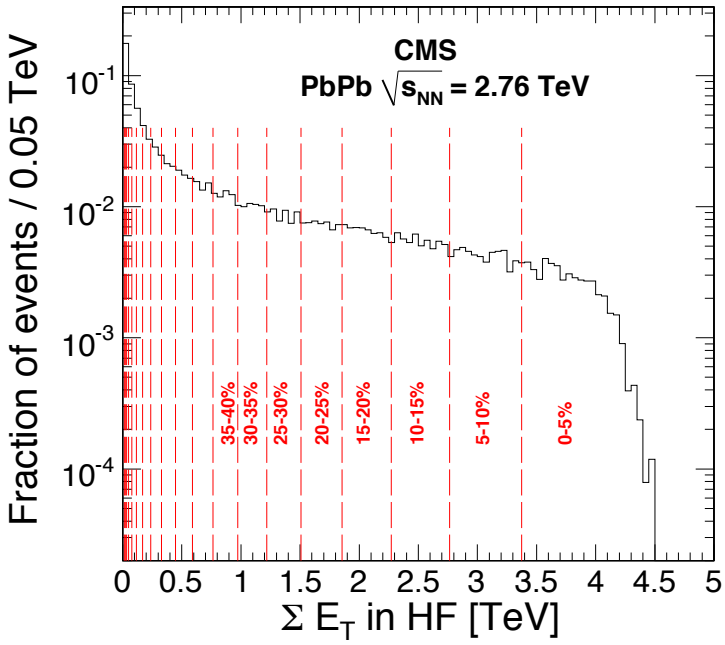

Figure 4.2: The distribution of the total transverse energy in the HF used to determine the centrality of a PbPb collision. The centrality boundaries for each 5% interval are given by the dashed red lines [156].

For pPb collisions, the events were divided into classes of reconstructed track multiplicity, $N_{trk}^{offline}$, where primary tracks with $|\eta| < 2.4$ and $p_T > 0.4$ GeV/c were counted, in a method similar to the approach used in [117,157]. Data from the HLT minimum bias trigger were used for $N_{trk}^{offline} < 120$, while the track multiplicity triggers with online track thresholds of 100, 130, 160, and 190 were used for $120 \leq N_{trk}^{offline} < 150$, $150 \leq N_{trk}^{offline} < 185$, $185 \leq N_{trk}^{offline} < 220$, and $N_{trk}^{offline} \geq 220$, respectively. This correspondence ensures at least 90% trigger efficiency in each multiplicity bin. The fractions of MB triggered events after event selections falling into each of the main multiplicity classes are listed in Table 4.1. The table also lists the average values of $N_{trk}^{offline}$ and $N_{\mathrm{trk}}^{\mathrm{corrected}}$, the event multiplicity of charged particles with $|\eta| < 2.4$ and $p_T > 0.4$ GeV/c corrected for detector acceptance and efficiency of the track reconstruction algorithm.

In order to compare directly the pPb and PbPb systems using event selections based on the multiplicity of the collisions, a subset of data from semi-peripheral PbPb collisions collected during the 2011 LHC heavy-ion run with a minimum bias trigger were reanalyzed using the same track reconstruction algorithm as the one employed for pPb collisions. Figure 4.3 shows the comparison of the $N_{trk}^{offline}$ distributions for minimum bias pPb and 50-100% centrality PbPb collisions. The average $N_{trk}^{offline}$ and $N_{\mathrm{trk}}^{\mathrm{corrected}}$ values, and corresponding average PbPb collision centrality, as determined by the total energy deposited in the HF calorimeters, are listed in Table 4.1 for each $N_{trk}^{offline}$ bin.

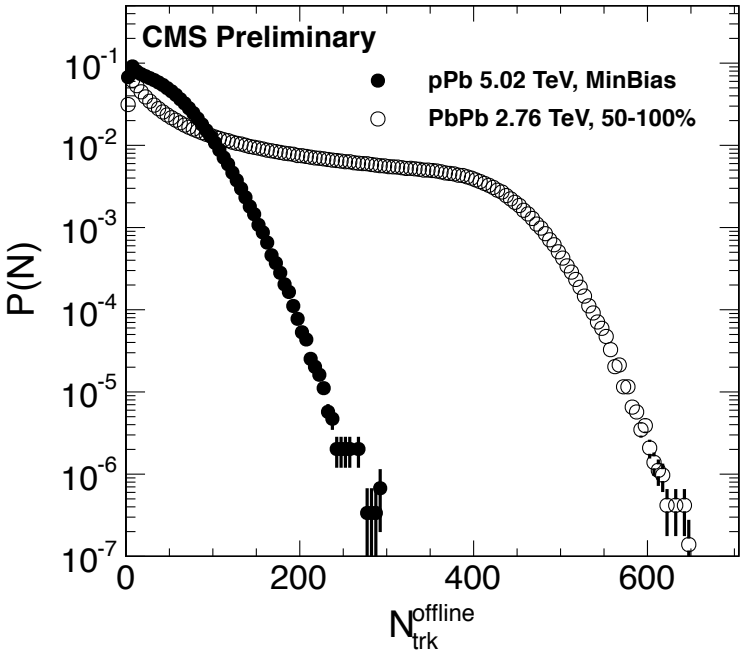

Figure 4.3: The $N_{trk}^{offline}$ distributions for minimum bias pPb and 50-100% centrality PbPb collisions.

4.2.2 Glauber Model Calculation

The Glauber model is a multiple collision model which treats a nucleus-nucleus collision as an independent sequence of nucleon-nucleon collisions, see [158] and references therein. The nucleons in a nucleus are distributed according to a Fermi (or Woods-Saxon) distribution:

$$\rho(r) = \frac{\rho_0(1 + wr^2/R^2)}{1 + e^{(r-R)/a}} \tag{4.1}$$

where R is the nucleon radius, a the surface thickness, w characterizes deviations from a spherical shape, and ρ_0 is a normalization factor chosen so that $\int d^3r\rho(r) = 1$. For the case of ^{208}Pb, the parameters utilized are $R = 6.62$ fm, $a = 0.546$ fm and $w = 0$.

The model assumes that nucleons in each nucleus travel on straight-line trajectories through the colliding system and interact according to the inelastic nucleon-nucleon cross section, σ_{inel}^{NN}, as measured in p+p collisions. The nominal value used for Pb+Pb collisions at $\sqrt{s_{NN}} = 2.76$ TeV is taken as $\sigma_{inel}^{NN} = 64$ mb.

The distance between the center of two colliding heavy ions is described by the impact parameter b. Additional quantities of primary interest that can be extracted from the Glauber modeling are the number of participating nucleons $N_{\rm part}$, the number of binary collisions $N_{\rm coll}$, the initial state spatial anisotropy ϵ_n and the transverse overlap area S as discussed in Chapter 2

The Glauber calculation can be implemented either by the optical model or in a Monte Carlo

Table 4.1: Fraction of MB triggered events after event selections in each multiplicity bin, and the average multiplicity of reconstructed tracks per bin with $|\eta| < 2.4$ and $p_T > 0.4$ GeV/c, before and after efficiency correction, for 2.76 TeV PbPb and 5.02 TeV pPb data.

	PbPb data			pPb data		
$N_{trk}^{offline}$ bin	$\langle Centrality \rangle$ $\pm$ RMS (%)	$\langle N_{trk}^{offline} \rangle$	$\langle N_{\rm trk}^{\rm corrected} \rangle$	Fraction	$\langle N_{trk}^{offline} \rangle$	$\langle N_{\rm trk}^{\rm corrected} \rangle$
$[0, \infty)$				1.00	40	50±2
$[0, 20)$	92±4	10	13±1	0.31	10	12±1
$[20, 30)$	86±4	24	30±1	0.14	25	30±1
$[30, 40)$	83±4	34	43±2	0.12	35	42±2
$[40, 50)$	80±4	44	55±2	0.10	45	54±2
$[50, 60)$	78±3	54	68±3	0.09	54	66±3
$[60, 80)$	75±3	69	87±4	0.12	69	84±4
$[80, 100)$	72±3	89	112±5	0.07	89	108±5
$[100, 120)$	70±3	109	137±6	0.03	109	132±6
$[120, 150)$	67±3	134	168±7	0.02	132	159±7
$[150, 185)$	64±3	167	210±9	4×10^{-3}	162	195±9
$[185, 220)$	62±2	202	253±11	5×10^{-4}	196	236±10
$[220, 260)$	59±2	239	299±13	6×10^{-5}	232	280±12
$[260, 300)$	57±2	279	350±15	3×10^{-6}	271	328±14
$[300, 350)$	55±2	324	405±18	1×10^{-7}	311	374±16

generator. The optical model is based on an analytic method of classically overlapping nuclei. The Monte Carlo approach is based on a computer simulation of billiard ball like colliding nucleons. In the Glauber Monte Carlo, a nucleon-nucleon collision takes place if their relative transverse distance D in the plane orthogonal to the beam axis satisfies $D < \sqrt{\sigma_{inel}^{NN}/\pi}$. An additional parameter of the Glauber Monte Carlo is the minimum inter-nucleon separation between the centers of the nucleons themselves, and this is nominally set to be $d_{\rm min} = 0.4$ fm, as was done for similar calculations at lower (RHIC) energies [159]. An example of PbPb collision from such a Monte Carlo Glauber model is shown in Fig. 4.4.

4.3 Charged-Particle Reconstruction

To determine the flow coefficients of the charged particles produced in the collisions, we first need to reconstruct the particles' trajectories ("tracks") through the 3.8 T solenoidal magnetic field. The tracks are reconstructed by starting with a "seed" comprising two or three reconstructed signals ("hits") in the inner layers of the silicon strip and pixel detectors that are compatible with a helical trajectory of some minimum p_T and a selected region around the reconstructed primary vertex or nominal interaction point. This seed is then propagated outward through subsequent layers using a combinatorial Kalman-filter algorithm. Tracking is generally performed in multiple iterations, varying the layers used in the seeding and the parameters used in the pattern recognition, and removing duplicate tracks between iterations. This algorithm is described in detail in [160].

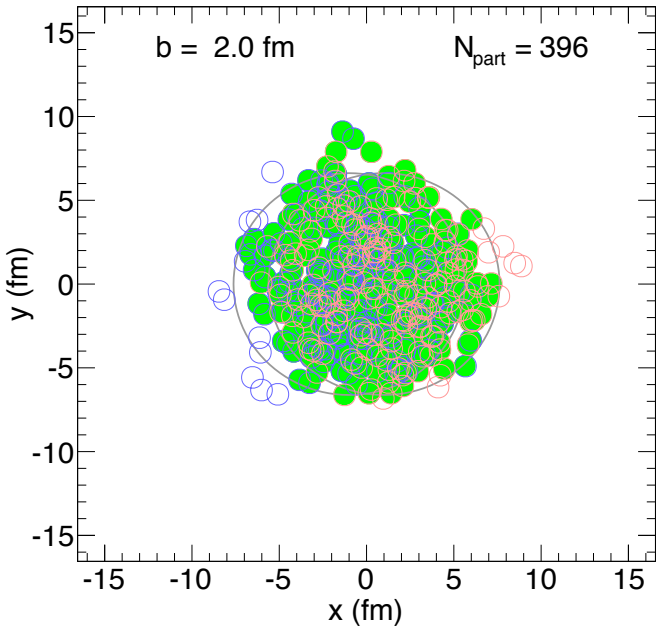

Figure 4.4: Schematic view of a PbPb collision with impact parameters of $b = 2.0$ fm as obtained from the Glauber model. Nucleons from each nucleus are shown as blue or red open circles respectively. The nucleons that participate in inelastic collisions are marked with filled green circles. The number of participating nucleons, N_{part}, is shown.

The algorithm used in most of the CMS pp and pPb analyses, as well as the tracking detector performance for the 2010 run, are described in [161].

The six-iteration process used in proton-lead collisions is computationally not feasible in the high-multiplicity environment of very central PbPb collisions. In place of this, a simple two-iteration process is used. The first iteration builds seeds from hits in some combination of three layers in the barrel and endcap pixel detectors compatible with a trajectory of $p_T > 0.9$ GeV/c and a distance of closest approach to the reconstructed vertex of no more than 0.1 cm in the transverse plane and 0.2 cm longitudinally. These tracks are then filtered using selection criteria based on a minimum number of reconstructed hits, vertex compatibility along the longitudinal direction and in the transverse plane, and low relative uncertainty on the reconstructed momentum.

In the second iteration, seeding is also performed using three layers of the pixel detector, but the minimum transverse momentum requirement is relaxed to $p_T > 0.2$ GeV/c. These tracks are not propagated through the silicon-strip detector, but simply refitted using the transverse position of the beam spot as an additional constraint. These pixel-only tracks are then filtered using selection criteria of vertex compatibility along the longitudinal axis and statistical goodness of fit.

The tracks from both collections are checked for duplicate tracks using the number of hits in common between the two tracks, and duplicates are removed giving preference to the first-iteration tracks. The tracking algorithm may sometimes misidentify tracks by combining silicon detector signals that do not originate from the same charged particle. It is important to keep the proportion of misidentified tracks (referred to as "fake tracks"), or fake rate, as low as possible. To create the final

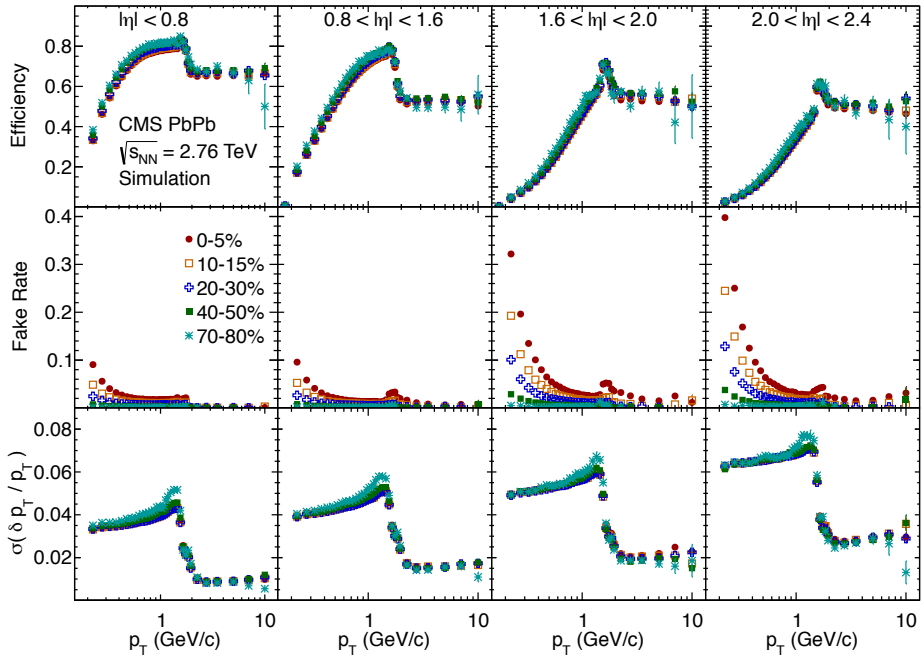

Figure 4.5: Efficiency (top), fake rate (middle), and momentum resolution (bottom) of charged tracks obtained from HYDJET simulated events in four pseudorapidity regions: $|\eta| < 0.8$, $0.8 < |\eta| < 1.6$, $1.6 < |\eta| < 2.0$, and $2.0 < |\eta| < 2.4$ displayed from left to right, and for the five centrality classes given in the legend.

collection, first-iteration tracks with $p_T > 1.5$ GeV/c are combined with second-iteration pixel-only tracks with $p_T < 1.8$ GeV/c. These p_T limits were chosen to exclude kinematic regions where a given iteration has a high fake rate. The efficiency and fake rate of this modified tracking collection are found both by using a full MC simulation of PbPb collisions based on the HYDJET event generator [162] and by embedding simulated charged pions into PbPb data events. The efficiency, fake rate, and momentum resolution of this final collection determined by the simulated events from the HYDJET event generator are shown in Figure 4.5 for events of five different centrality classes. The abrupt change in efficiency, fake rate, and momentum resolution seen in the figure occurs at the transverse momentum where the two track collections are merged.

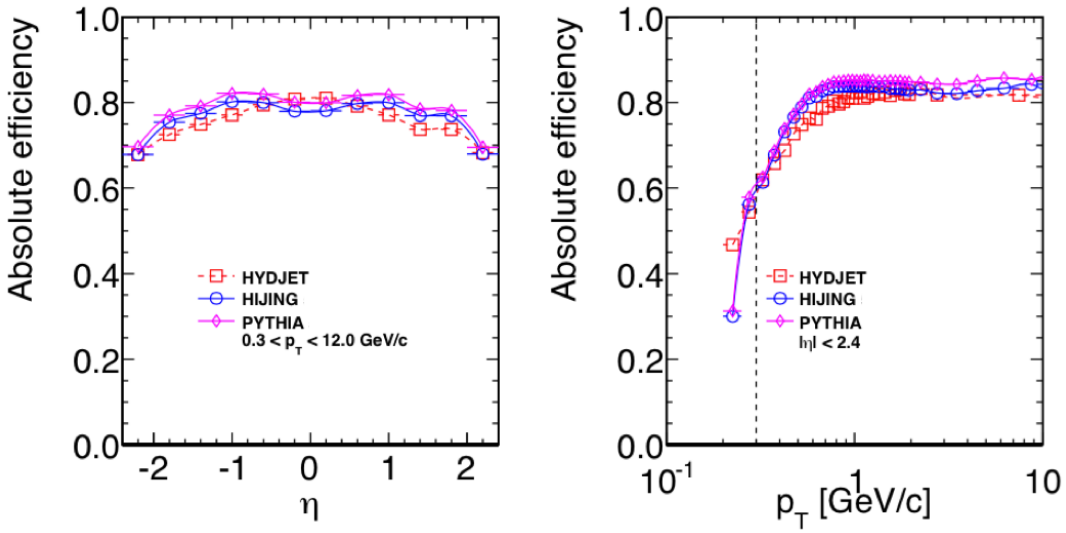

Figure 4.6: The efficiency of the charged tracks obtained from PYTHIA, HIJING and HYDJET peripheral simulated events as a function of η for $0.3 < p_T < 12.0$ GeV/c (left) and p_T with $|\eta| < 2.4$ (right). The dashed line shows the low p_T limit used in the pPb analysis.

For pPb collisions, the CMS *highPurity* [163] tracks were used. Additionally, a reconstructed track was only considered as a primary-track candidate if the significance of the separation along the beam axis (z) between the track and the best vertex, $d_z/\sigma(d_z)$, and the significance of the impact parameter relative to the best vertex transverse to the beam, $d_{\mathrm{T}}/\sigma(d_{\mathrm{T}})$, were each less than 3. The relative uncertainty of the transverse-momentum measurement, $\sigma(p_{\mathrm{T}})/p_{\mathrm{T}}$, was required to be less than 10%. The efficiency and fake rate are shown in Figure 4.6 and Figure 4.7. To ensure high tracking efficiency and reduce the rate of misidentified tracks, only tracks within $|\eta| < 2.4$ and with $p_T > 0.3$ GeV/c were used in the analysis.

4.4 Correction to v_n from Fake Tracks

In determining the $v_2(p_T)$ distributions for particles detected in the tracker, it is necessary to correct for the influence of fake tracks on the measurements. As shown in Section 4.3, the fake-track contribution is particularly significant at low-p_T values and for pseudorapidities $|\eta| > 1.6$. Of

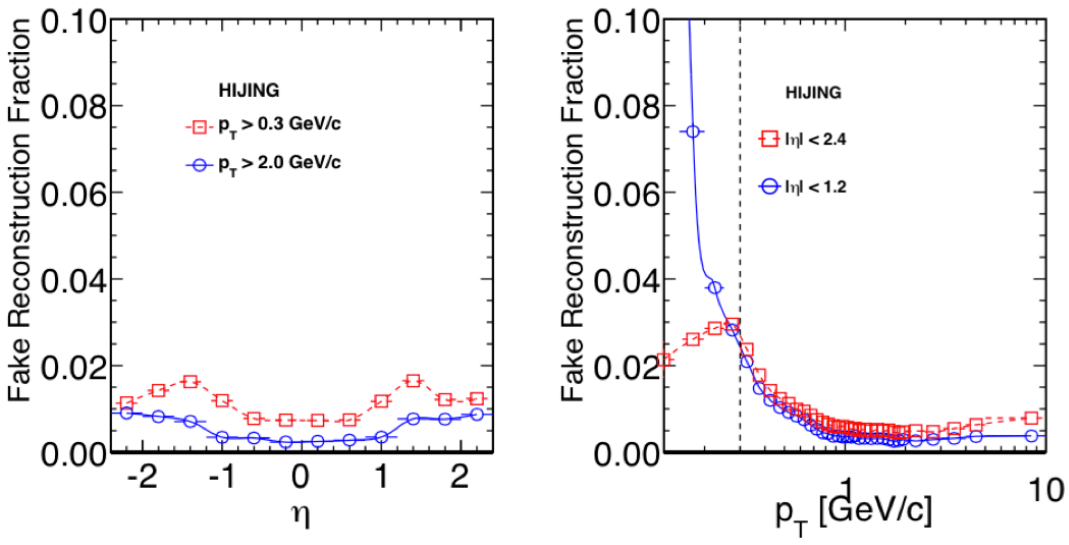

Figure 4.7: The fake rate of charged tracks obtained from HIJING simulation as a function of η (left) and p_T (right). The dashed line shows the low p_T limit used in the pPb analysis.

particular concern is the observation that the fake tracks can carry a v_2 signal at low p_T similar to that of properly reconstructed (i.e., "real") tracks at a higher p_T. Since the true v_2 signal is very small at low p_T, but increases at higher p_T, the fake tracks may contribute a significant fraction of the measured v_2 signal at low p_T.

Studies using a full MC CMS simulation of PbPb collisions based on the HYDJET event generator indicate that the component of the v_2 signal due to fake tracks is relatively constant for $p_T < 0.8$ GeV/c, where the fraction of fake tracks is largest. For higher p_T, where the fraction of fake tracks is quite small, the value of v_2 is consistent with the measured value from correctly reconstructed tracks. This suggests the following simple correction scheme. Let $N_{\rm det}(p_T)$ be the number of reconstructed tracks in a given p_T bin, f the fraction of these tracks that are "fake," $N_{\rm true}$ the number of "true" tracks in the p_T bin, and e the efficiency for reconstructing a true track in the bin. Then $N_{\rm det} - fN_{\rm det} = eN_{\rm true}$. The $fN_{\rm det}$ fake tracks are characterized by a constant v_2 value given by $v_2^{\rm fake}$. The $N_{\rm det} - fN_{\rm det}$ real tracks are characterized by $v_2^{\rm real}$. Then the observed value $v_2^{\rm obs}$ of v_2 will be

$$v_2^{\rm obs} = (1-f)v_2^{\rm real} + fv_2^{\rm fake} \tag{4.2}$$

and so

$$v_2^{\rm real} = \frac{v_2^{\rm obs} - fv_2^{\rm fake}}{1-f}. \tag{4.3}$$

This correction for the fake track signal is only significant for p_T values less than ≈1 GeV/c. In this range, an empirical correction that results in values of v_2 that are independent of the track selection requirements or fraction of fake tracks is applied using $v_2^{\rm fake} = 1.3\,\langle v_2 \rangle$, where the yield-weighted

average is performed over the transverse momentum range 0.3 to 3 GeV/c, folding in the efficiency-corrected spectra. This value for v_2^{fake} is also supported by MC studies using HYDJET.

4.5 Systematic Uncertainties

4.5.1 Systematic Uncertainties for $v_2\{LYZ\}$, $v_4\{LYZ\}$ and $v_6\{LYZ\}$ in Central and Mid-central PbPb Collisions

The systematic uncertainties for $v_n\{LYZ\}$ are evaluated as relative uncertainties and are reported as percentages relative to the measured v_n values. Since we are studying v_n for non-identified charged particles, and considering the fact that different particles show different v_n, it is important to investigate the tracking efficiency as a function of particle species. The tracking efficiencies for charged pions, kaons, protons, and antiprotons are determined using a full simulation of CMS. Subsequently, the value of $v_n(p_T)$ for charged particles is obtained using different assumptions for the p_T-dependence of v_n and the transverse momentum spectra of each particle type, taking into account the corresponding reconstruction efficiencies. The results are compared to those obtained with the assumption of a particle-species-independent efficiency. The uncertainties in the charged particle v_n results are estimated to be $\lesssim 0.5\%$, independent of the p_T, η, and centrality ranges. This uncertainty is listed as "Part. composition" in Tables 4.2–4.5.

Since the v_n value changes with centrality, an uncertainty in the centrality determination can lead to a shift in the v_n measurement. This uncertainty is evaluated by varying the value of the minimum-bias trigger efficiency to include $(97 \pm 3)\%$ of the total inelastic cross section. The resulting uncertainty on v_n is of the order 1%, independent of the p_T, η, and centrality ranges. This uncertainty is listed as "Cent. determination" in Tables 4.2–4.5.

The multiparticle correlation methods are sensitive to the multiplicity fluctuations in a set of analyzed data. This systematic uncertainty is studied by comparing the results from large centrality bin to smaller centrality bins, or by comparing the results from large multiplicity bin to smaller multiplicity bins.

The kinematic requirements used to select tracks can affect the efficiency of track finding and the relative fraction of fake tracks in an event. The requirements are varied from their default values to estimate the systematic uncertainty. For each set of requirements, corresponding corrections are obtained for the fake-track contribution to the v_n signal, as described in Section 4.4. For a given centrality and p_T range, the systematic uncertainty is estimated based on the stability of the v_n value after corrections for fake tracks, independent of the track selection requirements. The uncertainty is found to be directly related to the magnitude of the fake-track contribution, with the final results deemed unreliable when the fake-rate is higher than ≈20%. The systematic uncertainties from this source remain below 4% over the entire range of p_T, η, and centrality, and are significantly below this value for $p_T > 0.5$ GeV/c, centrality above 10%, and $|\eta| < 1.6$. The uncertainty in the efficiency corrections is evaluated by determining the efficiency based on the HYDJET model, and by embedding simulated pions into PbPb events in data. Although the two resulting efficiencies do have differences, the uncertainty on the v_n value is small, at most 0.5%. Variations in the

v_n results due to changing detector conditions throughout the data-taking period are studied by dividing the data into three subgroups and are found to be below 1% for all measurements. The combined uncertainties from the efficiency corrections, fake-track corrections, and variations in detector conditions are listed under "Corrections" in Tables 4.2–4.5.

The overall systematic uncertainties are from 1.7 to 10% for different v_n at different p_T range. A summary of the systematic uncertainties for $v_2\{LYZ\}$, $v_4\{LYZ\}$ and $v_6\{LYZ\}$ in central and mid-central PbPb collisions is presented in Tables 4.2–4.5.

Table 4.2: Systematic uncertainties in the measurement of $v_2(p_T)$ for $|\eta| < 0.8$ with the Lee–Yang zeros method for different p_T and centrality ranges.

Source	p_T (GeV/c)	Centrality		
		5 – 10%	10 – 40%	40 – 50%
Part. composition	All	0.5%	0.5%	0.5%
Cent. determination	All	1.0%	1.0%	1.0%
Multiplicity fluct.	All	0.1%	0.9%	1.9%
Corrections	0.3 – 0.5	2.5%	1.7%	0.7%
	0.5 – 22.0	1.5%	1.0%	0.6%
Total	0.3 – 0.5	2.7%	2.2%	2.3%
	0.5 – 22.0	1.9%	1.8%	2.3%

Table 4.3: Systematic uncertainties in the measurement of $v_2(\eta)$ for $0.3 < p_T < 3$ GeV/c with the Lee–Yang zeros method for different η and centrality ranges.

Source	$\|\eta\|$	Centrality		
		5 – 10%	10 – 40%	40 – 50%
Part. composition	All	0.5%	0.5%	0.5%
Cent. determination	All	1.0%	1.0%	1.0%
Multiplicity fluct.	All	0.1%	0.9%	1.9%
Corrections	0.0 – 1.6	1.3%	1.0%	0.8%
	1.6 – 2.4	1.5%	1.4%	1.3%
Total	0.0 – 1.6	1.7%	1.8%	2.4%
	1.6 – 2.4	1.9%	2.0%	2.5%

4.5.2 Systematic Uncertainties for $v_2\{4\}$ and $v_2\{LYZ\}$ in Semi-peripheral PbPb and High Multiplicity pPb Collisions

For the charged particle reconstruction in pPb and semi-peripheral collisions, the combined geometrical acceptance and efficiency for track reconstruction exceeds 60% for $p_T \approx 0.3$ GeV/c and $|\eta| < 2.4$. For the entire multiplicity range studied, no dependence of the tracking efficiency on multiplicity is found and the rate of mis-reconstructed tracks remains at the 1–2% level.

Systematic uncertainties due to track quality requirements are examined by varying the track selections for $d_z/\sigma(d_z)$ and $d_{xy}/\sigma(d_{xy})$ from 2 to 5. The results of $v_2\{4\}$ are found to be insensitive

Table 4.4: Systematic uncertainties in the $v_4\{LYZ\}$ values as a function of centrality are shown at the top of the table, followed by those specific to the differential (p_T dependent) and integral ($|\eta|$ dependent) measurements.

Source		**Centrality**		
		5–10%	10–40%	40–60%
Particle Composition		0.5	0.5	0.5
Centrality Determination		1.0	1.0	1.0
Multiplicity Fluctuations		0.1	0.9	2.0
[Differential]	(GeV/c)			
Corrections	0.3–0.5	10	7.0	3.0
	0.5–8.0	3.0	2.0	1.0
Total (p_{T})	0.3–0.5	10	7.1	3.8
	0.5–8.0	3.2	2.5	2.5
[Integral]	$\|\eta\|$			
Corrections	0.0–0.8	3.0	2.0	3.0
Total $\|\eta\|$	0.0–0.8	3.2	2.5	3.8

Table 4.5: Systematic uncertainties in the $v_6\{LYZ\}$ values as a function of centrality are shown at the top of the table, followed by those specific to the differential (p_T dependent) and integral ($|\eta|$ dependent) measurements.

Source		**Centrality**		
		5–10%	10–40%	40–60%
Particle Composition		0.5	0.5	0.5
Centrality Determination		1.0	1.0	1.0
Multiplicity Fluctuations		0.1	0.9	2.0
[Differential]	p_T (GeV/c)			
Corrections	0.3–0.5	16	12	7.5
	0.5–8.0	6.0	4.0	3.0
Total p_T	0.3–0.5	16	13	7.8
	0.5–8.0	6.1	4.2	3.8
[Integral]	$\|\eta\|$			
Corrections	0.0–0.8	3.0	2.5	3.5
Total $\|\eta\|$	0.0–0.8	3.2	2.9	4.2

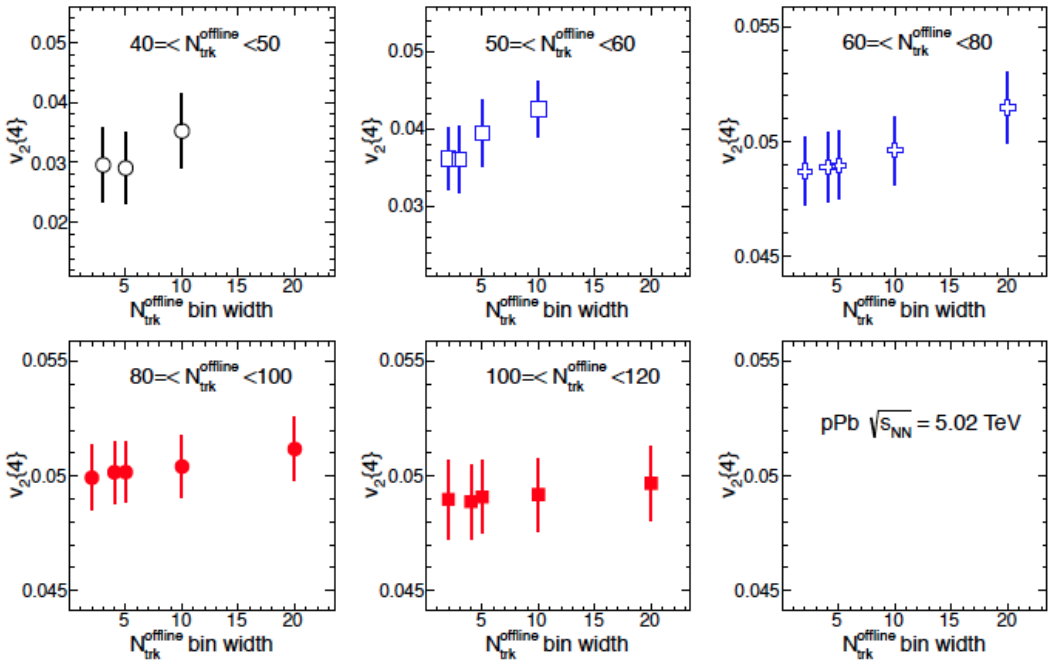

Figure 4.8: The values of $v_2\{4\}$ as a function of analysis multiplicity bin width in different $N_{trk}^{offline}$ ranges.

to these track selections within 2.5%. A comparison of high-multiplicity pPb data for a given multiplicity range but collected by two different HLT triggers with different trigger efficiencies shows an agreement within 2%. The uncertainties from tracking efficiency correction are found to be less than 0.5%. Possible contamination of residual pileup events is also investigated. By varying the z_{vtx} range in performing the analysis, the pileup probability is expected to vary by a factor of 3–4. The systematic uncertainties for $v_2\{4\}$ from possible residual pileup effects are estimated to be 2% for $N_{trk}^{offline} < 260$, increasing to 6% for $N_{trk}^{offline} \geq 260$.

The event-by-event variation of track multiplicity within a given multiplicity bin width is found to have an effect on $v_2\{4\}$, especially for the low-multiplicity region. The $c_2\{4\}$ values calculated directly for a multiplicity bin width of 30 show a large discrepancy from those derived first using a smaller bin width (e.g., 2 or 5) and then averaged over the same wider bin as will be shown in Figure 6.1 later. Studies performed with different $N_{trk}^{offline}$ bin widths, allowing different multiplicity content in the bins, suggest a systematic uncertainty of only 1% for $N_{trk}^{offline} > 100$ but up to 10% for the low multiplicity region $N_{trk}^{offline} < 60$. Figure 4.8 shows the values of $v_2\{4\}$ as a function of analysis $N_{trk}^{offline}$ bin width in different multiplicity ranges. It is clear from the top three panels that the $v_2\{4\}$ results using large bin size (>10) are larger than the results using small bin width.

The different systematic sources described above are added in quadrature to obtain the overall systematic uncertainty. Table 4.6 summarizes different sources of systematic uncertainties of $v_2\{4\}$.

The systematic uncertainties of $v_2\{LYZ\}$ are similar to that of $v_2\{4\}$. The $N_{trk}^{offline}$ range for $v_2\{LYZ\}$ analysis is from 120 to 260, which is within the bin range of $N_{trk}^{offline}$ from 100 to 260 in

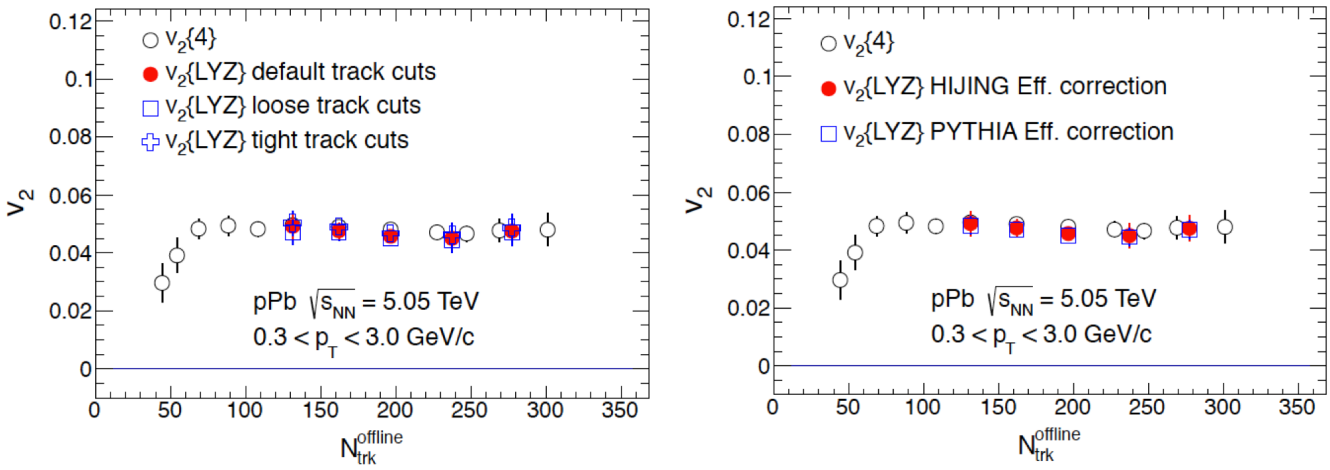

Figure 4.9: Left: The integrated $v_2\{LYZ\}$ as a function of $N_{trk}^{offline}$ from different track quality requirements. The default track selections require $d_z/\sigma(d_z) < 3$ and $d_{xy}/\sigma(d_{xy}) < 3$. The loose track quality selections are $d_z/\sigma(d_z) < 5$ and $d_{xy}/\sigma(d_{xy}) < 5$. The tight one requires $d_z/\sigma(d_z) < 2$ and $d_{xy}/\sigma(d_{xy}) < 2$. Right: The integrated $v_2\{LYZ\}$ as a function of $N_{trk}^{offline}$ from using different tracking efficiency corrections. The difference of $v_2\{LYZ\}$ between different corrections are taken as systematic uncertainty from this study.

Table 4.6. Thus, the systematic uncertainties of $v_2\{LYZ\}$ do not change within the large bin. The left hand side of Figure 4.9 shows the integrated $v_2\{LYZ\}$ as a function of $N_{trk}^{offline}$ from different track quality requirements. The default track selections require $d_z/\sigma(d_z) < 3$ and $d_{xy}/\sigma(d_{xy}) < 3$. The loose track quality selections are $d_z/\sigma(d_z) < 5$ and $d_{xy}/\sigma(d_{xy}) < 5$. The tight one requires $d_z/\sigma(d_z) < 2$ and $d_{xy}/\sigma(d_{xy}) < 2$. The values of integrated $v_2\{LYZ\}$ as a function of $N_{trk}^{offline}$ from using different tracking efficiency corrections are shown in the right hand side of Figure 4.9. The systematic uncertainties of $v_2\{LYZ\}$ from track quality cuts, HLT trigger bias, correction for track efficiency, multiplicity fluctuation, effect from pileups and vertex dependence are 2.5%, 2.0%, 1.5%, 1.5%, 1.0% and 2.0%. The overall systematic uncertainty is about 4.8%.

Table 4.6: Summary of systematic uncertainties in $v_2\{4\}$

	$N_{trk}^{offline}$			
Source	$[40, 60)$	$[60, 100)$	$[100, 260)$	$[260, 350)$
Track quality cuts	2.5%	2.5%	2.5%	2.5%
HLT trigger bias	2.0%	2.0%	2.0%	2.0%
Correction for track efficiency	0.5%	0.5%	0.5%	0.5%
Multiplicity fluctuation	10.0%	5.0%	1.0%	1.0%
Effect from pileups	1.0%	1.0%	1.0%	3.0%
Vertex dependence	2.0%	2.0%	2.0%	6.0%
Total	10.7%	6.4%	4.1%	7.5%

Chapter 5

Collective Flow Results in PbPb Collisions

The CMS collaboration has studied different aspects of the collective behavior of the charged particles produced in PbPb collisions. We measured the values of the Fourier coefficients of the azimuthal particle distributions v_n with n from 2 - 6, using the event-plane method, 2-particle correlations, 4-particle correlations and the Lee-Yang Zeros method as a function of the transverse momentum, pseudorapidity and centrality. The measurements are published in [104] and [164]. My contributions to the papers are the flow results from the LYZ method and the studies of the initial collision geometry and the corresponding participant distributions using the Glauber model.

The measurement of higher order flow coefficients provides strong constraints on the initial spatial distribution of the energy density in heavy ion collisions, its fluctuations on an event-by-event basis, as well as on the shear viscosity to entropy density ratio. This is due to the fact that the initial spatial asymmetries of higher order harmonics originate in the event-by-event initial state fluctuations; initial anisotropies are dissipated through the evolution of the system and the value of the shear viscosity can be extracted because it damps down all the flow coefficients. As we discussed in Chapter 2, different methods have different sensitivity to the effects of non-flow and flow fluctuations. With the results from different methods, it is possible to estimate the size of flow fluctuations. The underlying physics processes that generate the flow coefficients vary for different transverse momentum regions, with the low p_T ($p_T < 2$ GeV/c for mesons, and $p_T < 3$ GeV/c for baryons) driven by pressure gradients in the system, the intermediate p_T ($2 < p_T < 4$ GeV/c) from the recombination of quarks, and the high and intermediate p_T ($p_T > 3$ GeV/c) from the fragments of hard partons that produce anisotropy of hadrons from the path-length dependence of energy loss in the medium. The pseudorapidity dependence of the flow coefficients provides information on the initial state and the early-time development of the collision, constraining the theoretical models and the description of the longitudinal dynamics in the collisions. The centrality dependence of integrated v_n provides constraints on η/s by comparing v_n/ϵ_n between data and theoretical calculations.

5.1 Transverse Momentum Dependence of v_n

The measurements of v_2 from different methods, including $v_2\{LYZ\}$, for charged particles as a function of transverse momentum at mid-rapidity are presented in Figure 5.1. The four methods show differences as expected due to their sensitivities to non-flow contributions and flow fluctuations. The method that is most affected by non-flow correlations is the two-particle cumulant, because of the fact that the reference and the differential flow signals are determined in the same pseudorapidity range. The event plane method is expected to be similarly affected if dedicated selections are not applied to reduce these contributions. In our analysis, the particles used in the event plane determination and the particles used to measure the flow are at least 3 units of pseudorapidity apart,

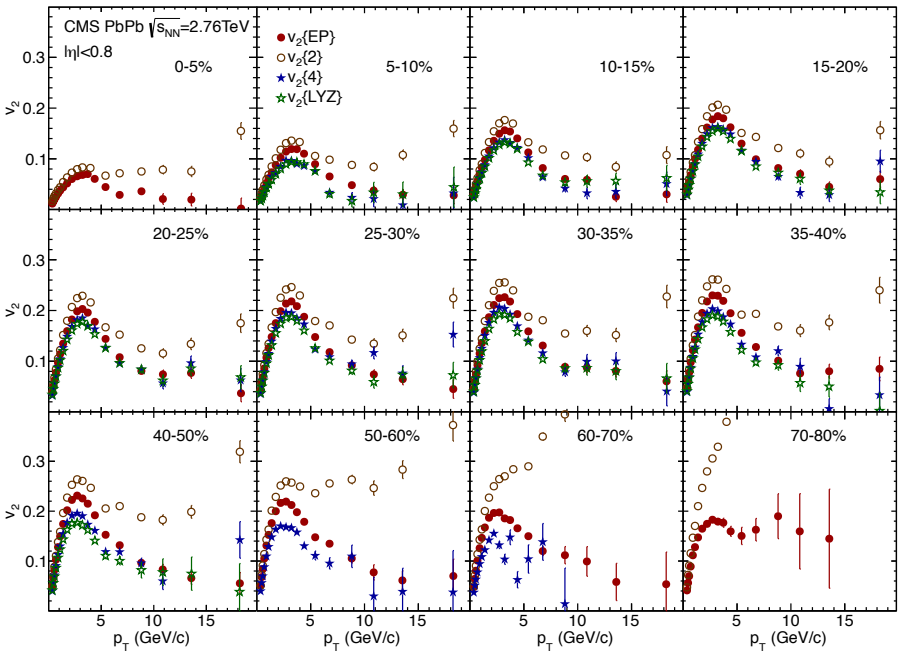

Figure 5.1: Comparison of the four different methods for determining v_2 as a function of p_T at mid-rapidity ($|\eta| < 0.8$) for the 12 centrality classes given in the figures. The error bars show the statistical uncertainties only. These results were published in [104].

which suppresses most non-flow correlations. The differences between the two-particle cumulant and the event plane methods are most pronounced at high p_T and in peripheral collisions, where jet-induced correlations dominate over the collective flow. The results from the four-particle cumulant and Lee-Yang Zeros methods are smaller than those from the two-particle cumulant and event plane methods. This is because $v_2\{4\}$ and $v_2\{LYZ\}$ are much less affected by non-flow contributions and, more importantly, they are suppressed from the effect of flow fluctuations as we discussed in Chapter 2. The results of $v_2\{4\}$ and $v_2\{LYZ\}$ are very close, which indicates that four-particle correlations already remove most of the non-flow. One can already see the complexity of the flow measurements. The true v_2 should be somewhere between v_{EP} and $v_2\{4\}$. A theoretical calculation of v_2 needs to use the same method as data for comparison, otherwise the results might be misinterpreted.

The value of v_2 increases from central to peripheral collisions up to the collisions with 40% centrality, as expected if the final momentum space anisotropy is driven by the spatial anisotropy in the initial state. The results from the Lee-Yang Zeros method are shown in the centrality range 5-50%. For the central 0-5% the method fails because the v_2 value is very small, and for peripheral 50-80% centralities because the multiplicity is very small and the systematic uncertainty from event-by-event multiplicity fluctuations is large. The transverse momentum dependence shows a rise of v_2 up to $p_T \approx 3$ GeV/c and then a decrease. In ideal hydrodynamics the azimuthal anisotropy continuously increases with increasing p_T [38, 165]. The deviation of the theory from the data at $p_T > 2$ GeV/c has been attributed to incomplete thermalization of the high p_T hadrons, and the effects of viscosity. Indeed, viscous hydrodynamic calculations [40, 127, 166] show that the shear viscosity has the effect

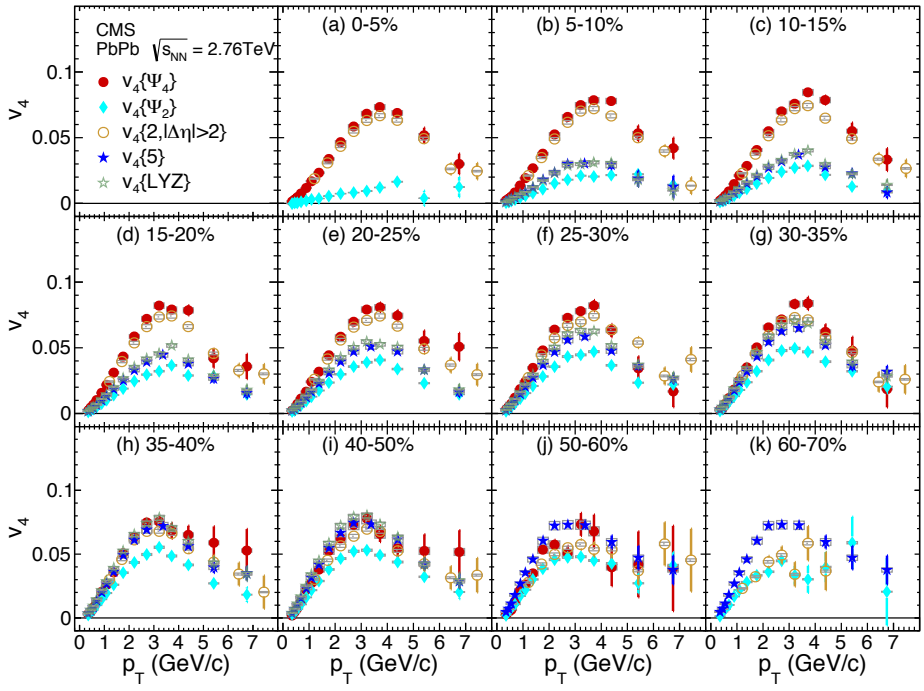

Figure 5.2: Measurements of the flow coefficient v_4 from different methods as a function of p_T for the indicated centrality bins, as specified in percent. The event plane (filled circles and filled diamonds), cumulant (filled stars), and Lee-Yang Zeros (open stars) analyses are with $|\eta| < 0.8$. The two particle correlation results (open circles) are from [116]. Results from other methods were published in [164].

of reducing the anisotropy at high p_T. At p_T >8 GeV/c, where hadron production is dominated by jet fragmentation, the collective-flow effects are expected to disappear [40, 165]. Instead, an asymmetry in the azimuthal distribution of hadron emission with respect to the participant plane could be generated by the path-length-dependent parton energy loss [167–169].

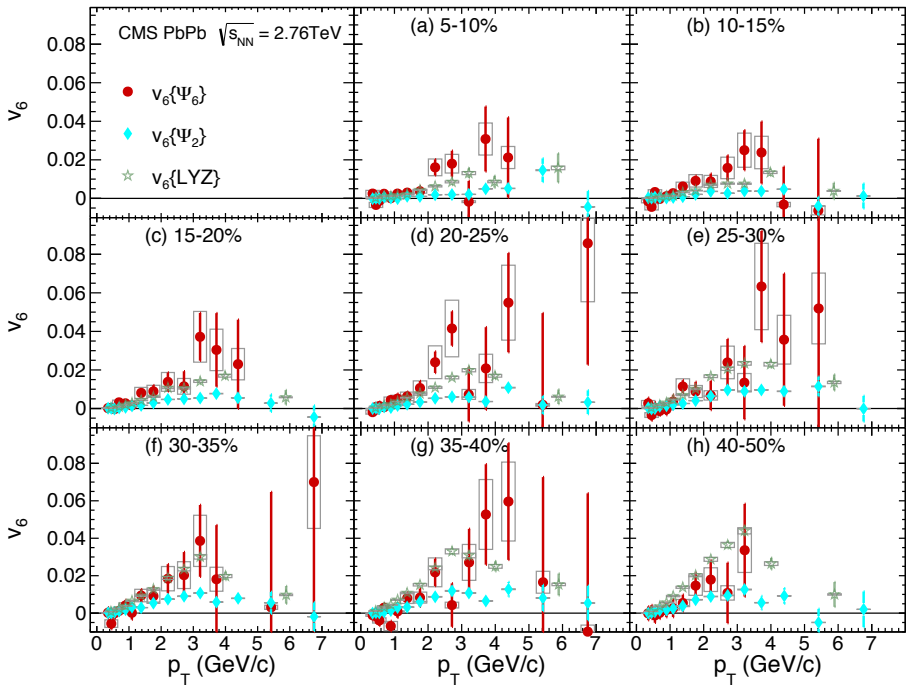

Figure 5.3: Measurements of the flow coefficient v_6 from the event plane (filled circles and filled diamonds) and Lee-Yang Zeros (open stars) methods as a function of p_T for the indicated centrality bins, as specified in percent. These results were published in [164].

Figure 5.2 shows the v_4 values from different methods. The event plane results are shown based on both the fourth-order event plane angle as well as the second-order event plane angle. The values $v_4\{2, |\Delta\eta| > 2\}$ are from the long-range two particle correlation method. The $v_4\{5\}$ and $v_4\{LYZ\}$ are from the five-particle cumulant and Lee-Yang Zeros methods. The shape of v_4 as a function of p_T is similar to that of v_2. The values of $v_4\{\Psi_4\}$ and $v_4\{2, |\Delta\eta| > 2\}$ are very close since they are both with respect to the fourth-order references. One can see that they have little centrality dependence, which means indeed they might come from the fluctuations of initial state that depend on centrality weakly. A significant centrality dependence is observed for the $v_4\{\Psi_2\}$, $v_4\{5\}$, and $v_4\{LYZ\}$ results, which are all based on a second-order reference distribution since $v_4\{\Psi_2\}$ uses the second-order event plane angle, $v_4\{5\}$ and $v_4\{LYZ\}$ are using the reference v_2 as an input for the calculation of p_T dependent v_4. The values of $v_4\{\Psi_2\}$ are smaller than those of $v_4\{5\}$ and $v_4\{LYZ\}$ which is understood because of the fact that the fluctuations of v_4 affect these methods differently.

Similarly, Figure 5.3 shows the results for v_6 from the event plane and Lee-Yang Zeros methods as a function of p_T for different centrality bins. The event plane results use both the sixth-order event plane angle and the second-order event plane angle. The results of $v_2\{LYZ\}$ are used in the calculation of $v_6\{LYZ\}$ as a function of p_T. The higher values and relatively weak centrality

dependence found for the $v_6\{\Psi_6\}$ results are consistent with these values being strongly influenced by fluctuations.

5.2 Centrality and Pseudorapidity Dependence of v_n

To obtain the integrated v_n values as a function of centrality at mid-rapidity, $v_2(p_T)$ measurements are averaged over p_T, weighted by the corresponding charged-particle spectrum. The integration range $0.3 < p_T < 3$ GeV/c is limited to low p_T to maximize the contribution from soft processes, which facilitates comparisons to hydrodynamic calculations.

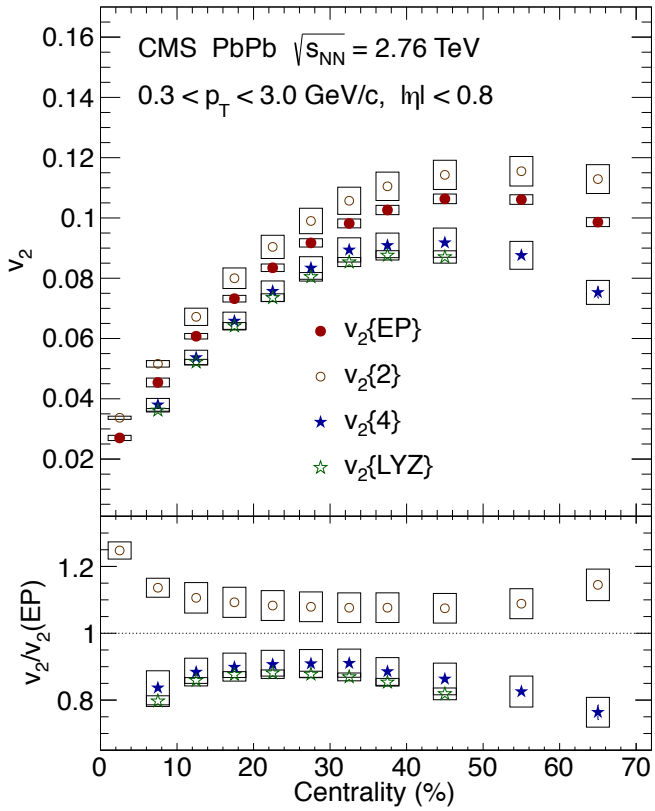

Figure 5.4: Top panel: Integrated v_2 as a function of centrality at mid-rapidity $|\eta| < 0.8$ for the four methods. The boxes represent the systematic uncertainties. The magnitudes of the statistical uncertainties are smaller than the size of the symbols. Bottom panel: The values from three of the methods are divided by the results from the event-plane method. The boxes represent the systematic uncertainties excluding the sources that are common to all methods. The magnitudes of the statistical uncertainties are smaller than the size of the symbols. These results were published in [104].

The centrality dependence of the integrated v_2 at mid-rapidity $|\eta| < 0.8$ is presented in Figure 5.4, for the four methods. The v_2 values increase from central to peripheral collisions, reaching a maximum in the 40-50% centrality range. In the more peripheral collisions, a decrease in v_2 is observed in the event-plane and four-particle cumulant measurements, while the values obtained

with the two-particle cumulant method remain constant within their uncertainties. The results for $v_2\{2\}$ are larger than those for $v_2\{EP\}$, while the $v_2\{4\}$ and $v_2\{LYZ\}$ values are smaller. To facilitate a quantitative comparison between the methods, including their respective systematic uncertainties, the bottom panel of Figure 5.4 shows the results from the cumulant and the Lee-Yang Zeros methods divided by those obtained from the event-plane method. The boxes represent the systematic uncertainty in the ratios, excluding sources of uncertainty common to all methods. The ratios are relatively constant in the 10-60% centrality range, but the differences between the methods increase for the most central and the most peripheral collisions. These findings are similar to results obtained by the STAR experiment at RHIC [170].

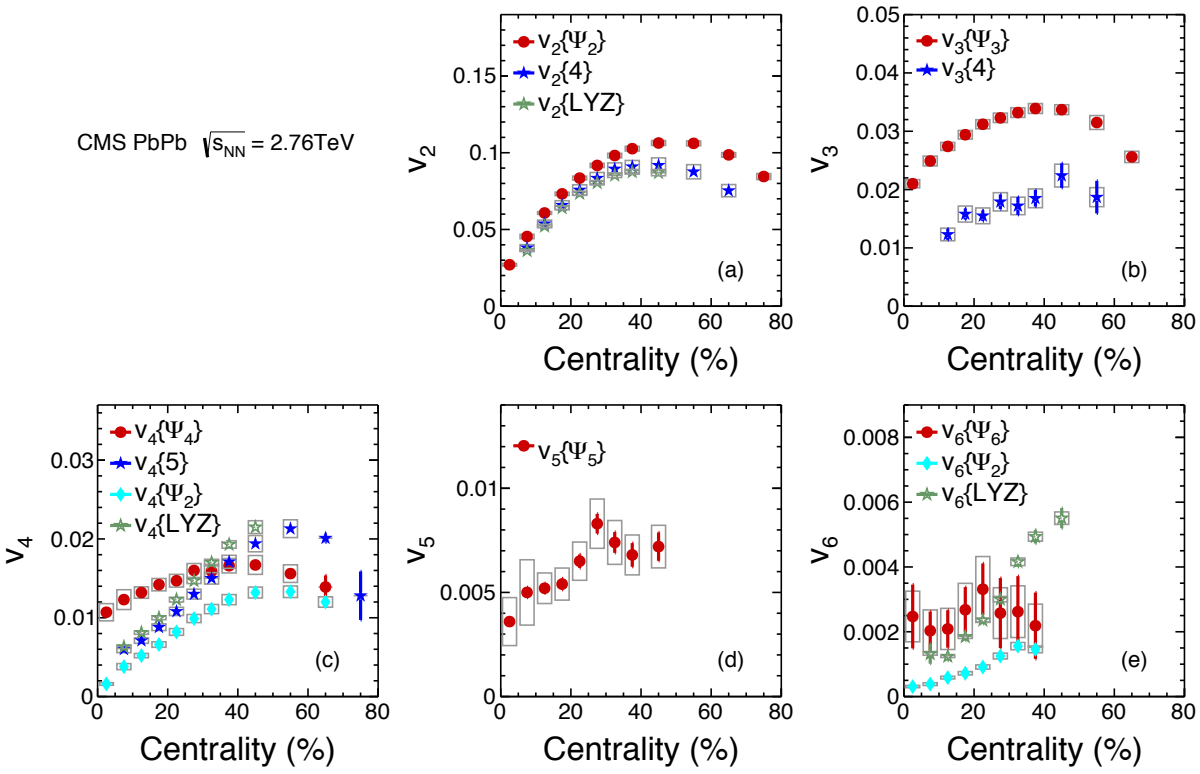

Figure 5.5: Integrated flow coefficients v_n, for n = 2 - 6, with $|\eta| < 0.8$ are shown for different methods as a function of centrality. The v_2 results were published in [104]. Other results were published in [164].

The centrality dependence of the integrated v_n values with $|\eta| < 0.8$ and $0.3 < p_T < 3.0$ GeV/c is shown in Figure 5.5 for the different methods. As noted for the p_T dependent results, a stronger centrality dependence is found for analyses based on the $n = 2$ reference plane, which is more clearly seen in Figure 5.5a.

The pseudorapidity dependence of the flow coefficients provides additional constraints on the system evolution in the longitudinal direction. The measurement of $v_2(\eta)$ is done using all particles in the range $|\eta| < 2.4$ and $0.3 < p_T < 3$ GeV/c in the generating function, to obtain the reference flow, and then extracting the pseudorapidity dependence in small pseudorapidity intervals of $\Delta\eta = 0.4$. Tracking efficiency and fake-rate corrections are applied using a track-by-track weight in forming the differential generating functions. As a crosscheck, we have confirmed that at mid-rapidity the

values obtained with this method agree with the ones obtained from a direct yield-weighted average of the $v_2(p_T)$ results from Figure 5.1, within the stated systematic uncertainties.

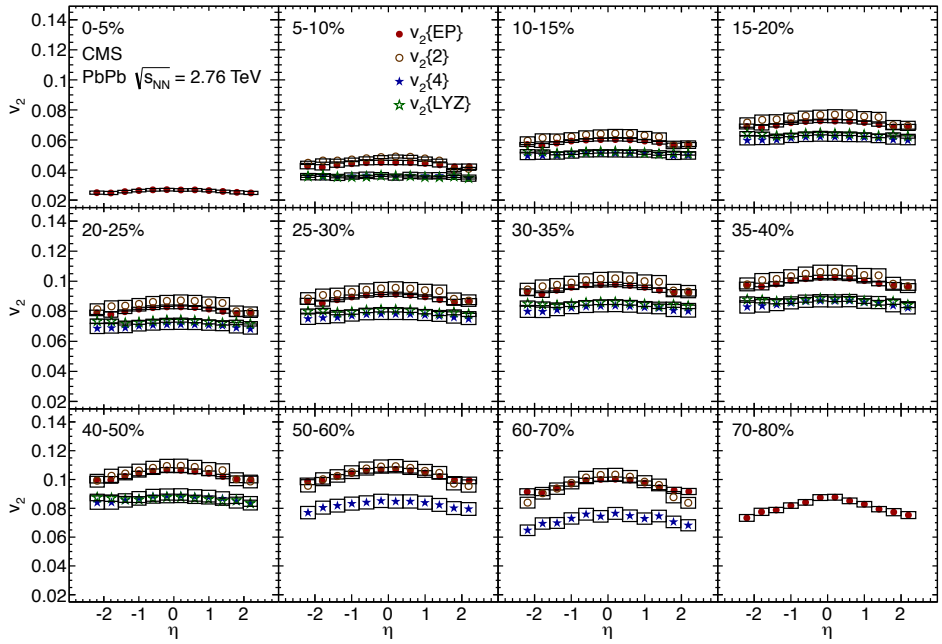

Figure 5.6: Pseudorapidity dependence of v_2 for $0.3 < p_T < 3$ GeV/c with all four methods in 12 centrality classes. The boxes give the systematic uncertainties. The magnitudes of the statistical uncertainties are smaller than the size of the symbols. These results were published in [104].

As observed at mid-rapidity ($|\eta| < 0.8$) in Figure 5.4, the values of $v_2\{4\}$ and $v_2\{LYZ\}$ are in agreement and are smaller than $v_2\{2\}$ and $v_2\{EP\}$. This behavior persists at larger pseudorapidity, as shown in Figure 5.6, which suggests that similar non-flow correlations and eccentricity fluctuations affect the results over the full measured pseudorapidity range. The results show that the value of $v_2(\eta)$ is greatest at mid-rapidity and is constant or decreases very slowly at larger values of $|\eta|$. This behavior is most pronounced in peripheral collisions and for the two-particle cumulant method, which is most affected by non-flow contributions.

5.3 Energy Dependence of the Integrated Elliptic Flow Coefficient v_2

In Figure 5.7, we study the $\sqrt{s_{NN}}$ dependence of the integrated v_2 from mid-central collisions spanning $\sqrt{s_{NN}} = 4.7$ GeV to $\sqrt{s_{NN}} = 2.76$ TeV. We have the $v_2\{LYZ\}$ and $v_2\{EP\}$ in the 20-30% centrality class by extrapolating the $v_2(p_T)$ and the charged-particle spectra down to $p_T = 0$. In the extrapolation it is assumed that $v_2(0) = 0$, and the charged-particle yield is constrained to match the $N_{ch}/d\eta$ values measured by CMS [156]. The low-energy data are from [63, 107, 108, 171–176], as compiled in [107] and tabulated in [172]. The error bars for the low-energy data represent the statistical uncertainties. For the CMS data the error bar is the quadrature sum of the statistical and systematic uncertainties. The integrated v_2 values increase approximately logarithmically with

$\sqrt{s_{NN}}$ over the full energy range, with a 20-30% increase from the highest RHIC energy to that of the LHC. We note that the centrality selections, the collision species, and the methods employed in the integrated v_2 measurements are not identical in all experiments, so the comparison presented in Figure 5.7 is only approximate. A comparison of the p_T dependent v_2 between LHC and RHIC in [104] shows that the $v_2(p_T)$ increase about 5-15% from RHIC to LHC at low p_T, thus the 20-30% increase of integrated v_2 is mostly due to the increase in the mean p_T of the charged-particle spectra.

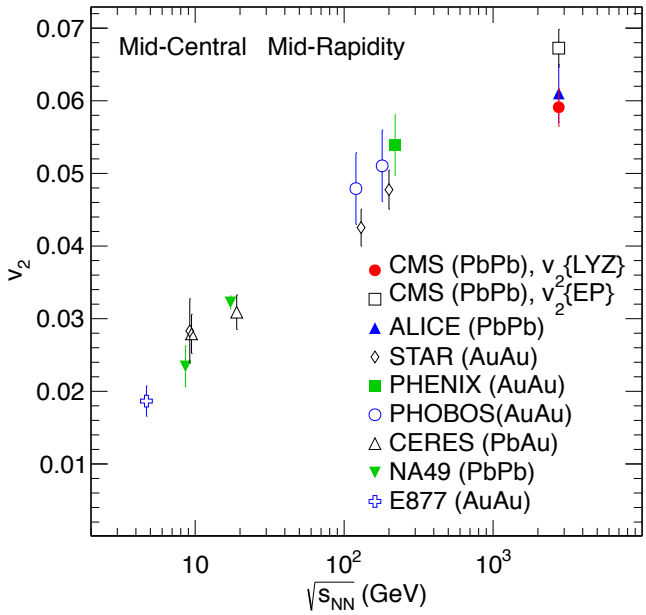

Figure 5.7: The CMS integrated v_2 values for 20-30% centrality from the range $|\eta| < 0.8$ and $0 < p_T < 3$ GeV/c obtained using the event plane method and Lee-Yang Zeros method are compared as a function of $\sqrt{s_{NN}}$ to results at mid-rapidity and similar centrality from ALICE [171], STAR [172], PHENIX [63], PHOBOS [108, 173, 174], NA49 [107], E877 [175], and CERES [176]. The error bars for the lower-energy results represent statistical uncertainties; for the CMS and ALICE measurements the statistical and systematic uncertainties are added in quadrature. The CMS results were published in [104].

Chapter 6

Azimuthal Anisotropy of Charged-Particle Production in High Multiplicity pPb Collisions and Comparison to PbPb Collisions of the Same Multiplicity

The fundamental questions that this thesis is trying to address are whether there is a system size limit for fluid behavior to emerge in heavy ion collisions, and how the azimuthal anisotropies in particle production are influenced by the properties of the medium produced in the collisions and its evolution. In nucleus-nucleus collisions one can vary the system size by selecting collisions of different centrality. In a similar manner, in pPb collisions one could select the collisions based on the number of the produced particles referred to as the multiplicity of the collisions. Although the initial geometry would be very different for a pPb collsions or a PbPb collision that produce the same number of particles in the final state, the event multiplicity is considered as a measure for the initial system size and results from the two collision systems are compared in event-multiplicity classes.

The CMS collaboration has measured the four-particle cumulant $c_2\{4\}$, v_2 from the two- and four-particle correlations and v_3 from the two-particle correlations as a function of multiplicity in pPb and PbPb collisions. The transverse momentum dependence of $v_2\{2, |\Delta\eta| > 2\}$, $v_3\{2, |\Delta\eta| > 2\}$ and $v_2\{4\}$ were also measured. The results were published in [177]. To further explore if the observed two- and four-particle correlations truly signal fluid behavior, another paper is in progress [178] that studies if the values of v_2 change as more and more particle correlations are used, e.g. by measuring v_2 with six-, eight- and all-particle correlations. My contributions to the papers are the measurements of the four-particle cumulant, the elliptic anisotropy from four-particle correlations $v_2\{4\}$ and the Lee-Yang Zeros method $v_2\{LYZ\}$ as a function of multiplicity, and the transverse momentum dependence of $v_2\{4\}$.

6.1 Four-Particle Cumulant

The four-particle cumulant is usually not a variable that we measure and show as a final result. The original idea for looking at $c_2\{4\}$ was to demonstrate the systematic uncertainty from the multiplicity fluctuation effect. However, it was realized, shortly after we looked at the $c_2\{4\}$, that the $c_2\{4\}$ is very important for the understanding of the "turn on" structure of $v_2\{4\}$ at low multiplicity. Hence, we published the $c_2\{4\}$ as a function of multiplicity in our paper.

The Q-cumulant method is already discussed in Chapter 2. The four-particle cumulant we are discussing here is the Eq. 2.43 with n=2.

$$c_2\{4\} = \left\langle\left\langle e^{-2i(\phi_1+\phi_2-\phi_3-\phi_4)}\right\rangle\right\rangle - 2 \times \left\langle\left\langle e^{-2i(\phi_1-\phi_2)}\right\rangle\right\rangle^2 . \tag{6.1}$$

Comparing Equation 2.43 with Equation 2.45, one knows that $c_2\{4\}$ values need to be negative if we require the $v_2\{4\}$ values to be real numbers.

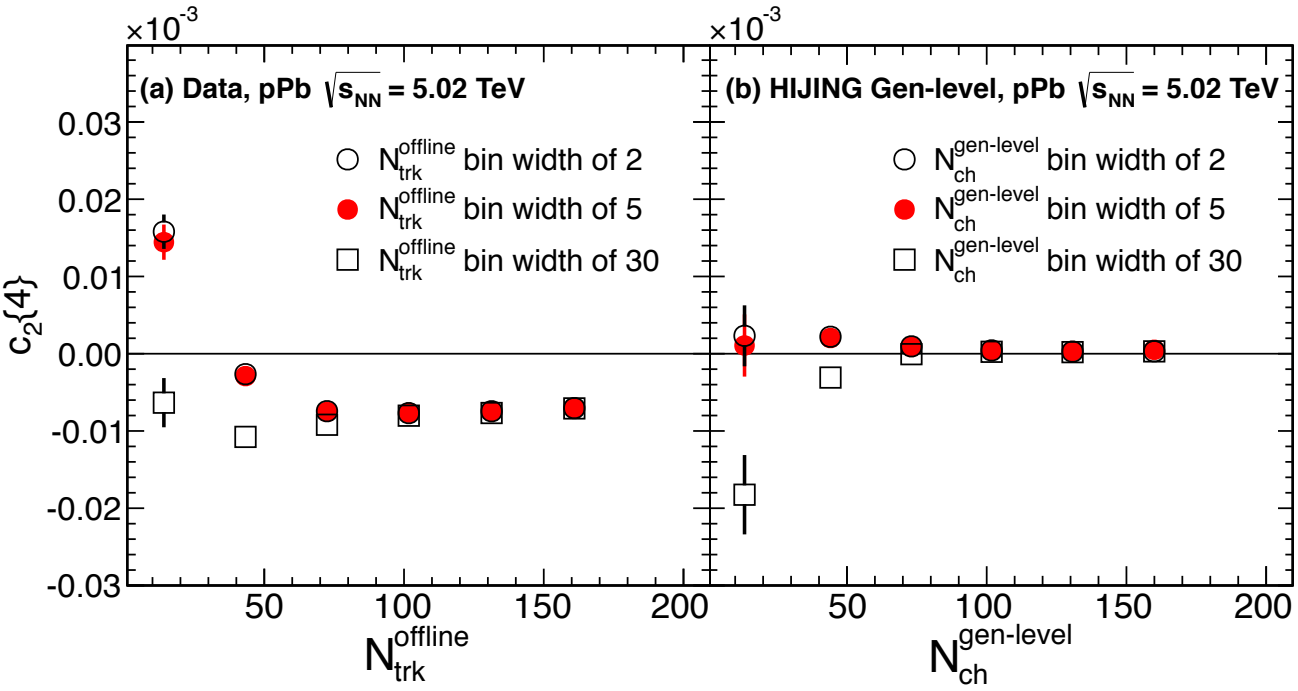

Figure 6.1: The $c_2\{4\}$ values as a function of multiplicity calculated for bin width of 30 (open squares), and first derived using a smaller bin width of 2 (open circles) or 5 (solid circles) and then averaging over the same wider bin of 30, for pPb data (left) and HIJING MC simulations (right) at $\sqrt{s_{NN}}$ = 5.02 TeV. These results were published in [177].

Figure 6.1 (left hand side) shows $c_2\{4\}$ as a function of event multiplicity calculated for bin width of 30 and bin widths of 2 and 5. The $c_2\{4\}$ values from the bin widths of 2 and 5 are averaged to produce a result in bin size of 30 as shown in the figure. We see that the direct calculation of $c_2\{4\}$ values in the large bin size of 30 are different from those obtained using bin sizes of 2 or 5. The $c_2\{4\}$ values from the bin width of 30 are always negative, however the values are positive for small bin widths in low multiplicity events. Obviously, there is a systematic effect that influences the measurement of v_2 for events selected according to their multiplicity, when the width of the multiplicity distribution changes. We can ascertain which result is correct by looking at results in MC with known input $c_2\{4\}$ signal. Figure 6.1 (right hand side) shows the results from HIJING generator-level studies. There is no flow in HIJING, so we expect the $c_2\{4\}$ values to be close to zero at all multiplicities, or at least there should not be a clear negative signal. The plot tells us that the analysis with bin widths of 2 and 5 are correct, however, bin width of 30 is clearly not showing the expected values. This is understood to be due to event-by-event multiplicty fluctuations in the chosen event class which could introduce an artificial $v_2\{4\}$ signal at low multiplicity if large bin width is used. The bin width of 5 is used by default for the study of $v_2\{4\}$.

From the left hand side plot of Figure 6.1, one can see, by looking at the open circles or filled circles, that the values of $c_2\{4\}$ change smoothly from positive to negative at $N_{trk}^{offline}$ around 40, which

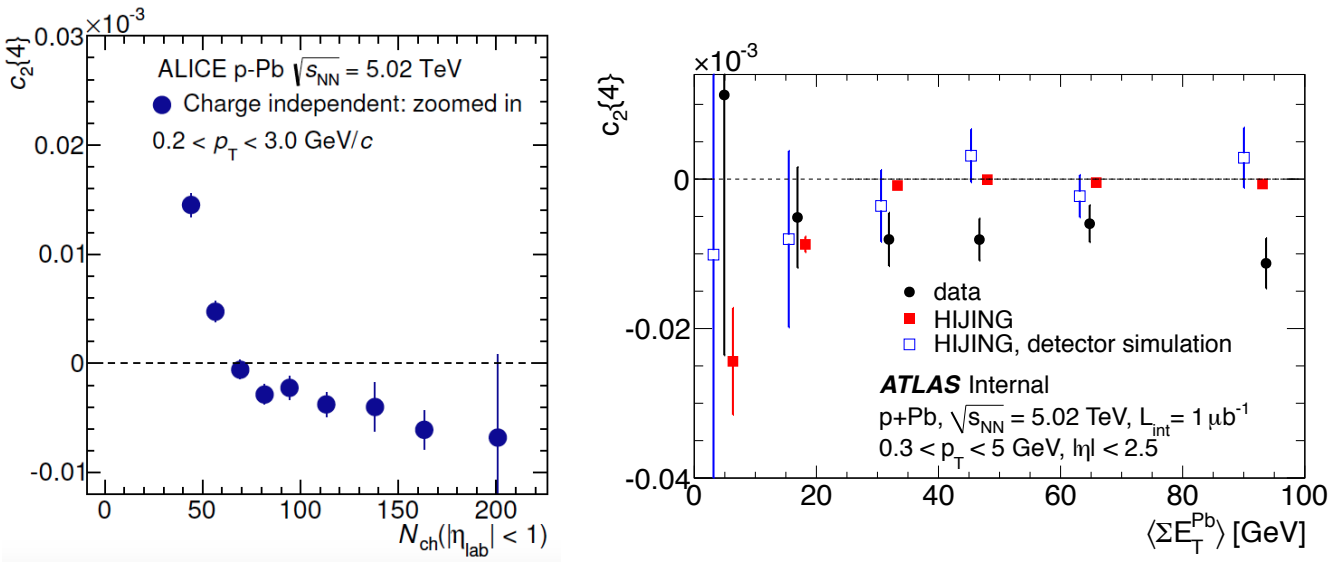

Figure 6.2: Left: Mid-rapidity ($|\eta| < 1$) measurements of $c_2\{4\}$ as a function of multiplicity in pPb collisions [179] . Right: The values of $c_2\{4\}$ as a function of $\Sigma E_{\mathrm{T}}^{\mathrm{Pb}}$ for data, the fully simulated HIJING events and the generator-level HIJING sample [180].

means the $v_2\{4\}$ signal "turns on" at $N_{trk}^{offline}$ around 40. This was the first time that a signature showing the "turn on" of $v_2\{4\}$ was found in pPb collisions.

Recently, similar studies were performed by the ALICE Collaboration [179] as shown in the left hand side of Figure 6.2, which confirm our conclusion. The ATLAS results [180] are shown in the right hand side of Figure 6.2. However, the studies were done as a function of $\Sigma E_{\mathrm{T}}^{\mathrm{Pb}}$, which are likely affected by the multiplicity fluctuation effect, since even in a small bin of $\Sigma E_{\mathrm{T}}^{\mathrm{Pb}}$, the multiplicity fluctuation is large, thus, similar to the results from $N_{trk}^{offline}$ bin width of 30 (open square) in the left hand side of Figure 6.1. ATLAS always got negative values of $c_2\{4\}$ for all the $\Sigma E_{\mathrm{T}}^{\mathrm{Pb}}$ ranges in HIJING.

6.2 Transverse Momentum Dependence of v_2

Long-range correlations in pPb collisions have been predicted in hydrodynamic models [181] where a collective hydrodynamic expansion of the system with fluctuating initial conditions is assumed. To compare with hydrodynamic predictions of the long-range correlations in pPb collisions, v_2 is extracted from a Fourier decomposition of 1D $\Delta\phi$ correlation functions, for the long-range region ($|\Delta\eta| > 2$) as shown in Figure 6.3. To further reduce the residual non-flow correlations, a four-particle cumulant analysis is used to extract the elliptic flow, $v_2\{4\}$, as shown in Figure 6.3. As mentioned in Chapter 2, the multi-particle correlation technique has the advantage of suppressing short-range jet-like correlations compared to two-particle correlations. It thus provides a cleaner measurement of the long-range correlations of collective nature involving many particles from the system. It is also possible to perform a subtraction using low-multiplicity data that are dominated by jet correlations to remove possible non-flow contributions for $v_2\{2, |\Delta\eta| > 2\}$ [177]. Figure 6.3

shows the differential $v_2\{4\}$ and $v_2\{2, |\Delta\eta| > 2\}$ values before and after the low-multiplicity data subtraction in four multiplicity ranges.

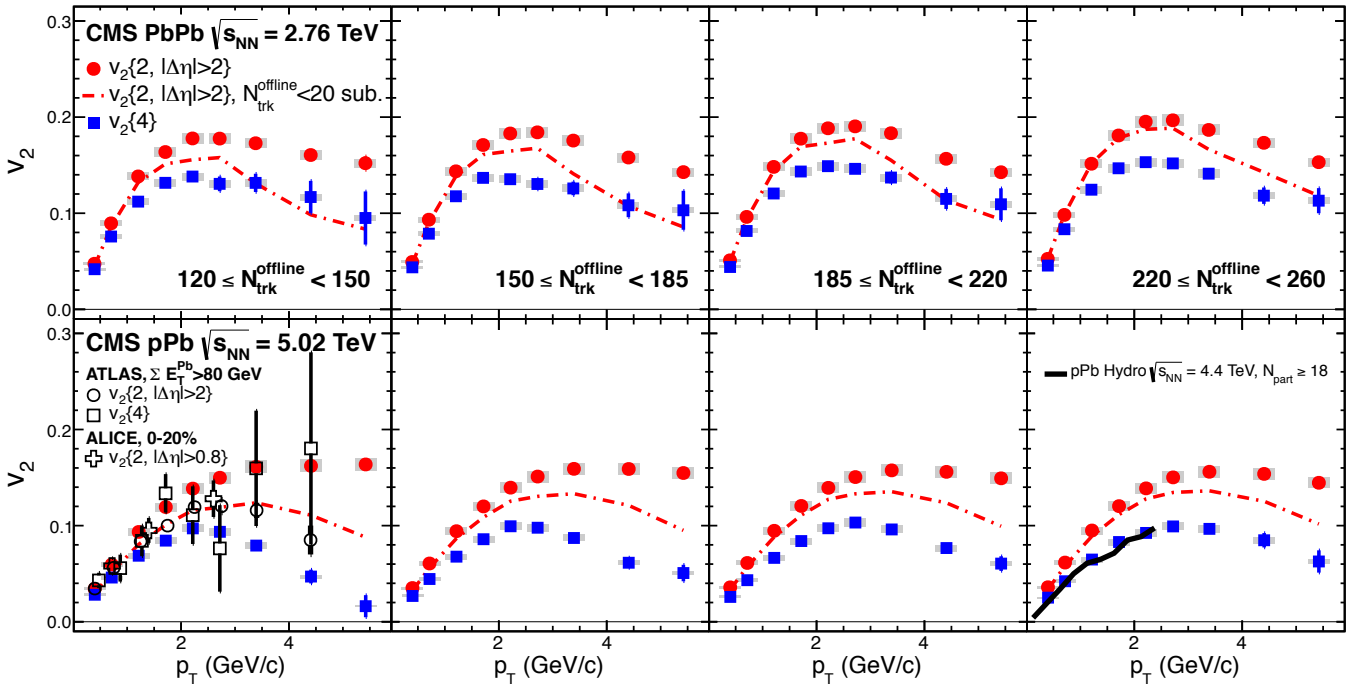

Figure 6.3: The differential $v_2\{2, |\Delta\eta| > 2\}$ and $v_2\{4\}$ values for four multiplicity ranges obtained with $|\eta| < 2.4$ and a p_T^{ref} range of 0.3 - 3 GeV/c. The results are for 2.76 TeV PbPb collisions (top) and for 5.02 TeV pPb collisions (bottom). The error bars correspond to statistical uncertainties, while the shaded areas denote the systematic uncertainties. Results after subtracting the low-multiplicity data ($N_{trk}^{offline} < 20$) as well as predictions from a hydrodynamic model are also shown (curves). The open markers show the results from ALICE [182] and ATLAS [180] using 2012 pPb data. The CMS results were published in [177].

The results from PbPb collisions are shown in the upper panels and those for pPb collisions of the same multiplicity are shown in the lower panels. The magnitude of the v_2 signal is found to be larger in PbPb than in pPb collisions by about 30% for $p_T < 2$ GeV/c. The difference between the $v_2\{2, |\Delta\eta| > 2\}$ and $v_2\{4\}$ results could be, a consequence of event-by-event fluctuations in the flow signal or non-flow correlations, as believed to be the case in PbPb collisions [124]. The p_T dependencies of the v_2 coefficients are similar, with peak values in the 2 - 3 GeV/c range for PbPb, and slightly higher for pPb collisions. The v_2 predicted by the hydrodynamic calculations in [181] for pPb collisions at $\sqrt{s_{NN}} = 4.4$ TeV and for $p_T < 2.5$ GeV/c are shown, and compared to the high-multiplicity pPb data in Figure 6.3. The calculations have little collision energy dependence, and assume the number of participating nucleons to be larger or equal to 18, approximately corresponding to the top 4% of central pPb events. However, contributions from event-by-event fluctuations of the flow signal around its average value are not accounted for in the calculations. Therefore, the v_2 calculated in [181] is expected to lie between the values from the two- and four-particle correlation methods as discussed in Section 2.3.

6.3 Multiplicity Dependence of v_2

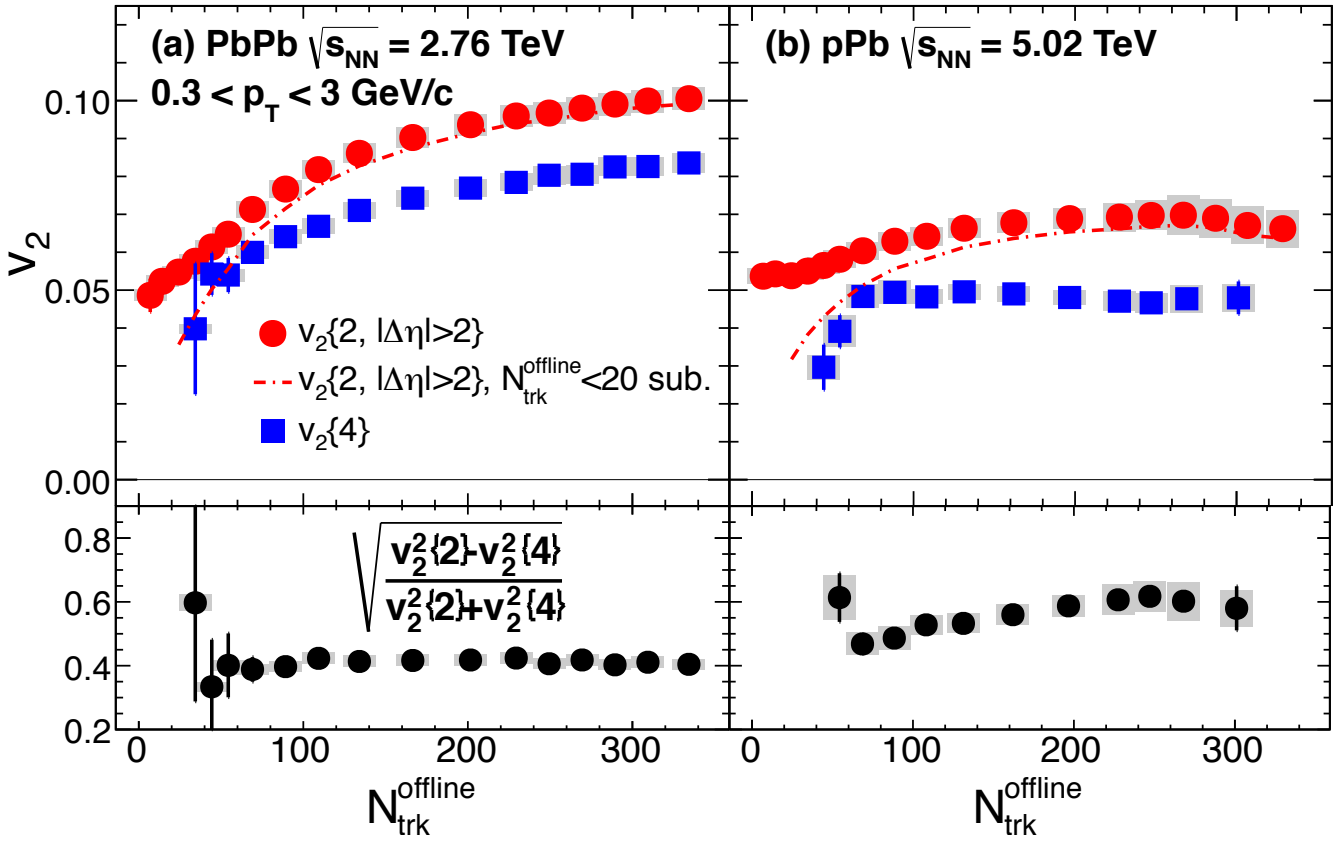

Figure 6.4: Top: the $v_2\{2, |\Delta\eta| > 2\}$ (circles) and $v_2\{4\}$ (squares) values as a function of $N_{trk}^{offline}$ for $0.3 < pT < 3$ GeV/c, in 2.76 TeV PbPb collisions (left) and 5.02 TeV pPb collisions (right). Bottom: upper limits on the relative v_2 fluctuations estimated from $v_2\{2\}$ and $v_2\{4\}$ in 2.76 TeV PbPb collisions (left) and 5.02 TeV pPb collisions (right). The error bars correspond to statistical uncertainties, while the shaded areas denote the systematic uncertainties. Results after subtracting the low-multiplicity data ($N_{trk}^{offline} < 20$) are also shown (curves). These results were published in [177].

The multiplicity dependencies of v_2 for PbPb and pPb collisions, averaged over the p_T range from 0.3 to 3 GeV/c, are shown in Figure 6.4. The $v_2\{2, |\Delta\eta| > 2\}$ and $v_2\{4\}$ values in PbPb collisions exhibit a moderate increase with $N_{trk}^{offline}$, while these coefficients remain relatively constant as a function of multiplicity for pPb data at larger values of $N_{trk}^{offline}$. Similarly to Figure 6.3, the PbPb data show a larger v_2 signal than observed for the pPb data over a wide multiplicity range. Below an $N_{trk}^{offline}$ value of 40, $v_2\{4\}$ can not be reliably extracted as we could already see from the four-particle cumulant results.

The magnitude of event-by-event v_2 fluctuations is estimated from the difference in the $v_2\{2, |\Delta\eta| > 2\}$ and $v_2\{4\}$ results. If hydrodynamic flow is the dominant source of the correlations, the relative v_2 fluctuations can be approximated by $\sqrt{(v_2^2\{2\} - v_2^2\{4\})/(v_2^2\{2\} + v_2^2\{4\})}$ as discussed in Section 2.3. The resulting flow fluctuation values calculated for pPb and PbPb collisions are shown in the bottom

two panels of Figure 6.4, with 40% v_2 fluctuations observed in PbPb and 50 - 60% fluctuations in pPb collisions. This magnitude of v_2 fluctuations in 2.76 TeV PbPb collisions at the LHC is comparable to the value measured in 200 GeV AuAu collisions at RHIC [183]. As a consequence of possible residual non-flow correlations from back-to-back jets in the $v_2\{2, |\Delta\eta| > 2\}$ measurement, these results should be considered as upper limits on the flow fluctuations.

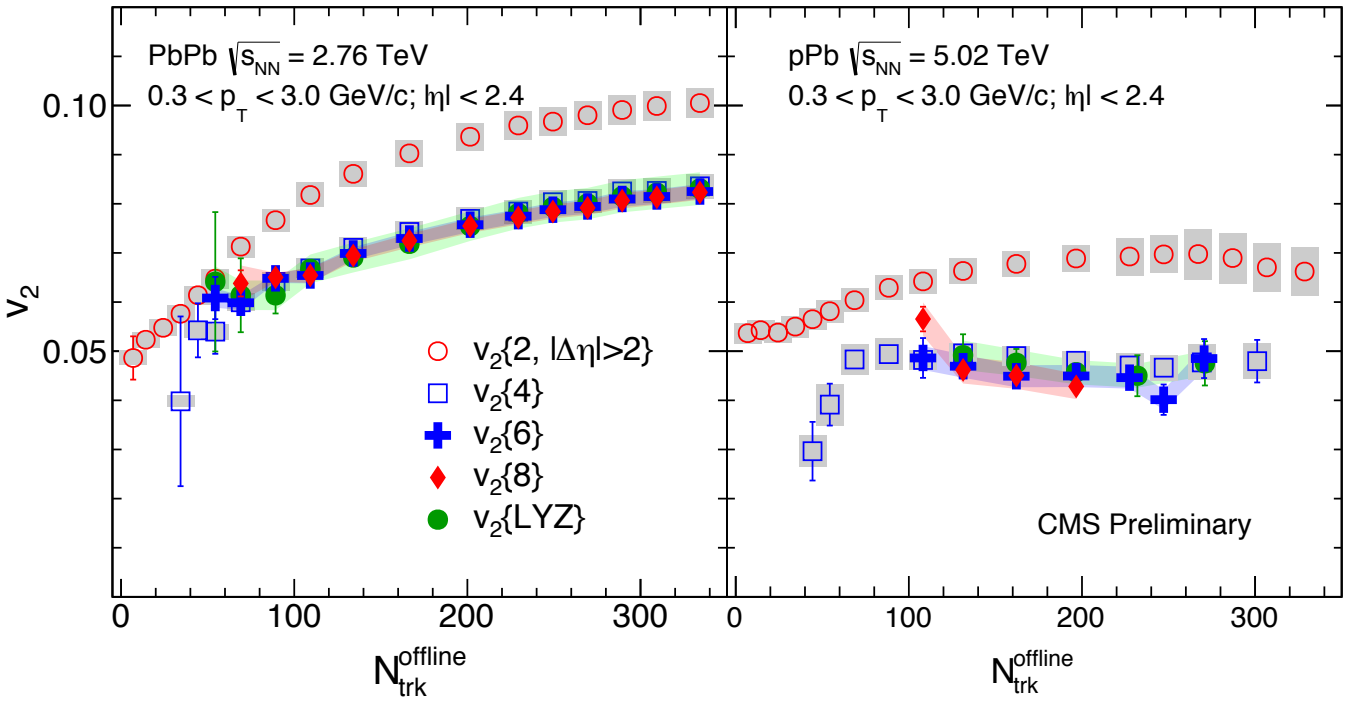

Figure 6.5: The v_2 results obtained from six-particle (blue cross), eight-particle (red diamond) cumulants, and LYZ (green filled circle) method, averaged over the particle p_T range of 0.3–3.0 GeV/c, as a function of $N_{trk}^{offline}$ in PbPb at $\sqrt{s_{NN}}$ = 2.76 TeV (left) and pPb at $\sqrt{s_{NN}}$ = 5.02 TeV (right). The two-particle and four-particle correlation v_2 results (open data points) are shown for comparison. Shaded areas denote systematic uncertainties. The new results are to be published [178].

The $v_2\{4\}$ results in pPb collisions were met with great interest both in the heavy ion community and in the general public, since they signaled a possible fluid behavior in very small systems and the emergence of this behavior at a given system size. However, one could ask if there is still some non-flow in four-particle correlations. The true fluid behavior is multiparticle in nature so it is desirable to study these correlations with more than four particles in order to establish whether the v_2 in pPb collisions is collective flow that can be described by models like hydrodynamics. If the results from six-, eight- and more-particle correlations are decreasing and become smaller as more particles are correlated, the $v_2\{4\}$ results might not be flow and might not have much interest for us. Thus, it is very important to study v_2 in pPb collisions with more than four-particle correlations.

Figure 6.5 shows the v_2 results obtained from six-particle, eight-particle cumulants, and LYZ method with all-particle correlations, averaged over the particle p_T range of 0.3–3.0 GeV/c, as a function of $N_{trk}^{offline}$ in PbPb collisions at $\sqrt{s_{NN}}$ = 2.76 TeV (left) and pPb collisions at $\sqrt{s_{NN}}$ = 5.02 TeV

(right). The two-particle and four-particle correlation v_2 results (open data points) are shown for comparison. For both PbPb and pPb systems, v_2 results from four-($v_2\{4\}$), six-($v_2\{6\}$) and eight-($v_2\{8\}$) particle cumulants, and the LYZ method ($v_2\{LYZ\}$) are in agreement within $\pm 10\%$ over almost the entire multiplicity range. The results confirm that the observed correlations in both systems have collective nature. In PbPb collisions, v_2 from all methods show an increase with multiplicity, while little multiplicity dependence is observed for the pPb collisions. This difference might reflect the presence of a lenticular overlap geometry in PbPb collisions that is absent in pPb collisions.

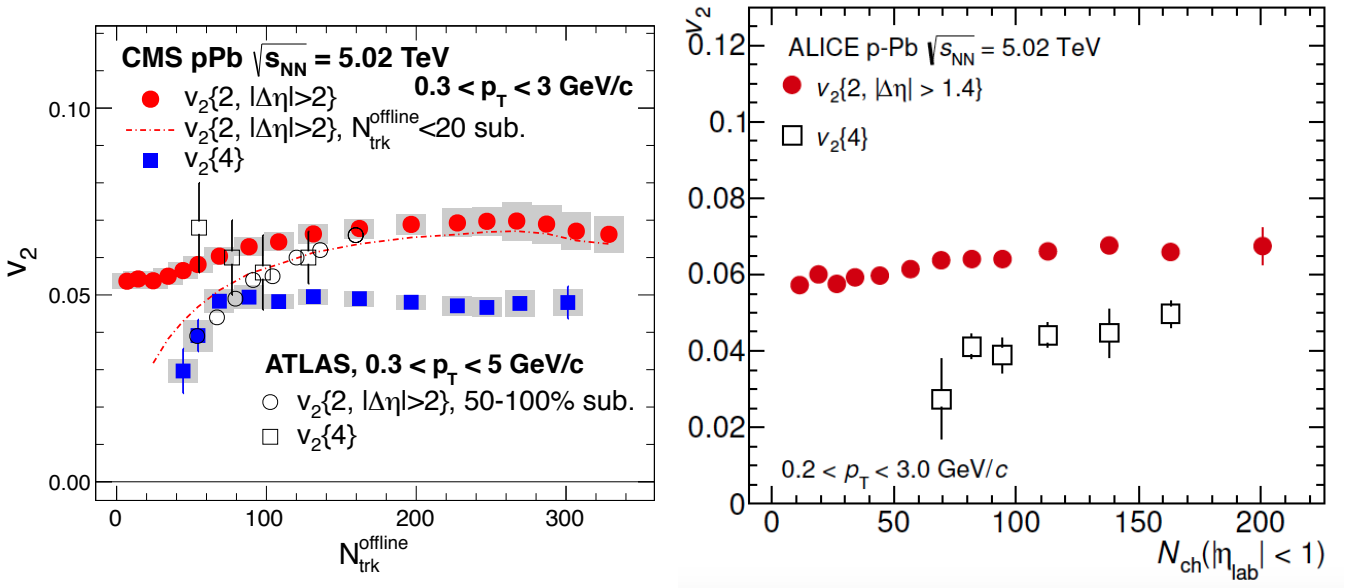

Figure 6.6: Left: The $v_2\{2, |\Delta\eta| > 2\}$ and $v_2\{4\}$ values as a function of $N_{trk}^{offline}$ for $0.3 < p_T < 3$ GeV/c, measured by CMS in 5.02 TeV pPb collisions (filled). The dash-dotted curve shows the CMS $v_2\{2, |\Delta\eta| > 2\}$ values after subtracting the 70 - 100% lowest-multiplicity data, to be compared with the ATLAS results subtracted by 50-100% lowest-multiplicity data (open) [180]. The error bars correspond to statistical uncertainties, while the shaded areas denote the systematic uncertainties. Right: Mid-rapidity ($|\eta| < 1$) measurements of $c_2\{4\}$ as a function of multiplicity in pPb collisions from ALICE Collaboration [179].

The left hand side of Figure 6.6 shows the comparison of $v_2\{2, |\Delta\eta| > 2\}$ and $v_2\{4\}$ results as a function of multiplicity from CMS, averaged over $0.3 < p_T < 3$ GeV/c, with those obtained by the ATLAS experiment, averaged over $0.3 < p_T < 5$ GeV/c with the data from the 2012 pPb run. The ATLAS $v_2\{2, |\Delta\eta| > 2\}$ values have the contribution from the 50 - 100% lowest multiplicity data subtracted, while the corresponding CMS data, shown as a curve in Figure 6.6 (left), use the 70 - 100% lowest multiplicity events for the subtraction. The difference in the low-multiplicity events used for the subtraction could explain the slight discrepancy in the resulting $v_2\{2, |\Delta\eta| > 2\}$ data from the two experiments. The $v_2\{4\}$ values from ATLAS are systematically higher than the CMS data. This may be accounted for by the multiplicity fluctuation effect discussed previously, although the discrepancy is not large with respect to the uncertainties. The right hand side of Figure 6.6 shows the results of $v_2\{2, |\Delta\eta| > 1.4\}$ and $v_2\{4\}$ as a function of multiplicity N_{ch}, as defined by the ALICE tracking-efficiency-corrected charged-particle multiplicity, with $0.2 < p_T < 3$ GeV/c and

$|\eta| < 1$. The p_T range for ALICE starts from 0.2 GeV/c, thus, the ALICE results are expected to be smaller than those of CMS and ATLAS, which is indeed the case from the comparison.

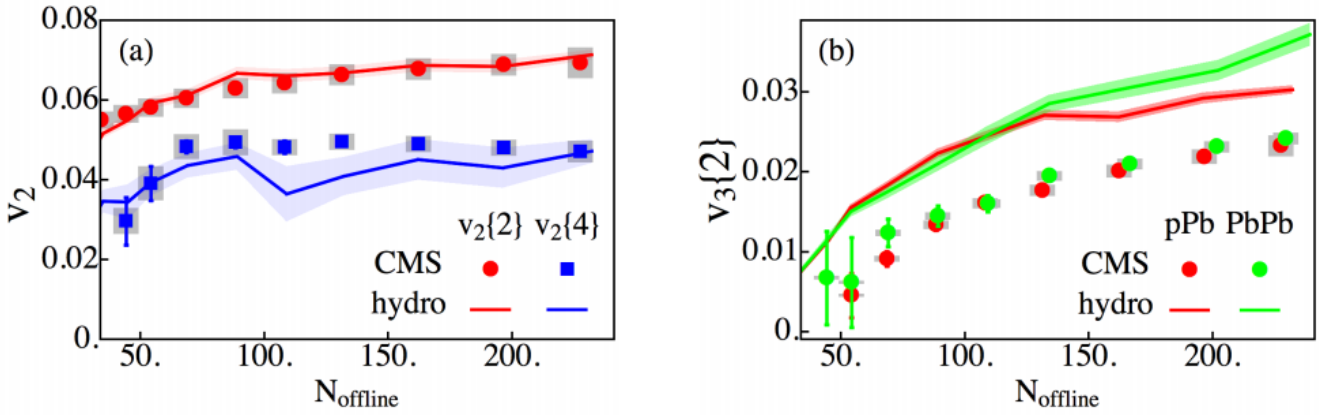

Figure 6.7: The comparison of v_2 (left) in pPb and v_3 (right) in pPb and PbPb between data and a viscous hydrodynamic calculation [184]. The initial condion is calculated using the MC Glauber model. The value of η/s in the calculation is 0.08.

After we released our results in 2013, a lot of theoretical studies have ensued [184–195]. The results of v_2 as a function of p_T in Figure 6.3 are already compared to a viscous hydrodynamic calculation, which uses the MC Glauber initial conditions and takes the value of $\eta/s = 0.08$ in the QGP phase.

Figure 6.7 from [184] shows the comparison of v_2 (left) in pPb and v_3 (right) in pPb and PbPb between data and another viscous hydrodynamic calculation. The initial condion is also calculated using the MC Glauber model. The value of η/s in the calculation is 0.08. There is a good agreement between the data and the calculation for both $v_2\{2\}$ and $v_2\{4\}$ in pPb collisions. However, the results from the calculation are larger than data for $v_3\{2\}$ in both pPb and PbPb collisions as seen in the right hand side plot of Figure 6.7.

The calculations in Figure 6.8 (left) are from [189] and similar to those in Figure 6.7. They compare the values of $v_2\{4\}$ from data and the viscous hydrodynamic calculation with MC Glauber model as initial conditons. Different values of η/s are studied. One can see that the calculations for $\eta/s = 0.08$ agree with the results from data best.

The right hand side of Figure 6.8 shows the comparison of the root-mean-square v_2 (the same as our $v_2\{2, |\Delta\eta| > 2\}$) between data and a hydrodynamic calculation with IP-Glasma as initial condition model [185]. The value of η/s is 0.18 in the calculation. The IP-Glasma + hydrodynamic model works well for PbPb collisions but clearly fails to get the value of v_2 in pPb collisions. The paper mentioned that they have checked the ideal case with $\eta/s = 0$, but the calculation results still underestimate the data by approximately a factor of 2.

Overall, there is not a model that can produce all the features in the data so far. It is clear that all the models favor a low value of $\eta/s < 0.24$, similar to the conclusion in AuAu and PbPb collisions. The calculations taking the MC Glauber model as the initial conditions agree with data better. But it was found that there are large uncertainties in the calculations of initial spatial asymmetry

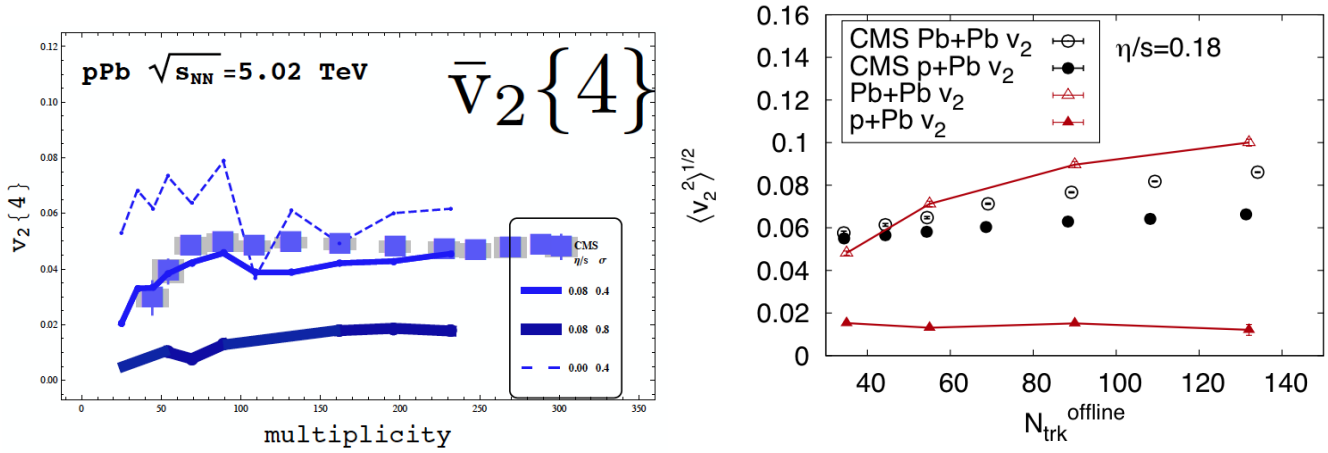

Figure 6.8: Left: The values of $v_2\{4\}$ from data compared to a viscous hydrodynamic calculation with MC Glauber model as initial conditons [189]. Different blue curves show results from different input η/s. Right: Multiplicity dependence of the root-mean-square v_2 in PbPb and pPb collisions from the IP-Glasma + hydrodynamic model [185] compared to our data. The value of η/s is 0.18 in the hydrodynamic calculation.

ϵ_n in pPb collisions [196]. The calculations with IP-Glasma initial conditions fail to reproduce the data because the ϵ_n are too small in the model [185]. The initial shape of a pPb collision follows the shape of the proton, which is spherical in the IP-Glasma model. Thus our data with large v_2 in pPb collisions suggests that the shape of proton might be eccentric, if the hydrodynamic paradigm is valid. It is surprising that our results could be used to extract detailed information on the spatial gluon distribution in the proton.

Chapter 7

Conclusion

Detailed measurements of the charged-particle azimuthal anisotropies in $\sqrt{s_{NN}} = 2.76$ TeV PbPb collisions and $\sqrt{s_{NN}} = 5.02$ TeV pPb collisions have been presented with multiparticle correlations (Lee-Yang Zeros method) and compared to the anisotropies obtained with event-plane, two- and four-particle correlation methods. Due to the different sensitivities to non-flow correlations and initial state fluctuations, these comparisons provide constraints to models describing the earliest stages of the heavy ion collisions, and facilitate the precise extraction of the transport properties, such as shear viscosity over entropy density, of the quark gluon plasma. The PbPb results are shown in 8 centrality classes from 5 to 50% and cover a broad kinematic range of $0.3 < p_T < 20$ GeV/c and $|\eta| < 2.4$. To explore the system size dependence of the collective flow, four-particle correlations are used to study $v_2(p_T)$ in peripheral PbPb collisions and in high-multiplicity pPb collisions. Further, the integrated v_2 in pPb collisions for charged particles in the range of $0.3 < p_T < 6$ GeV/c and $|\eta| < 2.4$, from four- and all-particle correlations are compared to PbPb results in the same particle multiplicity ranges.

The shapes of the $v_n(p_T)$ distributions in both PbPb and pPb are found to be similar to those measured in AuAu collisions at RHIC. The integrated v_2 signal increases from the most central PbPb collisions to the 40–50% centrality range, after which a decrease is observed. The rise is understood in terms of the increase of ϵ_2 and the fall may be due to incomplete thermalization, e.g. - the system does not transform the initial-state geometric anisotropy into a final-state momentum anisotropy so efficiently. The value of $v_2(\eta)$ is found to be weakly dependent on pseudorapidity in central collisions, which indicate approximate boost invariance in central events. However, for peripheral collisions, the values of $v_2(\eta)$ gradually decrease as the pseudorapidity increases, which signals inhomogeneity in the smaller systems. The change in the $\langle p_T \rangle$ value can also cause the decrease. The integrated v_2 at mid-rapidity and in mid-central collisions (20–30% centrality) increases approximately logarithmically with $\sqrt{s_{NN}}$. An increase in the v_2 signal by 20–30% from the highest RHIC energy to that of the LHC is observed. The increase is mostly due to the increase in the mean p_T of the underlying charged-particle spectra.

A significant centrality dependence is observed for v_n that is based on a second-order reference distribution. However, a weak centrality dependence is found for v_n that is based on higher-order reference distribution, which indicates that the the higher-order flow coefficients indeed originate from initial state fluctuations. Further theoretical studies are needed to fully explain the method-dependent differences of v_n seen in the data. These differences can be attributed to the role of fluctuations in the participant geometry. Understanding the role of these fluctuations is necessary in order to establish the initial state of the created medium, thereby allowing for an improved determination of its properties.

The four-particle cumulant as a function particle multiplicity in pPb collisions shows a smooth change of sign at $N_{trk}^{offline}$ around 40, which indicates the "turn on" of four-particle correlations

as the volume of the produced system increases. Going back to the question asked in Section 1.4 about "What is the smallest system size in which equilibration and subsequent collective flow can be achieved?", we could answer that for $\sqrt{s_{NN}} = 5.02$ TeV pPb collisions, at least 40 particles are needed in order to observe four-particle correlations. This is a discovery based on the studies from this thesis. We could not directly address the question of whether or not the system is thermally equilibrated. However, we sought to understand whether the correlations in small systems are limited to a small number of particles or if they are a true collective phenomenon. The correlations of all particles produced in the collisions were explored using the Lee-Yang Zeros method. The elliptic anisotropy measurements $v_2\{LYZ\}$ were compared to the results from four-, six- or eight-particle correlations and were found to be in agreement within 10% both in pPb collisions and in peripheral PbPb collisions. This is the most important discovery of the studies in the thesis. It indicates that all the particles are correlated and there is collective flow in high-multiplicity pPb collisions. Whether or not the flow is hydrodynamic in nature is beyond the scope of the thesis, but if it is, we may have created the smallest drops of liquid ever made in the laboratory [197].

Bibliography

[1] T. D. Lee and G. C. Wick, "Vacuum stability and vacuum excitation in a spin-0 field theory," *Phys. Rev. D* **9** (Apr, 1974) 2291–2316. http://link.aps.org/doi/10.1103/PhysRevD.9.2291.

[2] J. C. Collins and M. J. Perry, "Superdense matter: Neutrons or asymptotically free quarks?," *Phys. Rev. Lett.* **34** (May, 1975) 1353–1356. http://link.aps.org/doi/10.1103/PhysRevLett.34.1353.

[3] E. V. Shuryak, "Quantum chromodynamics and the theory of superdense matter," *Physics Reports* **61** (1980) 71 – 158.

[4] D. J. Gross and F. Wilczek, "Ultraviolet Behavior of Nonabelian Gauge Theories," *Phys. Rev. Lett.* **30** (1973) 1343–1346.

[5] F. Karsch, "Lattice results on QCD thermodynamics," *Nucl. Phys.* **A698** (2002) 199–208, arXiv:hep-ph/0103314 [hep-ph].

[6] M. Alford et al., "Color superconductivity in dense quark matter," *Rev. Mod. Phys.* **80** (2008) 1455–1515, arXiv:0709.4635 [hep-ph].

[7] D. Page and S. Reddy, "Dense Matter in Compact Stars: Theoretical Developments and Observational Constraints," *Ann. Rev. Nucl. Part. Sci.* **56** (2006) 327–374, arXiv:astro-ph/0608360 [astro-ph].

[8] Z. Fodor, S. Katz, and K. Szabo, "The QCD equation of state at nonzero densities: Lattice result," *Phys. Lett.* **B568** (2003) 73–77, arXiv:hep-lat/0208078 [hep-lat].

[9] C. Allton, S. Ejiri, S. Hands, O. Kaczmarek, F. Karsch, *et al.*, "The Equation of state for two flavor QCD at nonzero chemical potential," *Phys. Rev.* **D68** (2003) 014507, arXiv:hep-lat/0305007 [hep-lat].

[10] J. Wambach, K. Heckmann, and M. Buballa, "Transport Properties of Strong-Interaction Matter," *AIP Conf. Proc.* **1441** (2012) 794–796, arXiv:1111.5475 [hep-ph].

[11] **Nuclear Science Advisory Committee (NSAC)**, "The Frontiers of Nuclear Science - A Long Range Plan,".

[12] A. Andronic, P. Braun-Munzinger, and J. Stachel, "The Horn, the hadron mass spectrum and the QCD phase diagram: The Statistical model of hadron production in central nucleus-nucleus collisions," *Nucl. Phys.* **A834** (2010) 237C–240C, arXiv:0911.4931 [nucl-th].

[13] A. Kalweit, "QCD Phase Diagram, Fluctuations, Thermodynamics and Hadron Chemistry, QM14, Student Day,".

[14] **STAR Collaboration**, J. Adams *et al.*, "Experimental and theoretical challenges in the search for the quark gluon plasma: The STAR Collaboration's critical assessment of the

evidence from RHIC collisions," *Nucl. Phys.* **A757** (2005) 102–183, arXiv:nucl-ex/0501009 [nucl-ex].

[15] H. Gutbrod et al., "Plastic ball experiments," *Rep. Prog. Phys.* **52** (1989) 1267. http://stacks.iop.org/0034-4885/52/i=10/a=003.

[16] U. Heinz and M. Jacob, "Evidence for a new state of matter: An assessment of the results from the CERN lead beam programme," 2000. arXiv:nucl-th/0002042 (http://arxiv.org/abs/nucl-th/0002042).

[17] **BRAHMS Collaboration**, I. Arsene *et al.*, "Quark gluon plasma and color glass condensate at RHIC? The Perspective from the BRAHMS experiment," *Nucl. Phys.* **A757** (2005) 1–27, arXiv:nucl-ex/0410020 [nucl-ex].

[18] **PHENIX Collaboration**, K. Adcox *et al.*, "Formation of dense partonic matter in relativistic nucleus-nucleus collisions at RHIC: Experimental evaluation by the PHENIX collaboration," *Nucl. Phys.* **A757** (2005) 184–283, arXiv:nucl-ex/0410003 [nucl-ex].

[19] B. Back, M. Baker, M. Ballintijn, D. Barton, B. Becker, *et al.*, "The PHOBOS perspective on discoveries at RHIC," *Nucl. Phys.* **A757** (2005) 28–101, arXiv:nucl-ex/0410022 [nucl-ex].

[20] U. W. Heinz and M. Jacob, "Evidence for a new state of matter: An Assessment of the results from the CERN lead beam program," arXiv:nucl-th/0002042 [nucl-th].

[21] P. Jacobs and X.-N. Wang, "Matter in extremis: Ultrarelativistic nuclear collisions at RHIC," *Prog. Part. Nucl. Phys.* **54** (2005) 443–534, arXiv:hep-ph/0405125 [hep-ph].

[22] M. Gyulassy, "The qgp discovered at rhic," in *Structure and Dynamics of Elementary Matter*, W. Greiner, M. Itkis, J. Reinhardt, and M. Güçlü, eds., vol. 166 of *NATO Science Series*, pp. 159–182. Springer Netherlands, 2004. http://dx.doi.org/10.1007/978-1-4020-2705-5_14.

[23] M. Gyulassy and L. McLerran, "New forms of QCD matter discovered at RHIC," *Nucl. Phys.* **A750** (2005) 30–63, arXiv:nucl-th/0405013 [nucl-th].

[24] E. V. Shuryak, "What RHIC experiments and theory tell us about properties of quark-gluon plasma?," *Nucl. Phys.* **A750** (2005) 64–83, arXiv:hep-ph/0405066 [hep-ph].

[25] B. Muller and J. L. Nagle, "Results from the relativistic heavy ion collider," *Ann. Rev. Nucl. Part. Sci.* **56** (2006) 93–135, arXiv:nucl-th/0602029 [nucl-th].

[26] S. Bass, "http://qgp.phy.duke.edu,".

[27] T. Hirano, N. van der Kolk, and A. Bilandzic, "Hydrodynamics and Flow," *Lect. Notes Phys.* **785** (2010) 139–178, arXiv:0808.2684 [nucl-th].

[28] L. D. McLerran and R. Venugopalan, "Computing quark and gluon distribution functions for very large nuclei," *Phys. Rev.* **D49** (1994) 2233–2241, arXiv:hep-ph/9309289 [hep-ph].

[29] L. D. McLerran and R. Venugopalan, "Gluon distribution functions for very large nuclei at small transverse momentum," *Phys. Rev.* **D49** (1994) 3352–3355, arXiv:hep-ph/9311205 [hep-ph].

[30] E. Iancu and R. Venugopalan, "The Color glass condensate and high-energy scattering in QCD," arXiv:hep-ph/0303204 [hep-ph].

[31] F. Gelis, E. Iancu, J. Jalilian-Marian, and R. Venugopalan, "The Color Glass Condensate," *Ann. Rev. Nucl. Part. Sci.* **60** (2010) 463–489, arXiv:1002.0333 [hep-ph].

[32] T. Lappi and L. McLerran, "Some features of the glasma," *Nucl. Phys.* **A772** (2006) 200–212, arXiv:hep-ph/0602189 [hep-ph].

[33] H. Fujii, F. Gelis, A. Stasto, and R. Venugopalan, "Melting the color glass condensate at the LHC," arXiv:0707.1870 [nucl-th].

[34] R. Venugopalan, "From Glasma to Quark Gluon Plasma in heavy ion collisions," *J. Phys.* **G35** (2008) 104003, arXiv:0806.1356 [hep-ph].

[35] F. Gelis, "Color Glass Condensate and Glasma," *Int. J. Mod. Phys.* **A28** (2013) 1330001, arXiv:1211.3327 [hep-ph].

[36] R. Clare and D. Strottman, "Relativistic Hydrodynamics and heavy ion reactions," *Phys. Rept.* **141** (1986) 177–280.

[37] P. Huovinen, "Hydrodynamical description of collective flow. Chapter 1.," arXiv:nucl-th/0305064 [nucl-th].

[38] P. F. Kolb and U. W. Heinz, "Hydrodynamic description of ultrarelativistic heavy ion collisions," arXiv:nucl-th/0305084 [nucl-th].

[39] U. W. Heinz, "Early collective expansion: Relativistic hydrodynamics and the transport properties of QCD matter," arXiv:0901.4355 [nucl-th].

[40] D. A. Teaney, "Viscous Hydrodynamics and the Quark Gluon Plasma," arXiv:0905.2433 [nucl-th].

[41] H. Sorge, H. Stoecker, and W. Greiner, "Poincare Invariant Hamiltonian Dynamics: Modeling Multi - Hadronic Interactions in a Phase Space Approach," *Annals Phys.* **192** (1989) 266–306.

[42] S. Bass, M. Belkacem, M. Bleicher, M. Brandstetter, L. Bravina, *et al.*, "Microscopic models for ultrarelativistic heavy ion collisions," *Prog. Part. Nucl. Phys.* **41** (1998) 255–369, arXiv:nucl-th/9803035 [nucl-th].

[43] M. Bleicher, E. Zabrodin, C. Spieles, S. Bass, C. Ernst, *et al.*, "Relativistic hadron hadron collisions in the ultrarelativistic quantum molecular dynamics model," *J. Phys.* **G25** (1999) 1859–1896, arXiv:hep-ph/9909407 [hep-ph].

[44] J. Rafelski and B. Müller, "Strangeness production in the quark-gluon plasma," *Phys. Rev. Lett.* **48** (Apr, 1982) 1066–1069. http://link.aps.org/doi/10.1103/PhysRevLett.48.1066.

[45] J. Sollfrank and U. W. Heinz, "The Role of strangeness in ultrarelativistic nuclear collisions," arXiv:nucl-th/9505004 [nucl-th].

[46] T. Matsui and H. Satz, "J/ψ Suppression by Quark-Gluon Plasma Formation," *Phys. Lett.* **B178** (1986) 416.

[47] L. Kluberg and H. Satz, "Color Deconfinement and Charmonium Production in Nuclear Collisions," arXiv:0901.3831 [hep-ph].

[48] X.-N. Wang and M. Gyulassy, "Gluon shadowing and jet quenching in A+A collisions at $\sqrt{s_{NN}} = 200$ GeV," *Phys. Rev. Lett.* **68** (Mar, 1992) 1480–1483. http://link.aps.org/doi/10.1103/PhysRevLett.68.1480.

[49] X.-N. Wang, Z. Huang, and I. Sarcevic, "Jet quenching in the opposite direction of a tagged photon in high-energy heavy ion collisions," *Phys. Rev. Lett.* **77** (1996) 231–234, arXiv:hep-ph/9605213 [hep-ph].

[50] M. Gyulassy, I. Vitev, X.-N. Wang, and B.-W. Zhang, "Jet quenching and radiative energy loss in dense nuclear matter," arXiv:nucl-th/0302077 [nucl-th].

[51] A. Kovner and U. A. Wiedemann, "Gluon radiation and parton energy loss," arXiv:hep-ph/0304151 [hep-ph].

[52] J.-Y. Ollitrault, "Anisotropy as a signature of transverse collective flow," *Phys. Rev.* **D46** (1992) 229–245.

[53] W. Reisdorf and H. Ritter, "Collective flow in heavy-ion collisions," *Ann. Rev. Nucl. Part. Sci.* **47** (1997) 663–709.

[54] S. Jeon and V. Koch, "Event by event fluctuations," arXiv:hep-ph/0304012 [hep-ph].

[55] P. F. Kolb, J. Sollfrank, and U. W. Heinz, "Anisotropic transverse flow and the quark hadron phase transition," *Phys. Rev.* **C62** (2000) 054909, arXiv:hep-ph/0006129 [hep-ph].

[56] **STAR Collaboration**, C. Adler *et al.*, "Elliptic flow from two and four particle correlations in Au+Au collisions at $\sqrt{s_{NN}} = 130$ GeV," *Phys. Rev.* **C66** (2002) 034904, arXiv:nucl-ex/0206001 [nucl-ex].

[57] **PHENIX Collaboration**, S. Adler *et al.*, "Elliptic flow of identified hadrons in Au+Au collisions at $\sqrt{s_{NN}} = 200$ GeV," *Phys. Rev. Lett.* **91** (2003) 182301, arXiv:nucl-ex/0305013 [nucl-ex].

[58] **STAR Collaboration**, J. Adams *et al.*, "Particle type dependence of azimuthal anisotropy and nuclear modification of particle production in Au + Au collisions at $\sqrt{s_{NN}} = 200$ GeV," *Phys. Rev. Lett.* **92** (2004) 052302, arXiv:nucl-ex/0306007 [nucl-ex].

[59] **STAR Collaboration**, J. Adams *et al.*, "Azimuthal anisotropy at RHIC: The First and fourth harmonics," *Phys. Rev. Lett.* **92** (2004) 062301, arXiv:nucl-ex/0310029 [nucl-ex].

[60] U. W. Heinz and P. F. Kolb, "Early thermalization at RHIC," *Nucl. Phys.* **A702** (2002) 269–280, arXiv:hep-ph/0111075 [hep-ph].

[61] U. W. Heinz and P. F. Kolb, "Two RHIC puzzles: Early thermalization and the HBT problem," arXiv:hep-ph/0204061 [hep-ph].

[62] **PHENIX Collaboration**, A. Adare *et al.*, "Enhanced production of direct photons in Au+Au collisions at $\sqrt{s_{NN}} = 200$ GeV and implications for the initial temperature," *Phys. Rev. Lett.* **104** (2010) 132301, arXiv:0804.4168 [nucl-ex].

[63] **PHENIX Collaboration**, A. Adare *et al.*, "Scaling properties of azimuthal anisotropy in Au+Au and Cu+Cu collisions at $\sqrt{s_{NN}} = 200$ GeV," *Phys. Rev. Lett.* **98** (2007) 162301, arXiv:nucl-ex/0608033 [nucl-ex].

[64] P. Braun-Munzinger, D. Magestro, K. Redlich, and J. Stachel, "Hadron production in Au - Au collisions at RHIC," *Phys. Lett.* **B518** (2001) 41–46, arXiv:hep-ph/0105229 [hep-ph].

[65] P. Braun-Munzinger, K. Redlich, and J. Stachel, "Particle production in heavy ion collisions," arXiv:nucl-th/0304013 [nucl-th].

[66] S. Voloshin, "Anisotropic flow," *Nucl. Phys.* **A715** (2003) 379–388, arXiv:nucl-ex/0210014 [nucl-ex].

[67] R. Fries, B. Muller, C. Nonaka, and S. Bass, "Hadronization in heavy ion collisions: Recombination and fragmentation of partons," *Phys. Rev. Lett.* **90** (2003) 202303, arXiv:nucl-th/0301087 [nucl-th].

[68] V. Greco, C. Ko, and P. Levai, "Parton coalescence and anti-proton / pion anomaly at RHIC," *Phys. Rev. Lett.* **90** (2003) 202302, arXiv:nucl-th/0301093 [nucl-th].

[69] V. Greco, C. Ko, and P. Levai, "Parton coalescence at RHIC," *Phys. Rev.* **C68** (2003) 034904, arXiv:nucl-th/0305024 [nucl-th].

[70] R. Fries, B. Muller, C. Nonaka, and S. Bass, "Hadron production in heavy ion collisions: Fragmentation and recombination from a dense parton phase," *Phys. Rev.* **C68** (2003) 044902, arXiv:nucl-th/0306027 [nucl-th].

[71] **PHENIX Collaboration**, S. Adler *et al.*, "High transverse momentum η meson production in p^+p, d^+ Au and Au+Au collisions at $\sqrt{s_{NN}} = 200$ GeV," *Phys. Rev.* **C75** (2007) 024909, arXiv:nucl-ex/0611006 [nucl-ex].

[72] **STAR Collaboration**, C. Adler *et al.*, "Centrality dependence of high p_T hadron suppression in Au+Au collisions at $\sqrt{s_{NN}} = 130$ GeV," *Phys. Rev. Lett.* **89** (2002) 202301, arXiv:nucl-ex/0206011 [nucl-ex].

[73] **PHENIX Collaboration**, S. Adler *et al.*, "Suppressed pi0 production at large transverse momentum in central Au+ Au collisions at $\sqrt{s_{NN}} = 200$ GeV," *Phys. Rev. Lett.* **91** (2003) 072301, arXiv:nucl-ex/0304022 [nucl-ex].

[74] **STAR Collaboration**, J. Adams *et al.*, "Transverse momentum and collision energy dependence of high p_T hadron suppression in Au+Au collisions at ultrarelativistic energies," *Phys. Rev. Lett.* **91** (2003) 172302, arXiv:nucl-ex/0305015 [nucl-ex].

[75] M. Gyulassy and X.-N. Wang, "Multiple collisions and induced gluon Bremsstrahlung in QCD," *Nucl. Phys.* **B420** (1994) 583–614, arXiv:nucl-th/9306003 [nucl-th].

[76] **STAR Collaboration**, J. Adams *et al.*, "Evidence from d + Au measurements for final state suppression of high p_T hadrons in Au+Au collisions at RHIC," *Phys. Rev. Lett.* **91** (2003) 072304, arXiv:nucl-ex/0306024 [nucl-ex].

[77] X.-N. Wang, Z. Huang, and I. Sarcevic, "Jet quenching in the direction opposite to a tagged photon in high-energy heavy-ion collisions," *Phys. Rev. Lett.* **77** (Jul, 1996) 231–234. http://link.aps.org/doi/10.1103/PhysRevLett.77.231.

[78] W. Israel, "Nonstationary irreversible thermodynamics: A causal relativistic theory," *Annals of Physics* **100** no. 1–2, (1976) 310 – 331. http://www.sciencedirect.com/science/article/pii/0003491676900646.

[79] W. Israel and J. Stewart, "Transient relativistic thermodynamics and kinetic theory," *Annals of Physics* **118** no. 2, (1979) 341 – 372. http://www.sciencedirect.com/science/article/pii/0003491679901301.

[80] A. Muronga and D. H. Rischke, "Evolution of hot, dissipative quark matter in relativistic nuclear collisions," arXiv:nucl-th/0407114 [nucl-th].

[81] A. Muronga, "Relativistic dynamics of nonideal fluids: Viscous and heat-conducting fluids. i. general aspects and $3+1$ formulation for nuclear collisions," *Phys. Rev. C* **76** (Jul, 2007) 014909. http://link.aps.org/doi/10.1103/PhysRevC.76.014909.

[82] A. Muronga, "Relativistic dynamics of non-ideal fluids: Viscous and heat-conducting fluids. ii. transport properties and microscopic description of relativistic nuclear matter," *Phys. Rev. C* **76** (Jul, 2007) 014910. http://link.aps.org/doi/10.1103/PhysRevC.76.014910.

[83] P. Huovinen and P. Petreczky, "QCD Equation of State and Hadron Resonance Gas," *Nucl. Phys.* **A837** (2010) 26–53, arXiv:0912.2541 [hep-ph].

[84] C. Shen, U. Heinz, P. Huovinen, and H. Song, "Systematic parameter study of hadron spectra and elliptic flow from viscous hydrodynamic simulations of au+au collisions at $\sqrt{s_{NN}} = 200$ gev," *Phys. Rev. C* **82** (Nov, 2010) 054904. http://link.aps.org/doi/10.1103/PhysRevC.82.054904.

[85] P. Romatschke and U. Romatschke, "Viscosity information from relativistic nuclear collisions: How perfect is the fluid observed at rhic?," *Phys. Rev. Lett.* **99** (Oct, 2007) 172301. http://link.aps.org/doi/10.1103/PhysRevLett.99.172301.

[86] M. Luzum and P. Romatschke, "Conformal relativistic viscous hydrodynamics: Applications to rhic results at $\sqrt{s_{NN}} = 200$ GeV," *Phys. Rev. C* **78** (Sep, 2008) 034915. http://link.aps.org/doi/10.1103/PhysRevC.78.034915.

[87] H. Song and U. W. Heinz, "Suppression of elliptic flow in a minimally viscous quark-gluon plasma," *Phys. Lett.* **B658** (2008) 279–283, arXiv:0709.0742 [nucl-th].

[88] H. Song and U. Heinz, "Causal viscous hydrodynamics in 2 + 1 dimensions for relativistic heavy-ion collisions," *Phys. Rev. C* **77** (Jun, 2008) 064901. http://link.aps.org/doi/10.1103/PhysRevC.77.064901.

[89] H. Song and U. Heinz, "Multiplicity scaling in ideal and viscous hydrodynamics," *Phys. Rev. C* **78** (Aug, 2008) 024902. http://link.aps.org/doi/10.1103/PhysRevC.78.024902.

[90] H. Song, "Causal Viscous Hydrodynamics for Relativistic Heavy Ion Collisions," arXiv:0908.3656 [nucl-th].

[91] K. Dusling and D. Teaney, "Simulating elliptic flow with viscous hydrodynamics," *Phys. Rev. C* **77** (Mar, 2008) 034905. http://link.aps.org/doi/10.1103/PhysRevC.77.034905.

[92] D. Molnar and P. Huovinen, "Dissipative effects from transport and viscous hydrodynamics," *J. Phys.* **G35** (2008) 104125, arXiv:0806.1367 [nucl-th].

[93] P. Bożek, "Bulk and shear viscosities of matter created in relativistic heavy-ion collisions," *Phys. Rev. C* **81** (Mar, 2010) 034909. http://link.aps.org/doi/10.1103/PhysRevC.81.034909.

[94] A. K. Chaudhuri, "Centrality dependence of elliptic flow and qgp viscosity," *Journal of Physics G: Nuclear and Particle Physics* **37** no. 7, (2010) 075011. http://stacks.iop.org/0954-3899/37/i=7/a=075011.

[95] B. Schenke, S. Jeon, and C. Gale, "Elliptic and triangular flow in event-by-event D = 3 + 1 viscous hydrodynamics," *Phys. Rev. Lett.* **106** (Jan, 2011) 042301. http://link.aps.org/doi/10.1103/PhysRevLett.106.042301.

[96] B. Schenke, S. Jeon, and C. Gale, "Higher flow harmonics from (3 + 1)d event-by-event viscous hydrodynamics," *Phys. Rev. C* **85** (Feb, 2012) 024901. http://link.aps.org/doi/10.1103/PhysRevC.85.024901.

[97] P. Bożek, "Flow and interferometry in (3 + 1)-dimensional viscous hydrodynamics," *Phys. Rev. C* **85** (Mar, 2012) 034901. http://link.aps.org/doi/10.1103/PhysRevC.85.034901.

[98] J. Vredevoogd and S. Pratt, "Viscous hydrodynamics and relativistic heavy ion collisions," *Phys. Rev. C* **85** (Apr, 2012) 044908. http://link.aps.org/doi/10.1103/PhysRevC.85.044908.

[99] C. Nonaka, Y. Akamatsu, and M. Takamoto, "Study of higher harmonics based on ()-d relativistic viscous hydrodynamics," *Nuclear Physics A* **904–905** no. 0, (2013) 405c – 408c. http://www.sciencedirect.com/science/article/pii/S0375947413001516. The Quark Matter 2012 Proceedings of the {XXIII} International Conference on Ultrarelativistic Nucleus Nucleus Collisions.

[100] L. Del Zanna, V. Chandra, G. Inghirami, V. Rolando, A. Beraudo, *et al.*, "Relativistic viscous hydrodynamics for heavy-ion collisions with ECHO-QGP," *Eur. Phys. J.* **C73** (2013) 2524, arXiv:1305.7052 [nucl-th].

[101] I. Karpenko, P. Huovinen, and M. Bleicher, "A 3+1 dimensional viscous hydrodynamic code for relativistic heavy ion collisions," *Comput. Phys. Commun.* **185** (2014) 3016–3027, arXiv:1312.4160 [nucl-th].

[102] H. Song, "QGP viscosity at RHIC and the LHC - a 2012 status report," *Nucl. Phys.* **A904-905** (2013) 114c–121c, arXiv:1210.5778 [nucl-th].

[103] S. Voloshin and Y. Zhang, "Flow study in relativistic nuclear collisions by Fourier expansion of Azimuthal particle distributions," *Z. Phys.* **C70** (1996) 665–672, arXiv:hep-ph/9407282 [hep-ph].

[104] **CMS Collaboration**, S. Chatrchyan *et al.*, "Measurement of the elliptic anisotropy of charged particles produced in PbPb collisions at nucleon-nucleon center-of-mass energy = 2.76 TeV," *Phys. Rev.* **C87** (2013) 014902, arXiv:1204.1409 [nucl-ex].

[105] J.-Y. Ollitrault, "On the measurement of azimuthal anisotropies in nucleus-nucleus collisions," arXiv:nucl-ex/9711003 [nucl-ex].

[106] A. M. Poskanzer and S. Voloshin, "Methods for analyzing anisotropic flow in relativistic nuclear collisions," *Phys. Rev.* **C58** (1998) 1671–1678, arXiv:nucl-ex/9805001 [nucl-ex].

[107] **NA49 Collaboration**, C. Alt *et al.*, "Directed and elliptic flow of charged pions and protons in Pb + Pb collisions at 40-A-GeV and 158-A-GeV," *Phys. Rev.* **C68** (2003) 034903, arXiv:nucl-ex/0303001 [nucl-ex].

[108] **PHOBOS Collaboration**, B. Alver *et al.*, "System size, energy, pseudorapidity, and centrality dependence of elliptic flow," *Phys. Rev. Lett.* **98** (2007) 242302, arXiv:nucl-ex/0610037 [nucl-ex].

[109] B. Alver, B. Back, M. Baker, M. Ballintijn, D. Barton, *et al.*, "Importance of correlations and fluctuations on the initial source eccentricity in high-energy nucleus-nucleus collisions," *Phys. Rev.* **C77** (2008) 014906, arXiv:0711.3724 [nucl-ex].

[110] R. Snellings, "Elliptic Flow: A Brief Review," *New J. Phys.* **13** (2011) 055008, arXiv:1102.3010 [nucl-ex].

[111] P. M. Dinh, N. Borghini, and J.-Y. Ollitrault, "Effects of HBT correlations on flow measurements," *Phys. Lett.* **B477** (2000) 51–58, arXiv:nucl-th/9912013 [nucl-th].

[112] N. Borghini, P. M. Dinh, and J.-Y. Ollitrault, "Are flow measurements at SPS reliable?," *Phys. Rev.* **C62** (2000) 034902, arXiv:nucl-th/0004026 [nucl-th].

[113] N. Borghini, P. M. Dinh, and J.-Y. Ollitrault, "Flow analysis from multiparticle azimuthal correlations," *Phys. Rev.* **C64** (2001) 054901, arXiv:nucl-th/0105040 [nucl-th].

[114] R. Bhalerao, N. Borghini, and J. Ollitrault, "Analysis of anisotropic flow with Lee-Yang zeroes," *Nucl. Phys.* **A727** (2003) 373–426, arXiv:nucl-th/0310016 [nucl-th].

[115] **CMS Collaboration**, S. Chatrchyan *et al.*, "Long-range and short-range dihadron angular correlations in central PbPb collisions at a nucleon-nucleon center of mass energy of 2.76 TeV," *JHEP* **1107** (2011) 076, arXiv:1105.2438 [nucl-ex].

[116] **CMS Collaboration**, S. Chatrchyan *et al.*, "Centrality dependence of dihadron correlations and azimuthal anisotropy harmonics in PbPb collisions at $\sqrt{s_{NN}} = 2.76$ TeV," *Eur. Phys. J.* **C72** (2012) 2012, arXiv:1201.3158 [nucl-ex].

[117] **CMS Collaboration**, S. Chatrchyan *et al.*, "Observation of long-range near-side angular correlations in proton-lead collisions at the LHC," *Phys. Lett.* **B718** (2013) 795–814, arXiv:1210.5482 [nucl-ex].

[118] N. Borghini, P. M. Dinh, and J.-Y. Ollitrault, "Flow analysis from cumulants: A Practical guide," arXiv:nucl-ex/0110016 [nucl-ex].

[119] A. Bilandzic, R. Snellings, and S. Voloshin, "Flow analysis with cumulants: Direct calculations," *Phys. Rev.* **C83** (2011) 044913, arXiv:1010.0233 [nucl-ex].

[120] C. N. Yang and T. D. Lee, "Statistical theory of equations of state and phase transitions. i. theory of condensation," *Phys. Rev.* **87** (Aug, 1952) 404–409. http://link.aps.org/doi/10.1103/PhysRev.87.404.

[121] T. D. Lee and C. N. Yang, "Statistical theory of equations of state and phase transitions. ii. lattice gas and ising model," *Phys. Rev.* **87** (Aug, 1952) 410–419. http://link.aps.org/doi/10.1103/PhysRev.87.410.

[122] N. Borghini, R. Bhalerao, and J. Ollitrault, "Anisotropic flow from Lee-Yang zeroes: A Practical guide," *J. Phys.* **G30** (2004) S1213–S1216, arXiv:nucl-th/0402053 [nucl-th].

[123] M. Miller and R. Snellings, "Eccentricity fluctuations and its possible effect on elliptic flow measurements," arXiv:nucl-ex/0312008 [nucl-ex].

[124] J.-Y. Ollitrault, A. M. Poskanzer, and S. A. Voloshin, "Effect of flow fluctuations and nonflow on elliptic flow methods," *Phys. Rev.* **C80** (2009) 014904, arXiv:0904.2315 [nucl-ex].

[125] S. A. Voloshin, A. M. Poskanzer, and R. Snellings, "Collective phenomena in non-central nuclear collisions," arXiv:0809.2949 [nucl-ex].

[126] S. A. Voloshin, "Toward the energy and the system size dependece of elliptic flow: Working on flow fluctuations," arXiv:nucl-th/0606022 [nucl-th].

[127] M. Luzum and P. Romatschke, "Conformal Relativistic Viscous Hydrodynamics: Applications to RHIC results at $\sqrt{s_{NN}} = 200$ GeV," *Phys. Rev.* **C78** (2008) 034915, arXiv:0804.4015 [nucl-th].

[128] C. Gale, S. Jeon, B. Schenke, P. Tribedy, and R. Venugopalan, "Event-by-event anisotropic flow in heavy-ion collisions from combined Yang-Mills and viscous fluid dynamics," *Phys. Rev. Lett.* **110** (2013) 012302, arXiv:1209.6330 [nucl-th].

[129] B. Schenke, P. Tribedy, and R. Venugopalan, "Fluctuating Glasma initial conditions and flow in heavy ion collisions," *Phys. Rev. Lett.* **108** (2012) 252301, arXiv:1202.6646 [nucl-th].

[130] C. Shen, S. A. Bass, T. Hirano, P. Huovinen, Z. Qiu, *et al.*, "The QGP shear viscosity: Elusive goal or just around the corner?," *J. Phys.* **G38** (2011) 124045, arXiv:1106.6350 [nucl-th].

[131] D. Kharzeev, E. Levin, and M. Nardi, "Color glass condensate at the LHC: Hadron multiplicities in pp, pA and AA collisions," *Nucl. Phys.* **A747** (2005) 609–629, arXiv:hep-ph/0408050 [hep-ph].

[132] M. Luzum and J.-Y. Ollitrault, "Extracting the shear viscosity of the quark-gluon plasma from flow in ultra-central heavy-ion collisions," *Nucl. Phys.* **A904-905** (2013) 377c–380c, arXiv:1210.6010 [nucl-th].

[133] J.-B. Rose, J.-F. Paquet, G. S. Denicol, M. Luzum, B. Schenke, *et al.*, "Extracting the bulk viscosity of the quark-gluon plasma," arXiv:1408.0024 [nucl-th].

[134] L. Evans and P. Bryant, "LHC Machine," *JINST* **3** (2008) S08001.

[135] C. Lefevre, "LHC: the guide (English version). Guide du LHC (version anglaise)." Feb, 2009.

[136] X. Vidal and R. Cid, "Taking a closer look at lhc, http://www.lhc-closer.es," 2014. http://www.lhc-closer.es.

[137] S. Baird, "Accelerators for pedestrians; rev. version," Tech. Rep. AB-Note-2007-014. CERN-AB-Note-2007-014. PS-OP-Note-95-17-Rev-2. CERN-PS-OP-Note-95-17-Rev-2, CERN, Geneva, Feb, 2007.

[138] **CMS Collaboration**, S. Chatrchyan *et al.*, "Observation of a new boson at a mass of 125 GeV with the CMS experiment at the LHC," *Phys. Lett.* **B716** (2012) 30–61, arXiv:1207.7235 [hep-ex].

[139] **ATLAS Collaboration**, G. Aad *et al.*, "Observation of a new particle in the search for the Standard Model Higgs boson with the ATLAS detector at the LHC," *Phys. Lett.* **B716** (2012) 1–29, arXiv:1207.7214 [hep-ex].

[140] **CMS Collaboration**, V. Khachatryan *et al.*, "Precise determination of the mass of the Higgs boson and tests of compatibility of its couplings with the standard model predictions using proton collisions at 7 and 8 TeV," arXiv:1412.8662 [hep-ex].

[141] R. Bailey and P. Collier, "Standard Filling Schemes for Various LHC Operation Modes," Tech. Rep. LHC-PROJECT-NOTE-323, CERN, Geneva, Sep, 2003.

[142] **CMS Collaboration**, S. Chatrchyan *et al.*, "The CMS experiment at the CERN LHC," *JINST* **3** (2008) S08004.

[143] **ATLAS Collaboration**, G. Aad *et al.*, "The ATLAS Experiment at the CERN Large Hadron Collider," *JINST* **3** (2008) S08003.

[144] **ALICE Collaboration**, K. Aamodt *et al.*, "The ALICE experiment at the CERN LHC," *JINST* **3** (2008) S08002.

[145] **LHCb Collaboration**, J. Alves, A. Augusto *et al.*, "The LHCb Detector at the LHC," *JINST* **3** (2008) S08005.

[146] **TOTEM Collaboration**, G. Anelli *et al.*, "The TOTEM experiment at the CERN Large Hadron Collider," *JINST* **3** (2008) S08007.

[147] **LHCf Collaboration**, O. Adriani *et al.*, "The LHCf detector at the CERN Large Hadron Collider," *JINST* **3** (2008) S08006.

[148] **MoEDAL Collaboration**, J. Pinfold *et al.*, "Technical Design Report of the MoEDAL Experiment," Tech. Rep. CERN-LHCC-2009-006. MoEDAL-TDR-001, CERN, Geneva, Jun, 2009.

[149] **CMS Collaboration**, "Projected Performance of an Upgraded CMS Detector at the LHC and HL-LHC: Contribution to the Snowmass Process," arXiv:1307.7135.

[150] **CMS Collaboration**, "Performance of the CMS detectors in the 2011 Pb+Pb data taking period,".

[151] M. Swartz, D. Fehling, G. Giurgiu, P. Maksimovic, and V. Chiochia, "A new technique for the reconstruction, validation, and simulation of hits in the CMS pixel detector," *PoS* **VERTEX2007** (2007) 035.

[152] O. Djuvsland and J. Nystrand, "Single and double photonuclear excitations in Pb+Pb collisions at $\sqrt{s_{NN}} = 2.76$ TeV at the cern large hadron collider," *Phys. Rev. C* **83** (Apr, 2011) 041901. http://link.aps.org/doi/10.1103/PhysRevC.83.041901.

[153] **CMS Collaboration**, V. Khachatryan *et al.*, "Transverse-momentum and pseudorapidity distributions of charged hadrons in pp collisions at $\sqrt{s} = 7$ TeV," *Phys. Rev. Lett.* **105** (2010) 022002, arXiv:1005.3299 [hep-ex].

[154] S. Porteboeuf, T. Pierog, and K. Werner, "Producing Hard Processes Regarding the Complete Event: The EPOS Event Generator," arXiv:1006.2967 [hep-ph].

[155] M. Gyulassy and X.-N. Wang, "HIJING 1.0: A Monte Carlo program for parton and particle production in high-energy hadronic and nuclear collisions," *Comput. Phys. Commun.* **83** (1994) 307, arXiv:nucl-th/9502021 [nucl-th].

[156] **CMS Collaboration**, S. Chatrchyan *et al.*, "Dependence on pseudorapidity and centrality of charged hadron production in PbPb collisions at a nucleon-nucleon centre-of-mass energy of 2.76 TeV," *JHEP* **1108** (2011) 141, arXiv:1107.4800 [nucl-ex].

[157] **CMS Collaboration**, V. Khachatryan *et al.*, "Observation of Long-Range Near-Side Angular Correlations in Proton-Proton Collisions at the LHC," *JHEP* **1009** (2010) 091, arXiv:1009.4122 [hep-ex].

[158] M. L. Miller, K. Reygers, S. J. Sanders, and P. Steinberg, "Glauber modeling in high energy nuclear collisions," *Ann. Rev. Nucl. Part. Sci.* **57** (2007) 205–243, arXiv:nucl-ex/0701025 [nucl-ex].

[159] B. Alver, M. Baker, C. Loizides, and P. Steinberg, "The PHOBOS Glauber Monte Carlo," arXiv:0805.4411 [nucl-ex].

[160] W. Adam, B. Mangano, T. Speer, and T. Todorov, "Track Reconstruction in the CMS tracker," Tech. Rep. CMS-NOTE-2006-041, CERN, Geneva, Dec, 2006.

[161] **CMS Collaboration**, V. Khachatryan *et al.*, "CMS Tracking Performance Results from early LHC Operation," *Eur. Phys. J.* **C70** (2010) 1165–1192, arXiv:1007.1988 [physics.ins-det].

[162] I. Lokhtin and A. Snigirev, "A Model of jet quenching in ultrarelativistic heavy ion collisions and high-p_T hadron spectra at RHIC," *Eur. Phys. J.* **C45** (2006) 211–217, arXiv:hep-ph/0506189 [hep-ph].

[163] **CMS Collaboration**, "Tracking and Vertexing Results from First Collisions," Tech. Rep. CMS-PAS-TRK-10-001, CERN, 2010. Geneva, 2010.

[164] **CMS Collaboration**, S. Chatrchyan *et al.*, "Measurement of higher-order harmonic azimuthal anisotropy in PbPb collisions at $\sqrt{s_{NN}} = 2.76$ TeV," *Phys. Rev.* **C89** no. 4, (2014) 044906, arXiv:1310.8651 [nucl-ex].

[165] P. Huovinen and P. Ruuskanen, "Hydrodynamic Models for Heavy Ion Collisions," *Ann. Rev. Nucl. Part. Sci.* **56** (2006) 163–206, arXiv:nucl-th/0605008 [nucl-th].

[166] P. Romatschke, "New Developments in Relativistic Viscous Hydrodynamics," *Int. J. Mod. Phys.* **E19** (2010) 1–53, arXiv:0902.3663 [hep-ph].

[167] M. Gyulassy, I. Vitev, and X.-N. Wang, "High p_t azimuthal asymmetry in noncentral $A + A$ at rhic," *Phys. Rev. Lett.* **86** (Mar, 2001) 2537–2540. http://link.aps.org/doi/10.1103/PhysRevLett.86.2537.

[168] **PHENIX Collaboration**, A. Adare *et al.*, "Azimuthal anisotropy of neutral pion production in Au+Au collisions at $\sqrt{s_{NN}} = 200$ GeV: Path-length dependence of jet quenching and the role of initial geometry," *Phys. Rev. Lett.* **105** (2010) 142301, arXiv:1006.3740 [nucl-ex].

[169] S. A. Bass, C. Gale, A. Majumder, C. Nonaka, G.-Y. Qin, *et al.*, "Systematic Comparison of Jet Energy-Loss Schemes in a realistic hydrodynamic medium," *Phys. Rev.* **C79** (2009) 024901, arXiv:0808.0908 [nucl-th].

[170] **STAR Collaboration**, B. Abelev *et al.*, "Centrality dependence of charged hadron and strange hadron elliptic flow from $\sqrt{s_{NN}} = 200$ GeV Au + Au collisions," *Phys. Rev.* **C77** (2008) 054901, arXiv:0801.3466 [nucl-ex].

[171] **ALICE Collaboration**, K. Aamodt *et al.*, "Elliptic flow of charged particles in Pb-Pb collisions at 2.76 TeV," *Phys. Rev. Lett.* **105** (2010) 252302, arXiv:1011.3914 [nucl-ex].

[172] **STAR Collaboration**, B. Abelev *et al.*, "Identified particle production, azimuthal anisotropy, and interferometry measurements in Au+Au collisions at $\sqrt{s_{NN}} = 9.2$ GeV," *Phys. Rev.* **C81** (2010) 024911, arXiv:0909.4131 [nucl-ex].

[173] **PHOBOS Collaboration**, B. Back *et al.*, "Centrality and pseudorapidity dependence of elliptic flow for charged hadrons in Au+Au collisions at $\sqrt{s_{NN}} = 200$ GeV," *Phys. Rev.* **C72** (2005) 051901, arXiv:nucl-ex/0407012 [nucl-ex].

[174] **PHOBOS Collaboration**, B. Back *et al.*, "Pseudorapidity and centrality dependence of the collective flow of charged particles in Au+Au collisions at $\sqrt{s_{NN}} = 130$ GeV," *Phys. Rev. Lett.* **89** (2002) 222301, arXiv:nucl-ex/0205021 [nucl-ex].

[175] **E877 Collaboration**, J. Barrette *et al.*, "Energy and charged particle flow in a 10.8-A/GeV/c Au + Au collisions," *Phys. Rev.* **C55** (1997) 1420–1430, arXiv:nucl-ex/9610006 [nucl-ex].

[176] **CERES Collaboration**, A. Marin, "New results from CERES," *J. Phys.* **G30** (2004) S709–S716, arXiv:nucl-ex/0406007 [nucl-ex].

[177] **CMS Collaboration**, S. Chatrchyan *et al.*, "Multiplicity and transverse momentum dependence of two- and four-particle correlations in pPb and PbPb collisions," *Phys. Lett.* **B724** (2013) 213–240, arXiv:1305.0609 [nucl-ex].

[178] **CMS Collaboration**, "Multiplicity dependence of multiparticle correlations in pPb and PbPb collisions," Tech. Rep. CMS-PAS-HIN-14-006, CERN, Geneva, 2014.

[179] **ALICE Collaboration**, B. B. Abelev *et al.*, "Multiparticle azimuthal correlations in p -Pb and Pb-Pb collisions at the CERN Large Hadron Collider," *Phys. Rev.* **C90** no. 5, (2014) 054901, arXiv:1406.2474 [nucl-ex].

[180] **ATLAS Collaboration**, G. Aad *et al.*, "Measurement with the ATLAS detector of multi-particle azimuthal correlations in p+Pb collisions at $\sqrt{s_{NN}} = 5.2$ TeV," *Phys. Lett.* **B725** (2013) 60–78, arXiv:1303.2084 [hep-ex].

[181] P. Bozek, "Collective flow in p-Pb and d-Pd collisions at TeV energies," *Phys. Rev.* **C85** (2012) 014911, arXiv:1112.0915 [hep-ph].

[182] **ALICE Collaboration**, B. Abelev *et al.*, "Long-range angular correlations on the near and away side in p-Pb collisions at $\sqrt{s_{NN}} = 5.02$ TeV," *Phys. Lett.* **B719** (2013) 29–41, arXiv:1212.2001 [nucl-ex].

[183] **PHOBOS Collaboration**, B. Alver *et al.*, "Event-by-Event Fluctuations of Azimuthal Particle Anisotropy in Au + Au Collisions at $\sqrt{s_{NN}} = 200$ GeV," *Phys. Rev. Lett.* **104** (2010) 142301, arXiv:nucl-ex/0702036 [nucl-ex].

[184] I. Kozlov, M. Luzum, G. Denicol, S. Jeon, and C. Gale, "Signatures of collective behavior in small systems," arXiv:1412.3147 [nucl-th].

[185] B. Schenke and R. Venugopalan, "Eccentric protons? Sensitivity of flow to system size and shape in p+p, p+Pb and Pb+Pb collisions," *Phys. Rev. Lett.* **113** (2014) 102301, arXiv:1405.3605 [nucl-th].

[186] P. Bozek, W. Broniowski, and G. Torrieri, "Mass hierarchy in identified particle distributions in proton-lead collisions," *Phys. Rev. Lett.* **111** (2013) 172303, arXiv:1307.5060 [nucl-th].

[187] A. Bzdak and G.-L. Ma, "Elliptic and triangular flow in p+Pb and peripheral Pb+Pb collisions from parton scatterings," *Phys. Rev. Lett.* **113** no. 25, (2014) 252301, arXiv:1406.2804 [hep-ph].

[188] L. Yan and J.-Y. Ollitrault, "Universal fluctuation-driven eccentricities in proton-proton, proton-nucleus and nucleus-nucleus collisions," *Phys. Rev. Lett.* **112** (2014) 082301, arXiv:1312.6555 [nucl-th].

[189] I. Kozlov, M. Luzum, G. Denicol, S. Jeon, and C. Gale, "Transverse momentum structure of pair correlations as a signature of collective behavior in small collision systems," arXiv:1405.3976 [nucl-th].

[190] A. Dumitru and A. V. Giannini, "Initial state angular asymmetries in high energy p+A collisions: spontaneous breaking of rotational symmetry by a color electric field and C-odd fluctuations," *Nucl. Phys.* **A933** (2014) 212–228, arXiv:1406.5781 [hep-ph].

[191] A. Dumitru, T. Lappi, and L. McLerran, "Are the angular correlations in pA collisions due to a Glasmion or Bose condensation?," *Nucl. Phys.* **A922** (2014) 140–149, arXiv:1310.7136 [hep-ph].

[192] G. Basar and D. Teaney, "Scaling relation between pA and AA collisions," *Phys. Rev.* **C90** no. 5, (2014) 054903, arXiv:1312.6770 [nucl-th].

[193] T. Kalaydzhyan and E. Shuryak, "Self-interacting QCD strings and string balls," *Phys. Rev.* **D90** no. 2, (2014) 025031, arXiv:1402.7363 [hep-ph].

[194] A. Dumitru, L. McLerran, and V. Skokov, "Azimuthal asymmetries and the emergence of "collectivity" from multi-particle correlations in high-energy pA collisions," arXiv:1410.4844 [hep-ph].

[195] J.-P. Blaizot, W. Broniowski, and J.-Y. Ollitrault, "Correlations in the Monte Carlo Glauber model," *Phys. Rev.* **C90** no. 3, (2014) 034906, arXiv:1405.3274 [nucl-th].

[196] A. Bzdak, B. Schenke, P. Tribedy, and R. Venugopalan, "Initial state geometry and the role of hydrodynamics in proton-proton, proton-nucleus and deuteron-nucleus collisions," *Phys. Rev.* **C87** no. 6, (2013) 064906, arXiv:1304.3403 [nucl-th].

[197] "World's smallest droplets,". http://news.vanderbilt.edu/2013/05/worlds-smallest-droplets.